

**Development of carbon capture process
using a flexible metal–organic framework
and critical path method considering
stochastic durations**

A Doctoral Dissertation by

Yuya Takakura

2023

Graduate School of Engineering,

Department of Materials Process Engineering,

Nagoya University

Acknowledgments

First, I am deeply grateful to Dr. Yoshiaki Kawajiri for his patience and support over the past five years. His guidance throughout the period has been precious.

I would like to express my gratitude to all the people who have contributed to developing this thesis. In particular, I would like to mention Prof. Susumu Hashizume, Dr. Tomoyuki Yajima, and Dr. Junpei Fujiki. They have guided me courteously in many ways over the years. Furthermore, I am happy to have the opportunity to work with my colleagues in Kawajiri Lab.

I would like to thank the people at Georgia Tech during my studies there. Prof. Matthew Realff welcomed me as a member of his lab and provided courteous and helpful support. I appreciate Dr. Fani Boukouvala for her collaboration. I am grateful to the members of Realff Lab and Fani Lab for their generous help.

I would like to give thanks to Dr. Hiroshi Kajiro of Nippon Steel Corporation. He provided a great quantity of research data and discussion. Furthermore, he accepted me into his laboratory when I participated in an internship program at Nippon Steel Corporation. Thanks also to Prof. Stefan Kaskel for discussions on modeling adsorption isotherms.

Abstract

Intergovernmental Panel on Climate Change (IPCC) indicates that global warming caused by the anthropogenic carbon dioxide (CO₂) is a growing concern, and that unless CO₂ emissions are reduced to net zero by the 2050s, severe impacts of climate change on humankind will be inevitable. Carbon capture utilization and storage (CCUS), which captures CO₂ from exhaust gases and the atmosphere, sequesters it by storage, and converts it to valuable resources for reuse, is one of the approaches to contribute to the CO₂ reduction. However, cost must be reduced to realize economically feasible CCUS systems.

Since thermal power plants generate about 30% of anthropogenic CO₂ emissions, a cost-efficient post-combustion CO₂ capture process is essential for the CCUS systems. Post-combustion CO₂ capture processes include absorption, adsorption, and membrane separation. Currently, absorption processes are the most established, but they require a large amount of energy to regenerate the absorbent materials. For this reason, adsorption processes are promising because they require less energy to for regeneration than absorptive processes due to their lower CO₂ affinity. While various CO₂ adsorbents have been developed, metal–organic frameworks (MOFs) are new adsorbents that show desirable properties by selecting combinations of organic ligands and metal ions that consist the MOF crystals. Among many MOFs, flexible MOFs have attracted attention because of their unique property of changing structure before and after adsorption. Due to this property, flexible MOFs show remarkable performance for CO₂ separation — high working capacity and selectivity, step-type adsorption isotherm, and low heat

of adsorption. However, they have not yet been analyzed using a process simulation, and the performance of the CO₂ capture process using the flexible MOFs is unknown.

In this thesis, adsorption isotherms were modeled for the CO₂ capture process using a flexible MOF. Adsorption isotherms data using elastic layer-structured metal–organic framework-11 (ELM-11), one of the typical flexible MOFs, were measured by my collaborator, Nippon Steel Corporation. I modeled the stepwise and hysteresis adsorption isotherms which were confirmed to fit well to the data.

The process simulation using ELM-11 was performed using a rigorous model with partial differential-algebraic equations (PDAEs). Since PDAEs may not converge with rapid change in derivatives in a short time, the process simulation with ELM-11 is computationally challenging because the stepwise adsorption isotherms can cause rapid changes in CO₂ partial pressure, and the isotherms hysteresis can cause discrete changes in adsorption amount of CO₂. In this thesis, these problems were solved by applying several numerical techniques. My study is the first to simulate the process with stepwise and hysteresis adsorption isotherms. Note that the operating conditions, such as adsorption time, desorption time, and desorption pressure, were systematically determined for a fair evaluation.

The results of the process simulation revealed the following. First, the CO₂ recovery rate highly depends on feed pressure and temperature. By analyzing the mechanism how the recovery rate is determined, I proposed a simple and useful equation to estimate the recovery rate from feed pressure and temperature without running the simulation. Second, due to the high CO₂ selectivity of ELM-11,

the purity of recovered CO₂ is very high (>99%). Third, ELM-11 shows superior CO₂ recovery, productivity, and power consumption compared to zeolite 13X, a conventional adsorbent. In particular, the stepwise desorption isotherm shortens the desorption time, and productivity is about 4.5 times higher than zeolite 13X. The above results demonstrate that the CO₂ separation process using ELM-11 is promising.

On the other hand, various studies have applied mathematical programming to optimize the economics of CCUS systems. One of such approaches is a resource-constrained project scheduling (RCPS) method, which optimizes system schedules under resource constraints, such as workforces and funds. As far as I know, this method has not yet been applied to CCUS systems. Among the RCPS methods, Critical Path Method (CPM) is a popular method and has been used for various systems scheduling, such as building construction projects, factory management, etc. CPM assumes that each task in the system has a given duration of processing time, which can be reduced by allocating the cost. In the system, the optimum cost allocation is obtained by solving an optimization problem in which the decision variable is cost and the objective function is the minimization of the project completion time. Since the classical CPM assumes that the task durations are fixed values, it cannot account for uncertainties in task durations. This can be a bottleneck for applications in CCUS, which are expected to include duration uncertainties in tasks such as generating electricity from natural energy, transporting synthesized fuel from the recovered CO₂, running CO₂ adsorption processes, etc.

Therefore, the optimization results can be unreliable if the conventional CPM is applied without resolving this critical problem.

I proposed an advanced CPM, which can account for the uncertainty in task durations by expressing them using histograms obtained from historical operation data. I proposed three formulations, all of which have their advantages. The first, Task-Oriented Formulation, has two different ways to improve the task durations by allocating costs and can find more flexible ways of allocating costs than the conventional CPM, which has only one way to improve the durations. However, this method requires many decision variables and takes a long time to solve the optimization problem. The second, Path-oriented Formulation, significantly decreases the number of decision variables compared to Task-Oriented Formulation, instead of limiting the improving ways of task durations to one. The third, Path-oriented Formulation with local search, further reduces the number of decision variables by applying the local search method to Path-Oriented Formulation. This method does not guarantee an optimal solution depending on a range of local searches. The three methods above involve trade-offs between computation time, flexibility in cost allocation methods, and solution accuracy. They should be chosen according to the size of the target system. Note that my formulation of the optimization problem is mixed-integer linear programming (MILP), which can be solved by an algorithm that guarantees a solution, such as the branch and bound method.

In conclusion, this thesis provides important insights into the realization of CCUS systems to improving the economics. The CO₂ separation process with the flexible MOF allows high productivity,

high product purity, and low power consumption. Furthermore, the proposed RCPS methods for designing and operating CCUS systems, which takes into account the uncertainty in task durations, maximizes the productivity of the systems under the cost constraints.

Chapter 1 Introduction

1.1 Global warming and carbon capture technologies

Global warming is the dominant scientific consensus that the human-induced greenhouse effect causes it.^{1,2} Intergovernmental Panel on Climate Change (IPCC) has published a special report, "Global warming of 1.5 °C," which includes extensive information from previous studies.³ The report states that the increase in global temperatures due to human activities reached about 1.0 °C in 2017 compared to pre-industrial ages. If it continues to increase at its current rate, it is likely to reach 1.5 °C between 2030 and 2052. The temperature increases above 1.5 °C is expected to cause the following problems and cause severe damage to human society: damage to buildings and humans from typhoons and rainfall; droughts and the resulting food shortages; reduction in habitable areas due to sea level rise; and an increase in heat stroke patients due to high temperatures.

Limiting global warming to 1.5 °C will require limiting the cumulative global anthropogenic CO₂ emissions.³ It is estimated that anthropogenic CO₂ emissions from pre-industrial times to 2017 amounted to about 2200 ± 320 GtCO₂, and that future CO₂ emissions need to be kept below 420 GtCO₂ to achieve a 66% chance of limiting the warming to 1.5 °C. Since current global emissions are 42±3 GtCO₂ per year, the remaining budget is being consumed. Considering a pathway of emissions, it is estimated that the global CO₂ emissions need to be reduced to a net zero around 2050.

Carbon capture and storage (CCS) is an approach to reducing CO₂ emissions. CCS is a system that extracts high-purity CO₂ from industrial sources using gas separation, transports it to underground

reservoirs such as oil and gas fields or offshore storage, and finally isolates it for long-term storage. According to an International Energy Agency (IEA) report in 2013, CCS contributes significantly to reducing emissions from processes in power generation and industrial applications (steel, cement, oil refining, biofuels, etc.) by implementing 3,000 CCS projects around the world, with annual storage of 7,000 Mt.⁴ However, CCS is expensive and limited for large scale implementation, despite its potential to reduce large amounts of CO₂ with solid government incentives and regulations. The high cost of CCS is primarily caused by capture and compression, which accounts for 75% of the total cost of CCS. Therefore, there is a need to develop more efficient CO₂ separation and compression technologies.⁵

Another approach, carbon capture and utilization (CCU) technology, is a system that converts captured CO₂ into valuable products as a renewable carbon resource rather than permanently sequestering it. Utilizing CO₂ as a resource to produce valuable products is seen as a potential longer-term solution than sequestration. CO₂ can be converted into fuels, fine chemicals, pharmaceuticals, polymers, etc. Although CCU has significant advantages over CCS, the thermodynamic stability of CO₂ makes it necessary to develop technologies to convert CO₂ and use it for chemical reactions. While both CCS and CCU contribute to reducing CO₂ emissions, the combined concept is called carbon capture utilization and storage (CCUS) and is known as the next-generation mechanism for managing CO₂ emissions.

CO₂ emissions from the use of fossil fuels have a significant impact on global warming.⁶ The sector with the highest CO₂ emissions is fossil fuel power plants, which account for about one-third of total

anthropogenic CO₂ emissions.⁷ However, this power generation is essential for the society, and fossil fuel-based power plants are responsible for 80 % of the world's energy supply, with coal-fired power plants providing as much as 42 %.⁸ Fossil fuels will continue to be a major energy source for at least the next 50 years, and thus advanced fossil fuel low-carbon technologies such as CCUS are needed to limit the severe effects of global warming while maintaining people's livelihoods.

1.2 CO₂ separation systems

Post-combustion, pre-combustion and oxy-combustion

There are three known processes for CO₂ separation and recovery: post-combustion, which separates CO₂ after combustion; pre-combustion, which separates CO₂ before combustion; and oxy-combustion, which separates CO₂ during combustion by burning it in pure oxygen.⁵ In post-combustion, CO₂ is separated and recovered from the flue gas generated from boilers in power plants, blast furnaces, etc. The post-combustion CO₂ separation technologies include chemical absorption, physical absorption, membrane separation, and deep-cooling separation. In pre-combustion, H₂, CO, and CO₂ are generated by steam reforming of natural gas or partial oxidation of coal, and the CO₂ is separated from the fuel gas before combustion. The physical absorption and adsorption methods are typically used as CO₂ recovery technologies for pre-combustion. In oxy-combustion, coal is burned using a mixture of high-purity oxygen and recycled flue gas. The CO₂ concentration in the exhaust gas is enriched to about 95%, and more than 90% of the CO₂ can be recovered. Among the above

technologies, this study focuses on post-combustion, which has the advantage of installation in existing thermal power plants and factories. Considering that fossil fuel power generation is the largest source of CO₂ emissions, it is the most urgent technology to be developed.

Absorption separation

The most mature CO₂ separation method is solvent absorption.⁹ Chemical absorption with amine solvents such as aqueous ammonia, monoethanolamine (MEA), diethanolamine (DEA), N-methyl diethanolamine (MDEA), and alkaline solvents such as Ca(OH)₂ and NaOH are commonly used for post-combustion capture in various industries, including cement, steel, power plants, and oil refining.¹⁰⁻¹² The MEA absorption method is particularly selective for CO₂, yielding products with CO₂ concentrations greater than 95%.^{7,13}

Although the absorption method has a high collection efficiency, it requires a large amount of energy for solvent regeneration.⁹ Other challenges include solvent degradation, equipment corrosion, and amine evaporation.^{13,14} On the other hand, absorbents that solve the above problems are being developed: a material called phase separation solvent has been proposed as an alternative to conventional solvents for CO₂ recovery for its ability to reduce the heat of solvent regeneration by up to 50%.^{15,16} A material called CO₂-selective adsorbents absorbs only CO₂ without absorbing water, which eliminates the water desorption process.¹⁷

Membrane separation

Membrane separation is a technology that employs polymer membranes to separate CO₂ using pressure difference as the driving force. Since membrane separation does not require the regeneration of solvents and adsorbents required by absorption and adsorption methods, it is theoretically the most energy-efficient CO₂ separation process.¹⁸ CO₂ separation membranes are selected to have high permeability for CO₂ but low permeability for the other components involved. Well-known CO₂-permeable polymeric membranes for post-combustion applications are PolarisTM and PIM.^{19,20} Other advantages of membrane technology are the following: simplicity, suitability for retrofitting to existing power plants, requiring only little maintenance, and environmental-friendliness.²¹ However, challenges include the limited development of durable membrane supports with large surface areas, and impurities in the gas stream clogging the membranes.

Adsorption separation

The adsorption separation process utilizes the properties of adsorbent materials, which are porous materials, to adsorb specific molecules. Various adsorbents have been evaluated for CO₂ capture from pre-combustion and post-combustion flue gas. Examples of adsorbents include: conventional porous materials such as zeolites, carbon-based materials (activated carbon, carbon nanotubes, carbon nanofibers, graphene, etc.), molecular sieves, MOFs, porous polymer networks (PPN), covalent organic frameworks (COFs).²²

An advantage of the adsorption separation process is the possibility of energy savings for separation because the binding force between the adsorbent and the adsorbent is smaller than that of absorption. On the other hand, it is necessary to consider degradation of adsorbents due to water, NO_x, and SO_x. Zeolite 13X is currently in commercial use for CO₂ removal in air separation processes, but the adsorption capacity of zeolite 13X decreases when it co-adsorbs with water. Other challenges include the difficulty of rapidly changing pressure and temperature in large-scale adsorption processes, unlike in lab-scale experiments, requiring the development of operating methods for the large-scale operation. The effects of gas impurities on the capacity, selectivity, and stability of adsorption processes also need to be studied.¹³

There are two main categories of adsorption processes: pressure swing adsorption (PSA) and temperature swing adsorption (TSA). The PSA process is a cyclic adsorption process and is considered an energy and cost-effective option for CO₂ separation from post-combustion flue gas.^{23,24} The PSA process has been applied to various separation applications, and there are currently at least several hundred thousand PSA units installed worldwide.²⁵ Examples range from small-scale applications, mainly medical oxygen generators and air brake drying systems, to medium and large-scale applications such as H₂ purification and air fractionation. The PSA process has been considered promising for CO₂ separation in large-scale operations. There have been studies investigating PSA both in pre-combustion and post-combustion.^{26,27} On the other hand, the TSA process for CO₂ capture has yet to be implemented on a large scale due to the high energy requirements for adsorbent

regeneration and long cooling step times. New approaches could solve these scale-up challenges, such as hollow fiber adsorbents with cooling media.^{28,29}

The PSA process separates target components by increasing and decreasing the pressure in the system (pressure swing). Figure 1-1 shows the adsorption isotherms of gases A and B on an adsorbent. The PSA process mainly consists of the two operations shown below. Operation (1): putting a mixture of gases A and B into a container containing adsorbent and pressurizing it to the extent indicated by light blue arrows, the amount of gas A and B adsorbed increases by the amount indicated from bottom to top of the gray arrows, respectively. Operation (2): reducing the pressure by the amount indicated by the dark blue arrows, gases A and B are desorbed by the amount indicated from the bottom to the top of the gray arrows, respectively. The gases desorbed by this operation contain a larger amount of gas A.

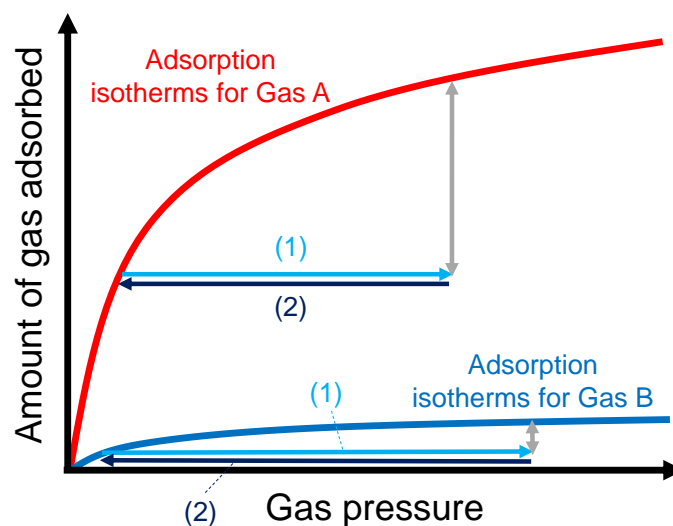


Figure 1-1. Adsorption isotherms for a PSA process

The PSA process employs a vacuum pump in case desorption pressure below atmospheric pressure is required. This process using a vacuum pump is called the vacuum pressure swing adsorption (VPSA) process. This process is also notable for its potential for low energy requirements for CO₂ separation.^{12,30-33} Zeolites and activated carbon beads have been investigated over the past several decades.³⁴⁻³⁶

The efficiency and economics of PSA/TSA processes largely depend on the properties of adsorbents, process design, and operating factors.^{37,38} Criteria for efficient adsorbents for large-scale separations include high working capacity and selectivity, low cost, low regeneration requirements, long-term stability, and fast adsorption kinetics. The design and operating conditions also affect process performance: cycle configuration, number of steps, cycle time, operating pressure or temperature, and number of beds. Although CO₂ separation by adsorption processes is expected to achieve high economic efficiency, they have not yet been adequately developed on a large scale.¹⁸ Developing novel adsorption separation processes using high-performance adsorbents is required. It should be noted that the performance of the adsorbent in a separation process cannot be evaluated as static data such as adsorption isotherms, and a dynamic evaluation must be performed using process model. Furthermore, the process design, configuration, and optimization need to be determined by considering the characteristics of the adsorbent.²²

1.3 Adsorbent materials

Adsorbents are classified by their composition, pore size, and separation mechanism. Separation mechanisms include physisorption, chemisorption, and molecular sieving.¹⁸ Here, I discuss physisorption. Physisorption is adsorption caused by intermolecular forces. Since it shows less entropy change before and after adsorption than chemisorption, it has the following advantages: low heat of adsorption, fast mass transfer, and less energy required for desorption. There are two types of these adsorbents, crystalline and amorphous. Crystalline adsorbents have a very narrow pore size distribution due to their definite positions of atoms, while amorphous adsorbents have a wider pore size distribution due to their random distribution of atoms. Zeolites and metal–organic frameworks (MOFs) are crystalline microporous adsorbents, while carbon-based materials are amorphous microporous adsorbents. Both classes of adsorbents have been widely investigated for their properties and potential as CO₂ adsorbents.¹²

Carbon-based materials

Carbon-based materials are also considered promising adsorbents for CO₂ capture due to their low cost, high surface area, high adaptability to pore structure modification and surface functionalization, and relatively easy regeneration.³⁹ However, because CO₂ cohesive force on the carbon-based material is weak, they are sensitive to temperature change and have relatively low selectivity. For this reason, approaches to increase the interaction between adsorbate and adsorbent to improve CO₂ selectivity

have been investigated, including single-walled carbon nanotubes (CNTs),⁴⁰ multi-walled CNTs,^{41,42} ordered mesoporous carbons,⁴³ microporous carbons,⁴⁴ etc. The idea in the studies is to increase the surface area of the carbon adsorbent by forming different structures and adjusting the pore structure.

Zeolites

Zeolites are porous crystalline aluminosilicates of SiO_4 and AlO_4 tetrahedra regularly bound together via oxygen atoms.³⁹ The crystal lattice is open, with molecular-sized pores into which molecules can enter. The adsorption and gas separation properties of zeolites highly depend on the size, charge density, and distribution of exchangeable cations (Na^+ , K^+ , Ca^{2+} , Mg^{2+} , etc.) present within the porous structure.⁴⁵ The mechanism of CO_2 adsorption on zeolites has been studied by various groups, and it has been shown that CO_2 is physisorbed through ion-dipole interactions.^{46,47}

Zeolites have shown encouraging results for separating CO_2 from gas mixtures and could be used in the pressure swing adsorption (PSA) process. Gas separation by zeolites depends on the structure and composition of the framework and cationic form.⁴⁸ Inui et al. investigated the adsorption behavior of various zeolites in the PSA process and claimed that CHA and 13X were the most appropriate for CO_2 separation.⁴⁹ Krishnamurthy et al. reported a pilot test of a CO_2 separation process using a 7-step PSA with zeolite 13X that showed high performance.⁵⁰

Amine-functionalized adsorbents

Amine-functionalized adsorbents are solid adsorbents in which organic amines are impregnated or grafted onto various porous supports such as activated carbon, zeolite, and silica. These adsorbents benefit from the high CO₂ adsorption capacity of amines while reducing the problems of liquid amine adsorbents, such as high regeneration energy and erosion.⁵¹

The properties required for the amine supports are not to degrade at relatively high temperatures and not to react with the amine during the functionalization. Also, it is necessary to optimize additional properties (specific surface area, porosity, pore volume, etc.) for adsorption and desorption performance. Supports with a larger specific surface area can be impregnated with more amines, leading to a higher adsorption capacity. Porosity and pore volume enable gas molecules to diffuse within the supports. These properties increase the adsorption capacity of CO₂ as well as desorption rate. Hence, the choice of supports significantly affects the performance of the adsorbent.⁵²

There are new strategies to functionalize polymeric compounds such as porous polymers^{53,54} and metal–organic frameworks⁵⁵ with amine-functionalized linkers. Yaghi et al. functionalized IRMOF-74-III with primary or secondary amines.⁵⁶

Amine-functionalized solid adsorbents are highly resistant to moisture. In many cases, moisture increases the CO₂ adsorption capacity yet keeps the regeneration temperature in the same range.^{57,58} This is advantageous in post-combustion CO₂ capture processes since the flue gas from power plants also contains moisture. On the other hand, it is also reported that the following issues need to be

overcome for practical application in industrial scales: long-term thermal stability during the regeneration process; and degradation due to oxidation.

Metal–organic frameworks

Metal–organic frameworks (MOFs) have attracted attention as a new class of crystalline porous materials due to their unique structural properties such as high surface area (up to $6200 \text{ m}^2\text{g}^{-1}$), high porosity (up to 90%) and low crystal density, as well as high thermal and chemical stability.^{59–61} MOFs are materials in which organic ligands bind metal or metal oxide corners. The major advantage of MOFs over conventional porous materials is that the material can be tailored to specific applications by choosing the metal and organic ligands species.⁶² Currently, over 12,000 of MOFs are registered in the Cambridge Structural Database, and some of them have been confirmed to be stable porous materials. However, this is only a portion of the potential materials, as the metal ions and the organic ligands vary widely. There are subsets of MOFs, including isorecticular MOFs (IRMOFs), zeolite imidazolate frameworks (ZIFs), and zeolite-like MOFs (ZMOFs).⁵⁹ Currently, these materials are being investigated for industrial applications. In particular, research using MOFs as a material for CO₂ separation and recovery has been active in recent years.^{11,60,63}

Flexible MOFs

Among many of these materials, flexible MOFs have attracted significant attention for CO₂ capture

due to their unique property of adsorption-induced structural change called “gate-opening/closing” phenomena during adsorption and desorption.^{64–66} This phenomenon occurs when the CO₂ pressure exceeds a specific value called *gate pressure*, and CO₂ rapidly pries open the space between the layers causing adsorption. Due to this property, flexible MOFs show large working capacity, high selectivity, and stepwise or sigmoidal adsorption isotherms. Unlike conventional adsorbents, flexible MOFs do not have trade-offs between selectivity and other performance metrics. Moreover, the flexible MOFs have “intrinsic thermal management capabilities”,^{67,68} where the exothermic heat by adsorption is partially offset by the endothermic expansion of the host framework during gate-opening. The opposite phenomenon occurs during gate-closing: endothermic heat by guest desorption is partially offset by the shrinkage of the host framework. Due to this unique phenomenon, flexible MOFs may be used under nearly isothermal conditions, avoiding loss of working capacity by the heat of adsorption and desorption. One of the most promising flexible MOFs is elastic layer-structured metal–organic framework-11 (ELM-11), which was first reported by Li and Kaneko.⁶⁹ This material has been confirmed to have a large working capacity of CO₂ compared to other flexible MOFs⁷⁰ and investigated by many researchers.^{71–76}

On the other hand, sigmoidal isotherms of flexible MOFs cause a problem of slipping-off, where the target gas CO₂ at a lower concentration than the gate pressure slips through and exit the adsorption column without being captured. This slipping-off phenomenon was first reported by Horike *et al.* and is known to reduce the recovery rate of CO₂.⁷⁷ To solve this problem, Hiraide *et al.* proposed a two-

stage VPSA process,⁷⁸ in which a column packed with a flexible MOF is connected to another column packed with a conventional MOF. In this approach, the second column captures CO₂ that slips off from the first column. A detailed evaluation by dynamic simulation is essential for CO₂ separation capability and cost estimation in VPSA processes, but the complex gas adsorption behavior of flexible MOFs has limited further analysis.

Flexible MOFs have been found to exhibit isotherms with hysteresis,^{79,80} which is the difference between the adsorption and desorption isotherms. In an adsorbent with hysteresis, there exists an infinite number of equilibrium states which depend on the history of adsorption and desorption cycles. A detailed description of the hysteresis and how to model the isotherms are given in this study. The isotherm hysteresis of flexible MOFs has not been implemented within dynamic VPSA simulation, although sigmoidal adsorption isotherms have been modeled for other adsorption systems.⁸¹ Remy *et al.*⁸² and Hefti *et al.*⁸³ modeled sigmoidal isotherms of MOFs without hysteresis. In addition, Štěpánek *et al.*⁸⁴ and Hefti and Mazzotti⁸⁵ modeled water adsorption isotherms on various porous materials, which are hysteretic due to capillary condensation. However, reports on process modeling using flexible MOFs with hysteresis cannot be found.

1.4 Process simulation with partial differential algebraic equations (PDAEs)

Process simulation is the computer representation of a process using physical property data and a mathematical model. The mathematical model often consists of partial differential algebraic equations

(PDAEs) containing mass balance equations, heat balance equations, adsorption rate equations, etc.

The process simulation requires a dynamic model that takes kinetics into account, enabling the evaluation of process performance and the exploration of optimal operating and design conditions.

There are two primary computational methods for solving PDAEs in PSA process simulations. One is to discretize the spatial domain and transform PDAEs into differential algebraic equations (DAEs) only with respect to time. This method is called single discretization (SD).⁸⁶ The other is to discretize space and time in parallel and transform PDAEs into nonlinear algebraic equations (NLAEs). This method is called the full discretization (FD).⁸⁷ Most advanced numerical integration solvers use the SD method, which has become the dominant approach for PSA process simulation.⁸⁸

Dynamic simulation of adsorption processes with flexible MOFs is numerically challenging. The PDAEs are difficult to solve due to rapid and discrete non-differentiable changes in the system. In particular, dynamic models with discrete changes are called hybrid systems and are known to be computationally difficult to solve.^{89,90} In this work, the sigmoidal isotherm with hysteresis of flexible MOFs causes rapid and discrete changes. Because of this problem, adsorption processes considering hysteresis have rarely been studied in the past. While flexible MOFs are considered promising candidates for highly efficient CO₂ separation, the lack of computational approaches has not allowed model-based analysis.

Solutions to the above challenging PDAEs have been investigated. The pseudo-transient continuation method (PTC) is a technique used to solve DAEs where the initial values are far from the

solution.⁹¹ This method introduces transient behavior of the solution until it approaches a steady state, which avoids abrupt changes in the solution and helps convergence.⁹² The method has been used successfully to solve aerodynamics,⁹³ magnetohydrodynamics,⁹⁴ and circuit simulations.⁹⁵ The PTC method has also been used in chemical engineering, including simulation and optimization of heat exchanger models,⁹⁶ and distillation models.⁹⁷

1.5 Decision-making methods for CCUS systems

While CCS systems can play an important role in achieving a low-carbon global society, there are cost challenges; Grimaud and Rouge pointed out that the high cost of CCS necessitates economic incentives or a carbon tax to promote its deployment, especially in the power generation sector.⁹⁸ On the other hand, by combining CCU with CCS and utilizing the captured CO₂ for various valued applications, it may be possible to simultaneously generate electricity from fossil fuels while reducing CO₂ emissions offsetting the costs with revenues. However, due to the variety of technologies involved, development of CCUS systems is complex with spatial, temporal, and other inherent technology issues to be considered.⁹⁹ Many studies have been conducted to analyze these factors to make decisions on how to achieve CCUS: Huang et al. conducted a techno-economic analysis of CCS;¹⁰⁰ Arestra and Dibenedetto reviewed CO₂ utilization options;¹⁰¹ Bruhn et al. investigated the integration of CCU into the CCS context.¹⁰² Frederick et al. summarized extensive research on optimization and decision-making methods for planning CCUS systems.⁹⁹

Mathematical programming is one of the established methods in operations research for decades which is a systematic method for handling the complex decision-making problems.¹⁰³ This method determines system parameters so that the objective functions are optimized under some constraints. Mathematical programming methods are classified by the form of their formulation, and the algorithm applied to solve the problem differ depending on the classification. Linear programming (LP) is a class of optimization problems consisting of only linear algebraic equations and is generally easy to solve. On the other hand, non-linear programming (NLP) is another class of optimization problems with nonlinear equations, and solving NLP problems is generally more complex.

Various CCUS optimization methods using mathematical programming have been studied in the past. The first application of mathematical programming to CCUS was in 1987 for CO₂ allocation problems in enhanced oil recovery using an integer programming model.¹⁰⁴ A review by Huang et al. introduces some optimization models to address the techno-economic problems in CCS.¹⁰⁰ Bai and Wei,¹⁰⁵ and Mavrotas et al.¹⁰⁶ developed multi-objective optimization approaches to select CO₂ capture options that consider both costs and CO₂ emission reductions. Tekiner et al. proposed mixed integer linear programming (MILP) using various energy demand scenarios generated by Monte Carlo simulations.¹⁰⁷ Tan et al. proposed an integer linear program (ILP) to minimize CO₂ emissions, with electricity demand as a constraint.¹⁰⁸ A MILP model with a similar objective was also developed by Pękala et al.¹⁰⁹ Al-Mohannadi and Linke proposed a cost minimization problem, considering the CO₂ network.¹¹⁰

To my knowledge, there is no study that applies resource constrained project scheduling (RCPS) methods to CCUS. The RCPS methods optimize the production schedule with resource constraints, such as manpower and budget. Among these methods, the Critical Path Method (CPM), which is a network-based method, have been widely applied. This method identifies the longest path, which allows us to find the critical path that must be shortened so that the completion time of the whole project can be shortened.¹¹¹ The CPM is one of the most well-known techniques in the RCPS method, and advanced techniques based on CPM have been proposed.¹¹² A review of previous CPM-based approaches is presented in Chapter 4. The CPM-based approaches can be applied to CCUS systems to optimize their overall scheduling and productivity.

1.6 Contribution of this thesis

In this thesis, I propose the following two approaches to improve the design and operation of CCUS systems. The first approach is presented in Chapters 2 and 3 where I present a model-based analysis for a VPSA process using one of the flexible MOFs, ELM-11, with sigmoidal isotherms and hysteresis. Based on experimental uptake data, models of adsorption and desorption isotherms are developed, and their parameters are estimated. By incorporating the resulting isotherm models into a rigorous PDAE model, a simulation of the VPSA process is developed. The numerical challenges to solve the PDAE models, including sigmoidal and hysteresis isotherms, are resolved with the proposed numerical approaches. Sensitivity analysis for feed pressure and temperature is performed using this simulation

to identify optimal operating conditions. Furthermore, a comparison with zeolite 13X, a common CO₂ adsorbent, is also conducted to confirm the advantages of ELM-11. The findings suggest that the VPSA process using ELM-11 is a promising candidate among CO₂ adsorption processes. The contributions of these chapters are as follows: the VPSA process with the adsorbent showing the step-type hysteresis adsorption isotherms was solved for the first time. I demonstrate various advantages of the adsorbent which leads to efficient the VPSA operation. In addition, is the numerical techniques for the challenging problem has the potential to be applied to other computationally complex PDAE systems.

The second approach is presented in Chapter 4, which presents an advanced CPM technique with stochastic durations. The conventional CPM assumes that task durations are fixed values, which is not applicable to CCUS systems that have uncertainty in task durations. For this problem, I propose an advanced CPM approach, where task durations are expressed as discrete histograms obtained from historical operation data, that maximizes the probability that all tasks are completed within a given completion time by improving the task durations on the critical path. I propose two reformulations of the problem as a mixed-integer linear programming problem: one based on tasks, and the other based on paths. In addition, I propose an iterative method to solve the problem efficiently by reducing the number of binary variables. Finally, I demonstrate efficiency of our proposed methods in some case studies. This method contributes to the development of the RCPS field as a novel project management framework and improving the economics of the CCUS systems.

Chapter 2 Modeling adsorption/desorption isotherms

2.1 Preparations for the isotherms modeling

In this section, as preparation to explain my modeling approaches for adsorption isotherms, past studies on ELM-11 and details of our experiments are described.

2.1.1 Past studies on ELM-11

The chemical formula of ELM-11 is $[\text{Cu}(\text{bpy})_2(\text{BF}_4)_2]_n$, which can be obtained by removing water molecules from the crystal lattice of $\{[\text{Cu}(\text{bpy})(\text{H}_2\text{O})_2(\text{BF}_4)_2](\text{bpy})\}_n$. Blake et al. determined the crystal structure by single crystal X-ray structure analysis.¹¹³ ELM-11 has a two-dimensional layered structure, with bpy molecules bridging two Cu ions in the x-y plane, forming a square lattice by their continuous repetition. This layered structure has no apparent voids: the interlayer space is 0.458 nm, which is not enough space for molecules to enter from the side. The interlayer spaces get wider when molecules are adsorbed: in the CO_2 adsorbed form, the spaces become 0.578 nm.¹¹⁴ Hence, CO_2 adsorption enlarges the space by 0.120 nm (26%). Such an expansion is rare in crystals. This unique gating phenomenon was revealed by detailed synchrotron radiation experiments.⁷⁵

In porous materials, various gas adsorption isotherms have been observed, depending on surface properties, pore size, and the properties of gas molecules, and these are classified into six types by IUPAC.¹¹⁵ On the other hand, the adsorption isotherms of ELM-11 cannot be classified into the IUPAC types where the gas adsorption amount in the low-pressure region is almost zero, and the adsorption amount sharply increases at a certain pressure.¹¹⁴

The high selectivity of ELM-11 was investigated by Hiraide et al:⁶⁷ they used GCMC simulations to determine the amount of CO₂/N₂ (10:90) gas mixture adsorbed and found that the selectivity was 135. Compared to the selectivities of common adsorbents which are around 10, the selectivity of ELM-11 is extremely high. This high selectivity is because the gate-opened structure has a significantly higher affinity for CO₂ than for N₂.

2.1.2 Experimental

The pre-ELM-11 sample, a hydrated precursor of ELM-11, was synthesized using the protocol reported by Kondo *et al.*⁷⁵ after some modifications: a methanol solution of 4,4'-bipyridine (3.20 M, 200 mL) was added to an aqueous solution of Cu(II) tetrafluoroborate (0.87 M, 368 mL) for 2 hours with vigorous stirring at room temperature. After additional stirring (1 hour), the reaction mixture was filtrated, and the filter cake was washed with water three times.

Isotherm data of ELM-11 were obtained using BELSORP HP (MicrotracBEL Corp.) equipped with a refrigerated/heating circulator (Julabo USA, Inc., FP-50MA). Before the isotherm measurement, the pre-ELM-11 sample was heated at 110 °C for 30 hours to convert it into ELM-11 and 110 °C for 5 minutes before each measurement.

Three datasets were obtained using three different batches of synthesized ELM-11. The first dataset, Dataset 1, was obtained by measuring CO₂ isotherms for adsorption and desorption at the temperature range from -10 °C to 25 °C. The second dataset is for N₂ adsorption isotherm at 0 °C. Finally, Dataset 3 was obtained at 0 °C, where the desorption branch of the isotherm was measured from an arbitrary

pressure within the pressure range showing gate-adsorption. The experiments were conducted by my collaborator, Nippon Steel Corporation.

2.2 Modeling sigmoidal adsorption/desorption isotherms and hysteresis

In this section, modeling approaches for isotherms of ELM-11 are discussed. ELM-11 is known for its hysteresis phenomenon, which causes the isotherm trajectory to change between adsorption and desorption. Four isotherm trajectories shown in Figure 2-1 (a) are examples of isotherm hysteresis. The isotherm (i) is for a monotonically increasing CO₂ partial pressure from origin, or a clean state, and the isotherm (ii) is for a monotonically decreasing CO₂ partial pressure from a saturated state. These two isotherms are exceptional cases starting from a clean or saturated state, and are called *primary isotherms* in this paper. The trajectories (iii) and (iv), called *secondary isotherms*, are isotherms in which adsorption and desorption switch at intermediate points between clean and saturated, as indicated by circles, respectively: (iii) shows an isotherm where adsorption is switched to desorption at the point shown by the light-blue circle, and (iv) shows an isotherm where desorption is switched to adsorption at the point shown by the orange circle. Moreover, when adsorption and desorption switch again on the trajectories of second-order isotherms, the isotherm takes a new higher-order trajectory. Thus, the adsorption equilibrium depends on the history of adsorption and desorption cycles, and there is an infinite number of isotherms for hysteretic adsorbents, which makes it challenging to analyze in an adsorption process.

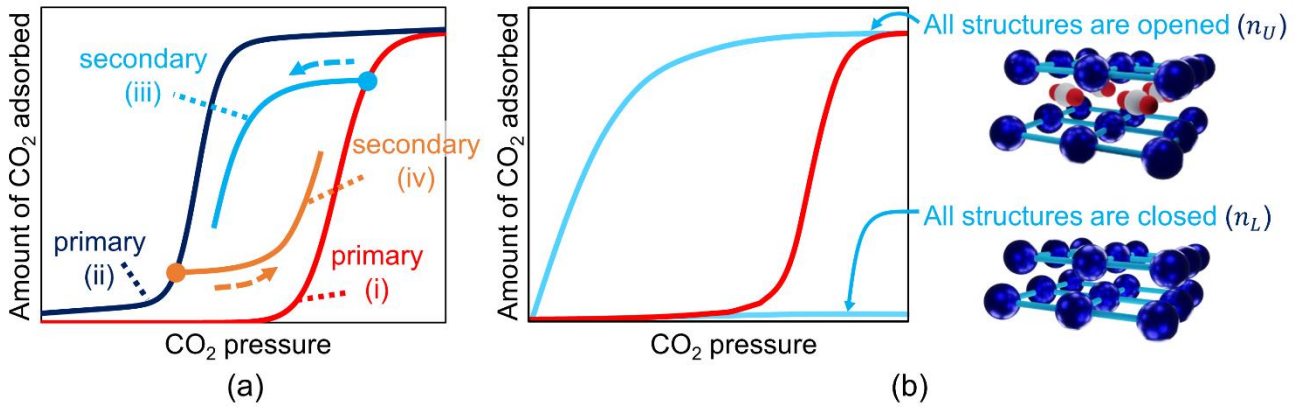


Figure 2-1. Adsorption and desorption isotherms of ELM-11: (a) hysteresis given by primary and secondary isotherms; (b) modeling approach for sigmoidal isotherm using imaginary isotherms.

2.2.1 Modeling sigmoidal shape of primary isotherms

I model the sigmoidal shape of primary isotherms using the approach by Hefti *et al.* eliminating some insensitive parameters to fit our data.⁸³ I assume imaginary adsorption isotherms shown in Figure 2-1 (b); the lower isotherm n_L is an imaginary adsorption isotherm where the gate is always closed regardless of the CO₂ partial pressure, and adsorption occurs only around the outer framework of ELM-11. On the other hand, the upper isotherm n_U is an imaginary isotherm where the gate is always open, and adsorption occurs only inside the framework. Because the actual amount of CO₂ adsorbed is given by the sum of these two amounts, the isotherm n_j is expressed by the following equation:

$$n_j = n_U w_j + n_L (1 - w_j), \quad j = (\text{ads, des}). \quad (2-1)$$

Note that j is mode of isotherms, and $w_j = [0, 1]$ is a weighting function that describes the ratio of gates opened to the total number of gates in the ELM-11 structure.

The isotherms n_L, n_U in Eq. (2-1) are represented by the following equations:

$$n_L = b_L p_{\text{CO}_2}, \quad (2-2)$$

$$n_U = \frac{n_U^\infty b_U p_{\text{CO}_2}}{1 + b_U p_{\text{CO}_2}} + b_H p_{\text{CO}_2}, \quad (2-3)$$

$$b_U = b_U^\infty \exp\left(\frac{E_U}{RT}\right), \quad (2-4)$$

where b_L , b_U^∞ , b_H , and E_U are parameters for the imaginary adsorption isotherms; p_{CO_2} is partial pressure of CO_2 ; T is temperature. Since the lower isotherm n_L is very small, approximating n_L to a linear isotherm is found to be sufficient. Note that n_U is always larger than n_L at any CO_2 partial pressure. The weighting function w_j in Eq. (2-1) is described as the cumulative log-logistic function as:

$$w_j = \frac{\exp\left(\frac{\ln(p_{\text{CO}_2}) - \ln(p_{\text{step},j}(T))}{\chi_j}\right)}{1 + \exp\left(\frac{\ln(p_{\text{CO}_2}) - \ln(p_{\text{step},j}(T))}{\chi_j}\right)}, \quad (2-5)$$

where χ_j is a parameter for the weighting function; $p_{\text{step},j}(T)$ is step pressure of isotherm j at temperature T , which determines the position of the step where the isotherms rise. The temperature dependence of $p_{\text{step},j}(T)$ for ELM-11 was experimentally confirmed by Hiraide *et al.*⁷² The step pressure $p_{\text{step},j}(T)$ is expressed by the following equation, which is also proposed by Sinha *et al.*²⁸

$$p_{\text{step},j}(T) = p_{\text{step},j,0} \exp\left(-\frac{H_{\text{step},j}}{R} \left(\frac{1}{T_0} - \frac{1}{T}\right)\right), \quad (2-6)$$

where $p_{\text{step},j,0}$ is the step pressure of isotherm j at a reference temperature $T_0 = 273.15$ [K]; $H_{\text{step},j}$ is the enthalpy of the phase transitions.

2.2.2 Modeling secondary and higher-order isotherms

I describe the isotherm trajectories that depend on the history of adsorption and desorption cycles.

I refer to the secondary and higher-order adsorption isotherms as $n_{\text{des} \rightarrow \text{ads}}$ and the desorption isotherms as $n_{\text{ads} \rightarrow \text{des}}$.

The proposed approach is illustrated in Figure 2-2, where secondary isotherms are given by *vertically compressing* the primary isotherms. The equilibrium follows the branched trajectory $n_{\text{des} \rightarrow \text{ads}}$ shown as the orange line in Figure 2-2 (a) when desorption is carried out until reaching Point A, and then adsorption occurs. I obtain the secondary isotherm $n_{\text{des} \rightarrow \text{ads}}$ by vertically compressing the primary isotherm n_{ads} *from the bottom to the top* as follows:

$$n_{\text{des} \rightarrow \text{ads}} = n_{\text{ads}} \cdot \left\{ \frac{(n_{\text{sat}} - n_{\text{switch}})}{n_{\text{sat}}} \right\} + n_{\text{switch}}, \quad (2-7)$$

where n_{switch} is the amount of CO₂ adsorbed at the time of the switching operation between desorption and adsorption; n_{sat} is a saturated amount of CO₂ adsorbed. The ratio $(n_{\text{sat}} - n_{\text{switch}})/n_{\text{sat}}$ is the ratio of gates not yet opened to the total number of gates in the ELM-11 structure. Note that $n_{\text{des} \rightarrow \text{ads}}$ is consistent with n_{ads} when $n_{\text{switch}} = 0$, i.e., when desorption is completed until reaching the *clean* state and then switched to adsorption. This modeling approach is the same as in Hefti and Mazzotti, who modeled the hysteretic isotherms by capillary condensation in the physisorption of water vapor.⁸⁵

Similarly, the equilibrium follows the trajectory $n_{\text{ads} \rightarrow \text{des}}$ shown as a light-blue line in Figure 2-2 (b) when adsorption is carried out until reaching Point B, and then desorption occurs. I obtain the secondary isotherm in the same manner as Eq. (2-7) by vertically compressing the primary isotherm

n_{des} , but this time *from the top to the bottom*, as follows:

$$n_{\text{ads} \rightarrow \text{des}} = n_{\text{des}} \cdot \left(\frac{n_{\text{switch}}}{n_{\text{sat}}} \right). \quad (2-8)$$

The ratio $(n_{\text{switch}}/n_{\text{sat}})$ gives the ratio of gates that are not closed to the total number of gates in the ELM-11 structure. Note that $n_{\text{ads} \rightarrow \text{des}}$ is consistent with n_{des} when $n_{\text{switch}} = n_{\text{sat}}$, i.e., when adsorption is switched to desorption after saturation.

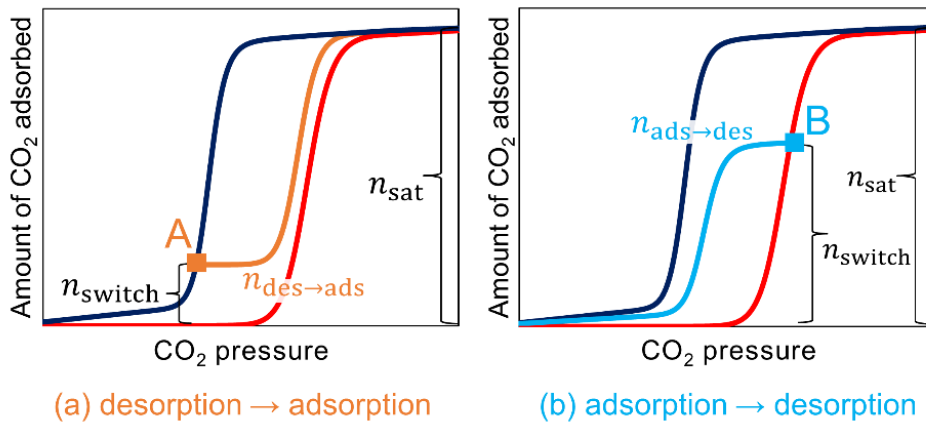


Figure 2-2. Modeling secondary and higher-order isotherms:
(a) adsorption isotherm; (b) desorption isotherm.

2.2.3 Modeling isotherm hysteresis in VPSA simulation, and N₂ isotherm

In this study, it is assumed that the adsorption/desorption isotherm is given by $n_{\text{des} \rightarrow \text{ads}}$ for the pressurization and adsorption steps and $n_{\text{ads} \rightarrow \text{des}}$ for the depressurization and desorption steps in the 4-step VPSA process. From this assumption, the hysteresis of the adsorption isotherm for CO₂ is expressed by the following equation:

$$q_{\text{CO}_2}^* = n_{\text{des} \rightarrow \text{ads}} \cdot \text{mode} + n_{\text{ads} \rightarrow \text{des}} \cdot (1 - \text{mode}), \quad (2-9)$$

where mode is a binary variable; $q_{\text{CO}_2}^*$ is equilibrium amount of CO₂ adsorbed. $q_{\text{CO}_2}^*$ is equal to the adsorption isotherm $n_{\text{des} \rightarrow \text{ads}}$ when mode = 1, and the desorption isotherm $n_{\text{ads} \rightarrow \text{des}}$ when mode = 0. The following equation determines this binary variable:

$$\text{mode} = \begin{cases} 1 & \text{if } 0 \leq t < t_{\text{press}} + t_{\text{ads}} \\ 0 & \text{if } t_{\text{press}} + t_{\text{ads}} \leq t < t_{\text{press}} + t_{\text{ads}} + t_{\text{depress}} + t_{\text{des}} \end{cases}, \quad (2-10)$$

where t is time since each cycle started; t_{press} , t_{ads} , t_{depress} , t_{des} are pressurization, adsorption, depressurization, desorption time, respectively.

The adsorption isotherm of N₂ is approximated by the temperature-independent linear model shown in the following equation.

$$q_{\text{N}_2}^* = b_{\text{N}_2} p_{\text{N}_2}, \quad (2-11)$$

where b_{N_2} is a temperature-independent parameter; $q_{\text{N}_2}^*$ is equilibrium amount of N₂ adsorbed; p_{N_2} is partial pressure of N₂.

2.3 Parameter estimation and fitting results

This section shows estimation results of the isotherm parameters included in Eqs. (2-1)–(2-6) and (2-11) for Datasets 1–3 shown in Figure 2-3 and Figure 2-4. The isotherm parameters for CO₂ were obtained separately for each dataset to consider the minor differences among the three batches. The isotherm of N₂, where the amount adsorbed is very small and differences among the batches are probably negligible, was assumed to be common for all datasets. The least-squares method was used for the estimation.

Estimated parameters at different temperatures from Dataset 1 are shown in Figure 2-3 and Table 2-1. The coefficients of determination (R^2) are shown in Table 2-2. Figure 2-3 and the values of R^2 show that the model matches the experimental data well.

The fitting for Dataset 2 is shown in Figure 2-4 (a). The estimated value of the parameter b_{N_2} is $3.05 \times 10^{-5} \text{ molN}_2/(\text{kg}_{\text{ads}} \cdot \text{kPa})$. The value of R^2 is 0.987, indicating that this model also describes the data well.

The fitting for Dataset 3 is shown in Figure 2-4 (b) and (c), and the estimated parameters are shown in Table 2-3. In this case, the weighting function w_j is expressed by the following equation:

$$w_j = \left(\frac{\exp\left(\frac{\ln(p_{\text{CO}_2}) - \ln(p_{\text{step},j}(T)})}{\chi_j}\right)}{1 + \exp\left(\frac{\ln(p_{\text{CO}_2}) - \ln(p_{\text{step},j}(T)})}{\chi_j}\right)} \right)^{v_j}, \quad (2-12)$$

where v_j [-] is a parameter in Hefti *et al.*⁸³ In fitting the model to the data to Dataset 3, I did not fix v_j to one but found the optimal value by parameter estimation. The values of R^2 for primary adsorption, desorption isotherms and the four secondary desorption isotherms are 1.00, 0.996, and 0.933, respectively. This result shows that the model can also describe the secondary desorption isotherm well.

Table 2-1 Estimated parameters for CO₂ adsorption/desorption isotherms using Dataset 1

Parameters	Values
b_L	9.15×10^{-4} [molCO ₂ /(kg _{ads} ·kPa)]
b_{U^∞}	4.22×10^{-8} [kPa ⁻¹]
b_H	0 [molCO ₂ /(kg _{ads} ·kPa)]*
n_{U^∞}	3.92 [molCO ₂ /kg _{ads}]
E_U	34.1 [kJ/molCO ₂]
χ_{ads}	0.0405 [-]
χ_{des}	0.0329 [-]
$p_{step0,ads}$	34.8 [kPa]
$p_{step0,des}$	24.3 [kPa]
$H_{step,ads}$	-23.3 [kJ/molCO ₂]
$H_{step,des}$	-22.2 [kJ/molCO ₂]

* Due to the limited number of high-pressure isotherm data, the value could not be estimated and was set to zero.

Table 2-2 Coefficients of determination R^2 for Dataset 1

Temperature [K]	R^2 for adsorption isotherms	R^2 for desorption isotherms
263.15	0.986	0.993
268.15	0.996	0.996
273.15	0.995	0.994
278.15	0.991	0.997
283.15	0.998	0.997
288.15	0.998	0.994
293.15	0.995	0.991
298.15	0.992	0.983

Table 2-3 Estimated parameters from Dataset 3

Parameters	Values
b_L	1.02×10^{-3} [molCO ₂ /(kg _{ads} · kPa)]
b_U^∞	4.85×10^{-6} [kPa ⁻¹]
b_H	3.33×10^{-3} [molCO ₂ /(kg _{ads} · kPa)]
n_U^∞	3.01 [molCO ₂ /kg _{ads}]
E_U	28.7 [kJ/molCO ₂]
v_{ads}	4.17 [-]
v_{des}	3.91 [-]
χ_{ads}	0.0414 [-]
χ_{des}	0.0456 [-]
$p_{step0,ads}$	30.6 [kPa]
$p_{step0,des}$	21.7 [kPa]
$H_{step,ads}$	-25.0 [kJ/molCO ₂]
$H_{step,des}$	-25.0 [kJ/molCO ₂]

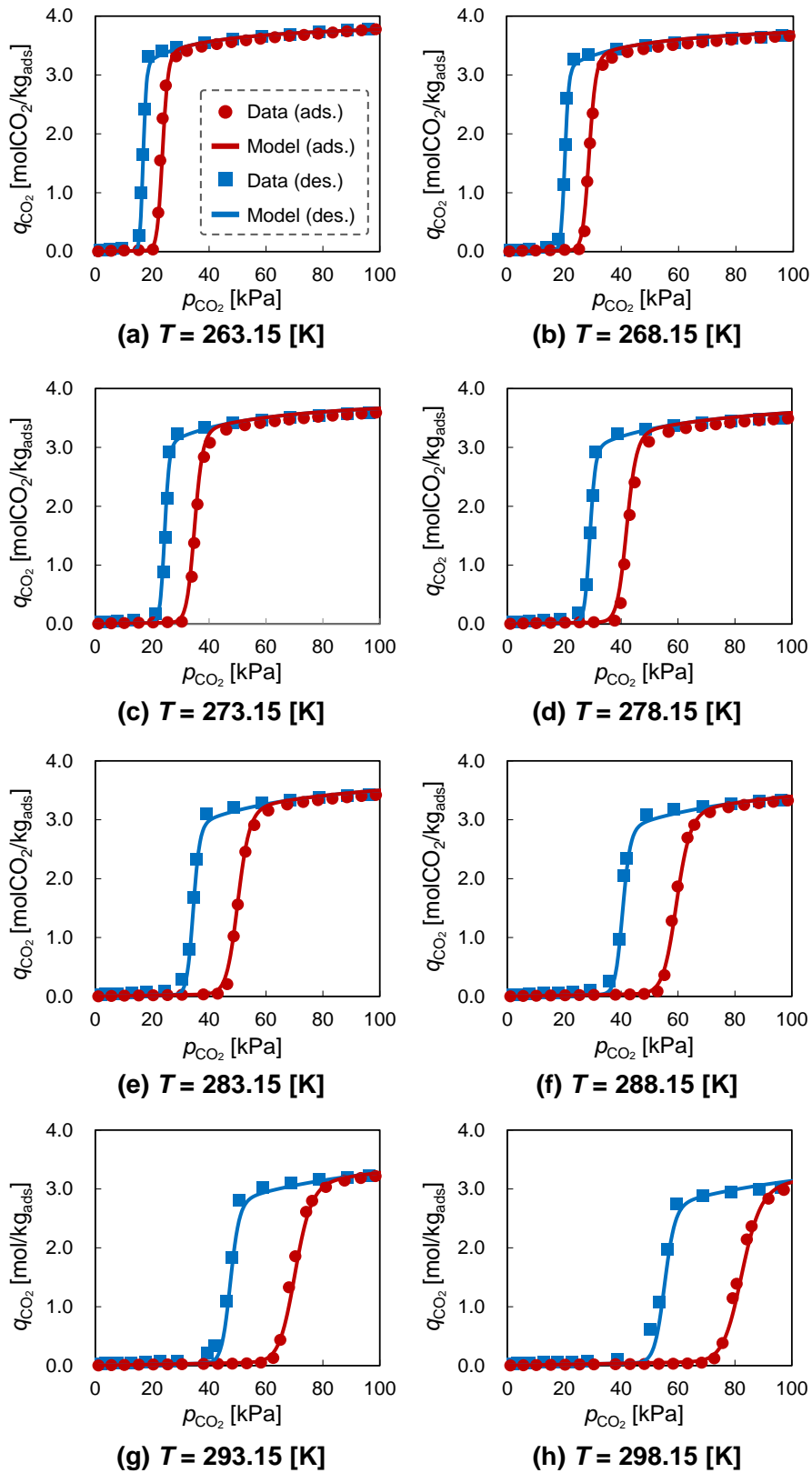


Figure 2-3. Fitting of primary isotherms at temperature 263.15–298.15 K for Dataset 1: (a) 263.15 K; (b) 268.15 K; (c) 273.15 K; (d) 278.15 K; (e) 283.15 K; (f) 288.15 K; (g) 293.15 K; (h) 298.15 K.

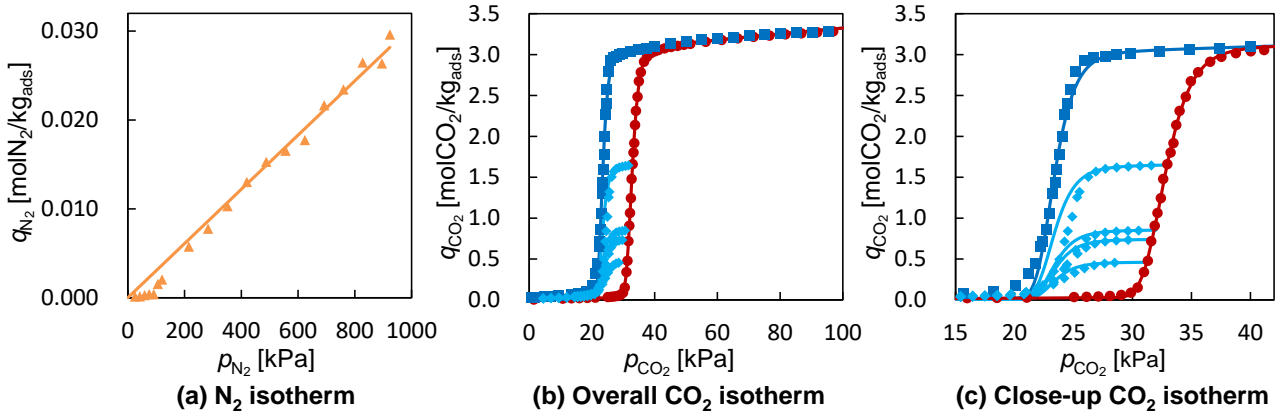


Figure 2-4. Isotherm model fitting: (a) N_2 isotherm for Dataset 2; (b) primary isotherms and secondary desorption isotherms of CO_2 for Dataset 3; (c) magnified plot of p_{CO_2} in 15–40 kPa for Dataset 3.

2.4 Concluding remarks

In this chapter, adsorption isotherms of ELM-11 are modeled based on the data provided by my collaborator, Nippon Steel Corporation. First, the stepwise adsorption isotherms of ELM-11 were modeled using two imaginary Langmuir adsorption isotherms and a weighting function, in the same approach as Hefti et al.⁸³ Furthermore, the hysteresis of the isotherms was modeled by compressing the primary isotherms using the ratio between CO_2 adsorption amount when switching operations and saturated CO_2 adsorption amount, as proposed by Hefti and Mazzotti.⁸⁵ These models show good fitting to Dataset 1–3. In addition, the mode switching adsorption/desorption isotherms in the VPSA process was modeled by the logic condition (2-10).

Chapter 3 VPSA process simulation

This chapter describes the VPSA process simulations performed in this study. It presents process description, modeling assumptions, model equations, operating conditions, techniques for the calculations, and simulation results.

3.1 Process descriptions

In this study, a rigorous dynamic model is developed for the VPSA process using ELM-11, as well as zeolite 13X, which was chosen to compare its performance against ELM-11 as a conventional and well-known adsorbent, as employed in recent studies.^{21,37} This process is for CO₂ separation from the post-combustion flue gas, and it is assumed that water and SO_x in this gas is removed in a pretreatment step.

A simple 4-step VPSA cycle is employed as shown in Figure 3-1. In the pressurization step (Step 1), mixed gas of CO₂ and N₂ is supplied from the inlet at the bottom of the column until the desired pressure is reached. In this step, the gas outlet at the top of the column is closed. In Step 2, the adsorption step, the mixed gas is kept being injected from the inlet while the outlet is opened to release N₂ rich gas. In Step 3, the depressurization step, the inlet is opened and the column is depressurized to atmospheric pressure. In Step 4, the desorption step, the pressure is reduced using a vacuum pump to collect the CO₂ product from the bottom of the column. Steps 1 to 4 above are repeated in a cyclic manner until the process reaches a cyclic steady state. Note that the column is assumed to be externally

covered by a jacket whose temperature is kept constant at T_{wall} .

The VPSA process considered in this study is a simple process that consists only of a single bed, where the cycle does not involve rinse and purge steps. The rinse operation reduces the productivity by re-injecting the product but is necessary for processes using conventional adsorbents to achieve sufficient product purity.¹¹⁷ Furthermore, the purge operation reduces the product purity by injecting N_2 during the desorption step but is necessary for the conventional processes to desorb CO_2 to a sufficient degree.¹¹⁸ These inefficient operations can be eliminated by using ELM-11 because the adsorbent effectively desorbs CO_2 when the pressure is lowered owing to the sigmoidal desorption isotherm.

It is also assumed that ELM-11 is supported on a binder and packed in the column as pellets. Since flexible MOFs have substantial volume changes due to the structural change by adsorption, employing a rigid binder would inhibit the structural change and thus reduce their adsorption amount.⁶⁸ Because of this problem, the binder must be a flexible material. As a material that satisfies such a property, cellulose can be used as demonstrated by Kajiro *et al.*¹¹⁹ I chose this material with a weight ratio of 1:3 between cellulose to ELM-11, which was reported in this patent. The pellet packing density (1030 kg/m^3) is the sum of the packing densities of ELM ($771 \text{ kg}_{\text{ads}}/\text{m}^3$) and cellulose (259 kg/m^3). Similar binders for flexible MOFs are reported using an adsorption sheet and methylcellulose,^{120,121} which was experimentally confirmed to have sufficient mechanical strength.

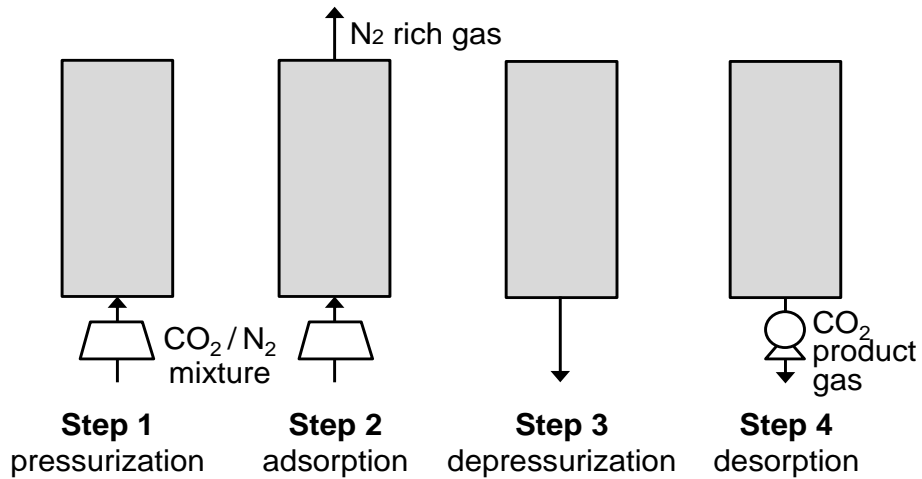


Figure 3-1. Four-step cycle of the VPSA process.

3.2 Modeling assumptions

In our model, the following assumptions were made. Note that Assumptions 9–11 were applied only for ELM-11.

1. The gas phase follows the ideal gas law.
2. Radial variations of temperature, pressure, and concentration are neglected.
3. Axial thermal dispersion occurs only through the gas.
4. Between the gas and the adsorbents, thermal equilibrium is established.
5. Mass transfer rate between gas and adsorbent phases is expressed by the linear driving force (LDF) model.
6. Mass transfer coefficient and thermal conductivity are constant regardless of temperature.
7. Physical properties of adsorbents, such as density, do not change with temperature.
8. Pressure drop is given by the Ergun equation.

9. Rate-determining step of mass transfer is the structural change of ELM-11 for adsorption of CO₂.
10. Two parameters for nitrogen adsorption that have not been measured or reported in the past are determined as follows: adsorption heat H_{N_2} is assumed to be the same as that of CO₂, and mass transfer coefficient k_{N_2} is assumed to be the same as that of zeolite 13X. This assumption is employed as a *conservative* estimate for heat balance equations; the potentially overestimated heat of adsorption for N₂ may underestimate the working capacity for ELM-11. In the mass balance equations, on the other hand, the temperature dependence of the N₂ isotherm, which is determined by the heat of adsorption, was ignored. The influence of this simplification is confirmed to be negligible, since the amount of N₂ adsorbed is small (about one-hundredth of CO₂).
11. The switching of adsorption and desorption isotherms by hysteresis is determined by Eq. (2-10).

Assumption 3 assumes the thermal diffusion through the adsorbent is much smaller than that through the gas. This assumption is reasonable for ELM-11 because the binder is cellulose, with low thermal conductivity. The same assumption was used by Schell *et al.*,¹²² who reported precombustion CO₂ capture by PSA using activated carbon.

Assumption 5 for ELM-11 was confirmed by Fujiki *et al.* They performed breakthrough experiments to verify that the adsorption rate of ELM-11 can be modeled by the LDF model.¹²³ Kondo *et al.* conducted adsorption experiments at 273–303 K temperatures using a laboratory-designed volumetric apparatus and fitted the transient data to the double-exponential and LDF models.¹²⁴ The

results showed that the adsorption rate is proportional to the driving force $q^*_{\text{CO}_2} - q_{\text{CO}_2}$ and both models show reasonable agreement.

For Assumption 6, Kondo *et al.* reported that the mass transfer coefficient increases at lower temperatures,¹²⁴ but I use the value at 298 K consistently throughout this study as a conservative estimate. To verify this assumption, I analyzed the sensitivity for the mass transfer coefficient. I compared two cases changing the different mass transfer coefficients: the first case has the mass transfer coefficient at 298 K ($k_{\text{CO}_2} = 0.0454$ [1/s]); the other case has the same mass transfer coefficient as zeolite 13X ($k_{\text{CO}_2} = 0.0220$ [1/s]). These two cases are at 298 K and a feed pressure of 1300 kPa (the details are shown as Case 1 and Case 2 in Table 3-8). There, the desorption time takes the same value, 350 s. It can be seen that the influence by employing the different mass transfer coefficients for ELM-11 is insignificant; recovery increases only by 2.6%, purity decreases only by 0.1%, BSF increases only by 7%, and power consumption decreases only by 2.4%. These changes are negligible in the comparison between zeolite 13X and ELM-11. Nevertheless, measurement and further verification of the mass transfer rate are desired.

Based on Assumption 9, the mass transfer coefficient measured by Kondo *et al.* is for the structural change of ELM-11 for adsorption of CO₂, which is assumed to be equal to the overall mass transfer coefficient of CO₂, k_{CO_2} . To verify this assumption, I analyzed the rate-determining step of CO₂ adsorption of ELM-11 by examining the contribution of the gas-film mass transfer to the overall mass transfer. The gas-film mass transfer coefficient k_g [m/s] was obtained as $k_g = 0.0533$ [m/s] using the

equation estimated by Wakao and Funazkri¹²⁵, in a case which total pressure, temperature, and molar flow rate are given as 1000 kPa, 298 K, and 0.198 mol/s, respectively. The diffusion coefficient between CO₂ and N₂ in the equation was calculated using the method by Fuller *et al.*¹²⁶

From the above value of k_g , I can confirm that the gas-film mass transfer is sufficiently fast. The overall mass transfer coefficient k_{CO_2} in the LDF model is expressed as follows:

$$k_{CO_2} = \frac{1}{1/k_s + H/k_g} [1/s], \quad (3-1)$$

where k_s [1/s] is the mass transfer coefficient for the structural change of ELM-11 and entering of CO₂ into it, k_g [m³/(kg_{ads}·s)] is the gas-film mass transfer coefficient, and H [m³/kg_{ads}] is Henry's constant.

The above equation is applicable under the following two assumptions: first, there is no CO₂ accumulation in the gas-film; and Henry's law $q_{CO_2} = Hc_{CO_2}$, where c_{CO_2} [molCO₂/m³] is concentration of CO₂, is satisfied in the film. Henry's constant is obtained as $H = 0.0771$ [m³/kg_{ads}] using one point of the adsorption isotherm that is close to saturation (q_{CO_2}, c_{CO_2}) = (3.11 molCO₂/kg_{ads}, 40.4 molCO₂/m³). On the other hand, $k_s = 0.0454$ [1/s] at 298 K gas temperature as reported by Kondo *et al.*¹²⁴ Using the above values, the values $1/k_s$ and H/k_g in the above equation are obtained as $1/k_s = 22.0$ [s] and $H/k_g = 0.866$ [s]. It indicates that the mass transfer in the gas film is sufficiently fast compared to that for the structural change of ELM-11. I also assume that diffusion in the cellulose binder, which is a highly porous material, is sufficiently fast, and thus the structural change of ELM-11 is the rate-determining step.

Assumption 11 was made to mitigate the numerical difficulty in solving the PDAE model. This simplification may lead to some model error if local adsorption occurs in the desorption step, or local desorption occurs in the adsorption step, which cannot be verified in our study due to the numerical difficulty. The same assumption was made by Hefti and Mazzotti, and Štěpánek *et al.*^{84,85}

3.3 Model equations

3.3.1 Overall equations

A similar model of partial differential algebraic equations (PDAEs) to that of Ko *et al.*³⁵ is employed as shown in Table 3-1. The model equations are implemented within the gPROMS modeling environment (Process System Enterprise). The centered finite difference method (CFDM) is used to discretize the spatial domain. The method of lines is used to solve the resulting system of the differential algebraic equations (DAEs). A DAE solver in gPROMS, SRADAU, is used to solve the model equations.

Table 3-1 Model equations for the VPSA simulation

Component mass balance	$-D_L \left[\frac{\partial^2 y_i}{\partial z^2} + 2T \left(\frac{\partial y_i}{\partial z} \right) \left\{ \frac{\partial}{\partial z} \left(\frac{1}{T} \right) \right\} + 2 \left(\frac{1}{P} \right) \left(\frac{\partial y_i}{\partial z} \right) \left(\frac{\partial P}{\partial z} \right) \right]$ $+ \frac{\partial y_i}{\partial t} + u \frac{\partial y_i}{\partial z} + \frac{1}{\varepsilon_{\text{bed}}} \frac{RT}{P} \rho_{\text{ads}} \left(\frac{\partial q_i}{\partial t} - y_i \sum_i \frac{\partial q_i}{\partial t} \right) = 0$	(3-2)
Overall mass balance	$\frac{\partial u}{\partial z} + \frac{u}{P} \frac{\partial P}{\partial z} + uT \frac{\partial}{\partial z} \left(\frac{1}{T} \right) + T \frac{\partial}{\partial t} \left(\frac{1}{T} \right) + \frac{1}{P} \frac{\partial P}{\partial t}$ $-D_L \left[T \frac{\partial^2}{\partial z^2} \left(\frac{1}{T} \right) + \frac{1}{P} \frac{\partial^2 P}{\partial z^2} + 2 \left(\frac{T}{P} \right) \left(\frac{\partial P}{\partial z} \right) \left(\frac{\partial}{\partial z} \left(\frac{1}{T} \right) \right) \right]$ $+ \frac{1}{\varepsilon_{\text{bed}}} \frac{RT}{P} \rho_{\text{ads}} \sum_i \frac{\partial q_i}{\partial t} = 0$	(3-3)
Ergun equation	$-\frac{\partial P}{\partial z} = 150 \frac{\mu u}{4R_p^2} \frac{(1 - \varepsilon_{\text{bed}})^2}{\varepsilon_{\text{bed}}^3} + 1.75 \frac{(1 - \varepsilon_{\text{bed}})}{2R_p \varepsilon_{\text{bed}}^3} u u \rho_{\text{gas}}$	(3-4)
LDF model	$\frac{\partial q_i}{\partial t} = k_i (q_i^* - q_i)$	(3-5)
Heat balance equation	$\left\{ \varepsilon_{\text{bed}} \rho_{\text{gas}} C_{pg} + \rho_{\text{pellet}} C_{ps} \right\} \frac{\partial T}{\partial t} + \rho_{\text{gas}} C_{pg} \varepsilon_{\text{bed}} u \frac{\partial T}{\partial z} - K_L \frac{\partial^2 T}{\partial z^2}$ $- \rho_{\text{ads}} \sum_i H_i \frac{\partial q_i}{\partial t} + \frac{2h}{R_{\text{bed}}} (T - T_{\text{wall}}) = 0$	(3-6)

3.3.2 Parameters

The physical properties and design parameters, as well as the references for obtaining each value, are given in Table 3-2.

Table 3-2 Design and physical property parameters

Common for ELM-11 and zeolite 13X			ELM-11 only		
Parameters	Values	References	Parameters	Values	References
R_p	1.20×10^{-3} [m]	This study	ρ_{ads}	771 [kg _{ads} /m ³]	This study
ϵ_{bed}	0.348 [-]	This study	ρ_{pellet}	1.03×10^3 [kg/m ³]	This study*
R_{bed}	2.50×10^{-2} [m]	This study	C_{ps}	1010 [J/(kg·K)]	3, 4
L	1.00 [m]	This study	k_{CO_2}	0.0454 [1/s]	5
C_{pg}	996 [J/(kg·K)]	127,128	k_{N_2}	0.110 [1/s]	This study (Assumption 10)
D_L	1.08×10^{-4} [m ² /s]	129	H_{CO_2}	-25.4 [kJ/mol]	67
K_L	$\frac{0.0220}{1.72 \times 10^{-5}}$ [J/(m·s·K)]	130	H_{N_2}	-25.4 [kJ/mol]	This study (Assumption 10)
μ	1.72×10^{-5} [kg/(m·s)]	131,132	zeolite 13X only		
ρ_{wall}	7800 [kg/m ³]	35	Parameters	Values	References
h	60 [J/(m ² ·s·K)]	35	ρ_{ads}	1.06×10^3 [kg _{ads} /m ³]	35
			ρ_{pellet}	1.06×10^3 [kg/m ³]	35
			C_{ps}	504 [J/(kg·K)]	35
			k_{CO_2}	0.0210 [1/s]	133
			k_{N_2}	0.110 [1/s]	133
			H_{CO_2}	-35.0 [kJ/mol]	133
			H_{N_2}	-23.0 [kJ/mol]	133

* The density of ELM-11 pellet is estimated from experimentally measured true density values of ELM-11 and cellulose (1570 kg_{ads}/m³, and 1600 kg/m³,¹³⁴ respectively) and the assumed porosity of the column ϵ_{bed} , 0.348. Since ELM-11 is not porous in the closed state, the internal porosity of ELM-11 was ignored.

3.3.3 Performance indicators

This study evaluates the performance of the process using the following four indicators: the recovery rate and purity of the product CO₂ gas recovered, bed size factor, and power consumption in electricity.

CO₂ recovery and purity

The CO₂ recovery rate and CO₂ product purity are obtained as follows. The following equation gives the CO₂ recovery:

$$\text{Recovery} = \frac{\text{product}}{\text{feed}}, \quad (3-7)$$

where feed [molCO₂] is the amount of CO₂ feed gas in one cycle at a cyclic steady state, and product [molCO₂] is the amount of CO₂ product gas in the cycle. The CO₂ product purity is given as:

$$\text{Purity} = \frac{\text{product}}{\text{product+impurity}}, \quad (3-8)$$

where impurity [molN₂] is the amount of N₂ gas in the CO₂ product in the cycle. The above product, feed, and impurity can be obtained from the equations shown in Table 3-3.

Table 3-3 Mole flux variables at each operating step

Step 1 pressurization	Step 2 adsorption	Step 3 depressurization	Step 4 desorption
$\frac{\partial(\text{feed})}{\partial t}$ $= \pi R_{\text{bed}}^2 \varepsilon_{\text{bed}} \frac{u p_{\text{CO}_2}}{RT} \Big _{z=0}$	$\frac{\partial(\text{feed})}{\partial t}$ $= \pi R_{\text{bed}}^2 \varepsilon_{\text{bed}} \frac{u p_{\text{CO}_2}}{RT} \Big _{z=0}$	$\frac{\partial(\text{feed})}{\partial t} = 0$	$\frac{\partial(\text{feed})}{\partial t} = 0$
$\frac{\partial(\text{product})}{\partial t} = 0$	$\frac{\partial(\text{product})}{\partial t} = 0$	$\frac{\partial(\text{product})}{\partial t} = 0$	$\frac{\partial(\text{product})}{\partial t}$ $= -\pi R_{\text{bed}}^2 \varepsilon_{\text{bed}} \frac{u p_{\text{CO}_2}}{RT} \Big _{z=0}$
$\frac{\partial(\text{impurity})}{\partial t} = 0$	$\frac{\partial(\text{impurity})}{\partial t} = 0$	$\frac{\partial(\text{impurity})}{\partial t} = 0$	$\frac{\partial(\text{impurity})}{\partial t}$ $= -\pi R_{\text{bed}}^2 \varepsilon_{\text{bed}} \frac{u p_{\text{N}_2}}{RT} \Big _{z=0}$

Bed size factor

One of the performance indicators, bed size factor (BSF) [$\text{kg}_{\text{ads}}/\text{TPDCO}_2$], is reciprocal of the amount of CO_2 obtained from the adsorbent per unit weight and unit time, and is expressed by the following equation:

$$\text{BSF}[\text{kg}_{\text{ads}}/\text{TPDCO}_2] = \frac{m_{\text{ads}} \cdot t_{\text{cycle}}}{Mw_{\text{CO}_2} \cdot \text{product}} \times \frac{10^6}{24 \times 3600}, \quad (3-9)$$

where m_{ads} [kg_{ads}] is weight of adsorbent packed in the column without cellulose, which is a binder; t_{cycle} [s] is cycle time; product [$\text{molCO}_2/\text{cycle}$] is the amount of CO_2 product in one cycle at a cyclic steady state.

Power consumption

One of the performance indicators, power consumption [GJ_e/tonCO₂], is the amount of *electrical* energy for compressing and vacuuming per recovered unit weight of CO₂, which is given by the following equation:

$$\begin{aligned} & \text{Power Consumption [GJ}_e\text{/tonCO}_2\text{]} \\ &= \frac{1}{M_{w_{\text{CO}_2}} \text{product}} \left(\int_0^{t_{\text{press}} + t_{\text{ads}}} \text{Power}_{\text{compressor}} dt + \int_{t_{\text{press}} + t_{\text{ads}} + t_{\text{depress}}}^{t_{\text{press}} + t_{\text{ads}} + t_{\text{depress}} + t_{\text{des}}} \text{Power}_{\text{vacuum}} dt \right), \end{aligned} \quad (3-10)$$

where $M_{w_{\text{CO}_2}}$ [g/molCO₂] is molecular weight of CO₂, and its value is 44.01; product [molCO₂] is the amount of CO₂ product in one cycle at a CCS; Power_{compressor} [kW] and Power_{vacuum} [kW] are the electrical power consumption for the compressor and the vacuum pump, respectively, which are given by:

$$\text{Power}_{\text{compressor}} [\text{kW}] = \frac{1}{\eta_{\text{compressor}}} P \Big|_{z=0} \frac{\gamma}{\gamma-1} u \pi R_{\text{bed}}^2 \varepsilon_{\text{bed}} \left[\left(\frac{P_{\text{feed}}}{P_{\text{atm}}} \right)^{\frac{\gamma-1}{\gamma}} - 1 \right], \quad (3-11)$$

$$\text{Power}_{\text{vacuum}} [\text{kW}] = \frac{1}{\eta_{\text{vacuum}}} P \Big|_{z=0} \frac{\gamma}{\gamma-1} u \pi R_{\text{bed}}^2 \varepsilon_{\text{bed}} \left[\left(\frac{P_{\text{atm}}}{P_{\text{des}}} \right)^{\frac{\gamma-1}{\gamma}} - 1 \right], \quad (3-12)$$

where $\eta_{\text{compressor}}$ and η_{vacuum} are the efficiency of the compressor and the vacuum pump, respectively.

Specific values of these parameters are given in Sections 3.4.2 and 3.4.3. Note that the power consumption of the compressor can be a pessimistic value: the energy to pressurize the feed gas may partially be supplied by recovered mechanical energy from the exhaust gas released during the adsorption and depressurization steps, where the pressure remains high, if a turbine is installed.^{135,136}

Some of the operations in this study require energy to cool the gas and column to ambient temperature or below, but the cooling energy is not taken into account; the flue gas temperature needs to be reduced, where the compression heat may need to be removed. For example, in the case with a temperature of 263 K and a feed pressure of 516 kPa, the amount of compression heat to be removed is 0.742 GJ/tonCO₂. However, the cooling energy for the feed gas may be saved substantially by heat exchange with the exhaust gas emitted in the adsorption and depressurization steps as well as with the recovered gas.¹³⁷

3.4 Operational conditions

3.4.1 Boundary conditions

The boundary conditions are shown in Table 3-4. The boundary condition $dP/dz|_{z=0} = (P_{\text{feed}} - P_{\text{des}})/t_{\text{ads}}$ in Step 1 indicates that the inlet pressure changes linearly from P_{des} to P_{feed} over t_{ads} seconds. The purpose of this boundary condition is to help convergence in solving PDAEs by changing the inlet pressure gradually. The value of $dP/dz|_{z=0}$ in Steps 3 and 4 is set for the same reason. Similarly, a numerical buffer, Step 5, is implemented as a technique to help the convergence. More details are given in Section 3.5.1.

Table 3-4 Boundary conditions

Step 1 Pressurization	Step 2 Adsorption	Step 3 Depressurization	Step 4 Desorption	Step 5 Numerical buffer
$y_i _{z=0} = y_{\text{feed},i}$	$y_i _{z=0} = y_{\text{feed},i}$	$\frac{\partial y_i}{\partial z} _{z=0} = 0$	$\frac{\partial y_i}{\partial z} _{z=0} = 0$	$\frac{\partial y_i}{\partial z} _{z=0} = 0$
$\frac{\partial y_i}{\partial z} _{z=L} = 0$	$\frac{\partial y_i}{\partial z} _{z=L} = 0$	$\frac{\partial y_i}{\partial z} _{z=L} = 0$	$\frac{\partial y_i}{\partial z} _{z=L} = 0$	$\frac{\partial y_i}{\partial z} _{z=L} = 0$
$T _{z=0} = T_{\text{feed}}$	$T _{z=0} = T_{\text{feed}}$	$\frac{\partial T}{\partial z} _{z=0} = 0$	$\frac{\partial T}{\partial z} _{z=0} = 0$	$\frac{\partial T}{\partial z} _{z=0} = 0$
$\frac{\partial T}{\partial z} _{z=L} = 0$	$\frac{\partial T}{\partial z} _{z=L} = 0$	$\frac{\partial T}{\partial z} _{z=L} = 0$	$\frac{\partial T}{\partial z} _{z=L} = 0$	$\frac{\partial T}{\partial z} _{z=L} = 0$
$\frac{\partial u}{\partial z} _{z=0} = 0$	$\frac{\partial u}{\partial z} _{z=0} = 0$	$\frac{\partial u}{\partial z} _{z=0} = 0$	$\frac{\partial u}{\partial z} _{z=0} = 0$	$\frac{\partial u}{\partial z} _{z=0} = 0$
$u _{z=L} = 0$	$u _{z=L} = u_{\text{outlet}}$	$u _{z=L} = 0$	$u _{z=L} = 0$	$u _{z=L} = 0$
$\frac{\partial P}{\partial z} _{z=0} = \frac{(P_{\text{feed}} - P_{\text{des}})}{t_{\text{ads}}}$	$P _{z=0} = P_{\text{feed}}$	$\frac{\partial P}{\partial z} _{z=0} = \frac{(P_{\text{atm}} - P_{\text{feed}})}{t_{\text{depress}}}$	In the first t_{trans} seconds,* $\frac{\partial P}{\partial z} _{z=0} = \frac{(P_{\text{des}} - P_{\text{atm}})}{t_{\text{trans}}}$.	$\frac{\partial P}{\partial z} _{z=0} = 0$
			Afterward, $P _{z=0} = P_{\text{des}}$.	
$\frac{\partial P}{\partial z} _{z=L} = 0$	$\frac{\partial P}{\partial z} _{z=L} = 0$	$\frac{\partial P}{\partial z} _{z=L} = 0$	$\frac{\partial P}{\partial z} _{z=L} = 0$	$\frac{\partial P}{\partial z} _{z=L} = 0$

* t_{trans} [s] is transition time for the column inlet pressure from atmospheric pressure to desorption pressure.

3.4.2 Common parameters for all cases

Operating condition parameters employed commonly in all simulation cases are shown in Table 3-5. The four parameters were determined empirically: pressurization time (t_{press}), depressurization time (t_{depress}), transition time (t_{trans}), and molar flow rate at the outlet (Q_{outlet}). The step times, t_{press} , t_{depress} , and t_{trans} would be determined by the performance of the hardware, such as the vacuum pump, compressor, as well as pipe inner diameters. It was found that assigning larger values to t_{depress} and t_{trans} avoid rapid pressure changes and thus improves numerical stability. Shortening these values by employing a potentially advanced numerical scheme will be our future work. The compressor efficiency was determined based on the data reported by Campbell.¹³⁸ A two-stage compressor may be used in high-pressure operations.

Table 3-5 Operational condition parameters for all cases

Parameters	Values
$y_{i,\text{feed}}$	0.80 ($i = \text{N}_2$), 0.20 ($i = \text{CO}_2$)
t_{press}	30 [s]
depress	100 [s]
t_{trans}	300 [s]
Q_{outlet}	0.0477 [mol/s]
$\eta_{\text{compressor}}$	0.750 [-]

3.4.3 Vacuum pump efficiency

The efficiency of the vacuum pump was determined using the empirical model for the ELRS-60 vacuum water-ring pump at 420 rpm.¹³⁹ In this model, the efficiency is expressed as a function of desorption pressure. Figure 3-2 shows the efficiency values versus desorption pressure.

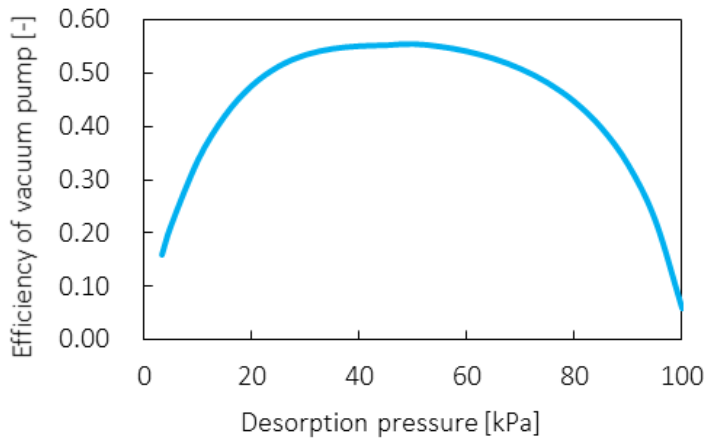


Figure 3-2. Vacuum pump efficiency against desorption

3.4.4 Adsorption time

The following algorithm is used to determine the adsorption time. In this algorithm, the adsorption step continues until the CO₂ partial pressure at the outlet reaches a target value, $p_{\text{CO}_2, \text{tar}}$ (Figure 3-3 (a)).

Step 1. Run the adsorption step for 10 seconds.

Step 2. If the CO₂ partial pressure at the outlet is above $p_{\text{CO}_2, \text{tar}}$, the adsorption step is terminated.

Otherwise, return to Step 1.

The foot CO₂ pressure $p_{\text{foot, ads}}$ is used as the value of $p_{\text{CO}_2, \text{tar}}$ for ELM-11, while 25 kPa is used for zeolite 13X. These values of $p_{\text{CO}_2, \text{tar}}$ were chosen to achieve sufficiently high recovery for ELM-11 and purity for zeolite 13X.

3.4.5 Desorption time

The following algorithm is used to determine the desorption time. In this algorithm, the desorption step continues until the amount of CO₂ adsorbed at the column inlet reaches a target value $p_{\text{CO}_2, \text{tar}}$ (Figure 3-3 (b)).

Step 1. Run the desorption process for 50 seconds.

Step 2. If the amount of CO₂ adsorbed at the column inlet is below $p_{\text{CO}_2, \text{tar}}$, the desorption step is terminated. Otherwise, return to Step 1.

It was also assumed that the desorption time cannot be shorter than 300 seconds.

The target value $p_{\text{CO}_2, \text{tar}}$ is expressed using desorption ratio r_d as follows:

$$q_{\text{CO}_2, \text{tar}} = r_d q_{\text{eq, ads}} + (1 - r_d) q_{\text{eq, des}}, \quad (3-13)$$

where $q_{\text{eq, ads}} = q_{\text{CO}_2}^* \Big|_{p_{\text{CO}_2} = y_{\text{feed, CO}_2} p_{\text{feed}}}$ [molCO₂/kg_{ads}] is equilibrium amount of CO₂ adsorbed during the adsorption step, and $q_{\text{eq, des}} = q_{\text{CO}_2}^* \Big|_{p_{\text{CO}_2} = p_{\text{des}}}$ [molCO₂/kg_{ads}] is equilibrium amount of CO₂ adsorbed during the desorption step. To obtain the optimal value of r_d that maximizes the CO₂ recovery rate, the grid search method is used as shown in Section 3.6.5.

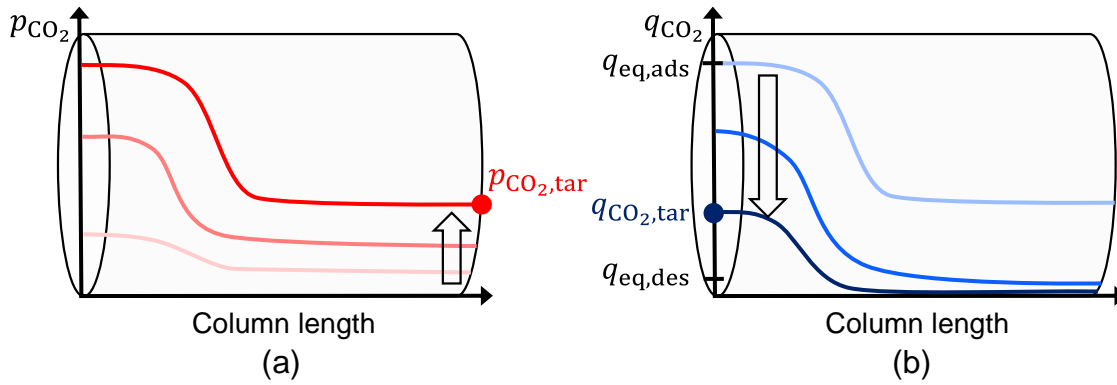


Figure 3-3. Time transitions in the column: (a) CO₂ partial pressure at the outlet approaching $p_{CO_2,tar}$; (b) amount of CO₂ adsorbed at the inlet approaching $q_{CO_2,tar}$.

3.4.6 Desorption pressure

The desorption pressure, one of the operational conditions, is determined using *foot CO₂ pressures*, $p_{foot,ads}(T)$ and $p_{foot,des}(T)$, defined as threshold values of the CO₂ pressure at the foot of the adsorption and desorption isotherms at a certain temperature T , respectively. These parameters are the pressures at which the amount of CO₂ adsorbed reaches 2% of the saturated amount n_U^∞ , as shown in Figure 3-4. To avoid an impractically long desorption time to reach the equilibrium, the desorption pressure should be smaller than $p_{foot,des}(T_{wall})$. I empirically chose the desorption pressure value as $P_{des} = 0.55 p_{foot,des}(T_{wall})$.

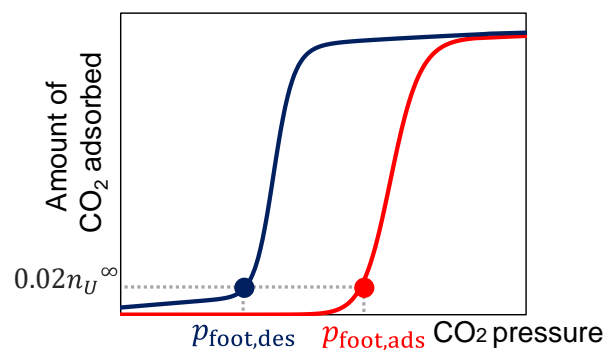


Figure 3-4. Foot CO₂ pressures, $p_{foot,ads}$ and $p_{foot,des}$

3.4.7 Operation method to increase purity for zeolite 13X

Unlike ELM-11, zeolite 13X adsorbs N₂, resulting in lower CO₂ purity in the product gas when the same operations as above are implemented. To compare the performance under similar purity values, the VPSA process using zeolite 13X is assumed to discard the gas that comes out during the first 300 seconds of the desorption step, where the N₂ concentration is high so that the CO₂ product purity of 99% is achieved.

3.4.8 Determination of cyclic steady state (CSS)

In this paper, the VPSA process is assumed to be in CSS when the following conditions are met:

The squared errors of temperature T [K], mole fraction y_i [-], and amount adsorbed q_i [mol/kg_{ads}] at the end of the cycle compared to the values in a previous cycle are smaller than tolerances, ε_T , ε_y , and ε_q , respectively.

$$\begin{aligned}\sum_{z=0}^L \left(T(z) \Big|_{t=t_{\text{cycle}}} - T(z) \Big|_{t=0} \right)^2 &< \varepsilon_T, \\ \sum_{z=0}^L \left(y_i(z) \Big|_{t=t_{\text{cycle}}} - y_i(z) \Big|_{t=0} \right)^2 &< \varepsilon_y, \\ \sum_{z=0}^L \left(q_i(z) \Big|_{t=t_{\text{cycle}}} - q_i(z) \Big|_{t=0} \right)^2 &< \varepsilon_q.\end{aligned}\tag{3-14}$$

The tolerances are chosen as follows: $(\varepsilon_T, \varepsilon_y, \varepsilon_q) = (10^{-3}, 10^{-5}, 10^{-5})$.

3.5 Techniques for converging the PDAEs

ELM-11 shows sigmoidal adsorption isotherms and hysteresis, which causes a sudden change in CO₂ adsorption amount and partial pressure. This makes converge in solving PDAEs difficult. To address this problem, the following numerical techniques presented were employed.

3.5.1 Artificial buffer step

To handle the numerical difficulty in solving the PDAEs, an artificial buffer step, Step 5, is considered as shown in Table 3-4. This is a step to smoothen the change in the mole fraction y_i from Step 4 to Step 1, where the numerical solver often fails. In this step, I approximate the dynamics in the column by replacing the component mass balance (Eq. (3-2)) and overall mass balance (Eq. (3-3)) by the following equations, respectively:

$$\frac{\partial y_i}{\partial t} = \frac{y_{\text{end},i} - y_{\text{feed},i}}{t_{\text{buffer}}}, \quad (3-15)$$

$$\frac{\partial P}{\partial t} = 0, \quad (3-16)$$

where $y_{\text{end},i}$ [-] is mole fraction of component i at the end time of Step 4; t_{buffer} [s] is numerical buffer time (10 seconds). Note that the influence of this step on the CO₂ mass balance is negligible, since the amount of CO₂ that remains in the column during this step is very small and the duration is short.

3.5.2 Continuation in adsorption isotherms

Another technique is based on the pseudo transient continuation, which is a technique for solving PDAEs where the initial values are far from the solutions.⁸⁸ In order to slow the slope of the adsorption/desorption isotherms, imaginary linear isotherms $q^*_{\text{linear},j}$ [molCO₂/kg_{ads}] ($j = (\text{ads}, \text{des})$), are used at the beginning of the simulation, and they are transitioned to the actual adsorption isotherm $q^*_{\text{actual},j}$ [molCO₂/kg_{ads}] over t_{shift} seconds (see Figure 3-5):

$$q^*_{\text{CO}_2} = q^*_{\text{actual},j} \cdot x + q^*_{\text{linear},j} \cdot 1 - x ,$$

$$x = \begin{cases} 1 & \text{if } t_{\text{shift}} \leq \text{Time} \\ \text{Time}/t_{\text{shift}} & \text{if } 0 \leq \text{Time} < t_{\text{shift}} \end{cases} , \quad (3-17)$$

$$q^*_{\text{linear},j} = \min \left(0, \frac{n_U^\infty}{p_{\text{feed,CO}_2} - p_{\text{step},j}} p_{\text{CO}_2} - p_{\text{step},j} \right) ,$$

where x [-] is binary variable to switch between $q^*_{\text{linear},j}$ and $q^*_{\text{actual},j}$; Time [s] is total time; t_{shift} [s] is shifting time from the linear isotherms to the actual isotherms (3000 seconds).

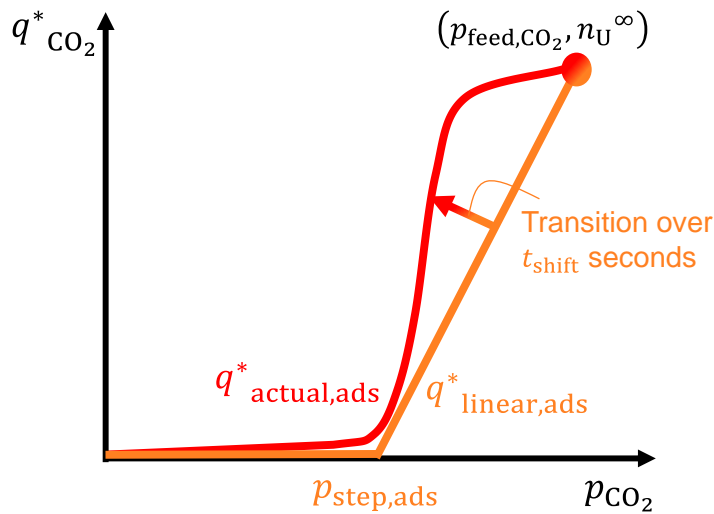


Figure 3-5. Adsorption/desorption isotherms transition over time

3.6 Simulation results

In this section, the results of the simulations are shown under various operating conditions, such as different temperatures and feed pressures. Note that the adsorption isotherms of ELM-11 are known to show “double-step” at low temperatures and high CO₂ partial pressures,⁶⁷ but it does not occur under the operating conditions shown in this paper. For example, according to the data measured by Ichikawa *et al.*, the double-step occurs at a CO₂ partial pressure of 980 kPa at a temperature of 273 K.⁸⁰ The maximum CO₂ partial pressure in our operations is 400 kPa, which is much smaller than the value.

3.6.1 Ambient temperature

This section shows results for cases where the feed gas and column wall temperature are set to the ambient temperature of 298.15 K, while the feed pressure is varied. The four performance indicators of the process are calculated for seven different feed pressures, and the results are shown in Figure 3-6. This figure shows significant changes in the CO₂ recovery rate, BSF, and power consumption by changing the feed pressure.

Figure 3-6 (a) shows that recovery rate can be increased substantially by employing a higher feed pressure. To reduce the slipping-off, the partial pressure of CO₂ must exceed the foot CO₂ pressure $p_{\text{foot,ads}}$ sufficiently. Therefore, the extent to which the feed CO₂ pressure exceeds $p_{\text{foot,ads}}$ significantly influences the recovery rate. For example, in Case 3, the feed CO₂ pressure is $p_{\text{feed,CO}_2} = P_{\text{feed}}y_{i,\text{feed}} = 400 \times 0.20 = 80$ kPa, which is only about 1.2 times higher than $p_{\text{foot,ads}}(298.15 \text{ K})$ of 67 kPa. At such a

low partial pressure of CO₂, most of the CO₂ fed to the column slips through, resulting in a low recovery rate of only 25.5%. On the other hand, the feed CO₂ pressure $p_{\text{feed,CO}_2}$ in Case 4 is 200 kPa, which is 3.0 times higher than $p_{\text{foot,ads}}(298.15 \text{ K})$ and thus causes stronger adsorption, resulting in a significantly higher recovery rate of 67.8%.

Based on the slipping-off mechanism, I attempt to estimate the recovery rate can by a linear approximation formula as follows:

$$\text{Estimated recovery} = \frac{p_{\text{feed,CO}_2} - p_{\text{foot,ads}}(T_{\text{wall}})}{p_{\text{feed,CO}_2}} \times 100[\%], \quad (3-18)$$

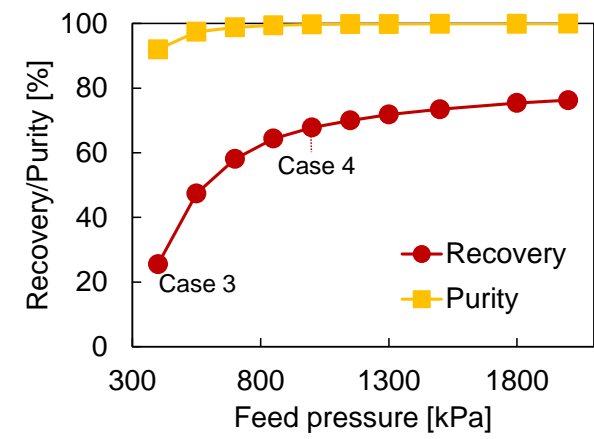
where the numerator, $p_{\text{feed,CO}_2} - p_{\text{foot,ads}}(T_{\text{wall}})$, is the amount of CO₂ adsorbed that exceeds the foot pressure at T_{wall} to the feed partial pressure $p_{\text{feed,CO}_2}$. Figure 3-6 (b) shows a plot to validate the estimation given by (3-18), which shows the formula gives reasonable estimation. The slight deviation between the two is caused by the adsorption/desorption heat, which causes a shift in the foot CO₂ pressure. From the equation of the recovery estimation, it can be seen that increasing the feed pressure or decreasing the foot CO₂ pressure are effective approaches to increase the recovery rate. This strategy can be a simple and useful approach when analyzing the slipping-off problem of flexible MOFs.

Figure 3-6 (a) also shows that the product purity of CO₂ gas is high in all cases, especially in cases where the feed pressure exceeds 850 kPa, showing values of over 99.0%. That is because ELM-11 hardly adsorbs N₂, and most of the recovered gas is CO₂. However, in Case 3, the purity value of 92.0% was relatively small because the feed pressure is low, and the amount of CO₂ adsorbed in the column is small.

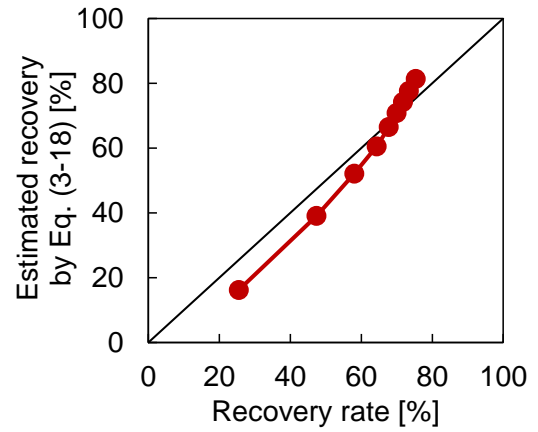
Increasing the feed pressure is not necessarily the optimum in terms of the power consumption per unit weight of CO₂ recovered. Figure 3-6 (c) shows that the power consumption is the lowest when the feed pressure is 700 kPa. This optimum is found in the balance of CO₂ yield and power consumption for the compressor. If the feed pressure is higher than 700 kPa, the compressor power consumption is significantly large, increasing the sum of power consumption.

Figure 3-6 (d) shows that BSF changes significantly as a function of feed pressure, showing a 9-fold difference between Cases 3 and 4, which can be explained by two effects. One is the difference in the volume of CO₂ fed per cycle. The volume of CO₂ fed per cycle is proportional to the adsorption time. Therefore, the difference in the volume is due to the timing of stopping the adsorption process when the CO₂ partial pressure at the outlet exceeds a certain threshold, as described in Section 3.4.4; in Case 3, the amount of CO₂ adsorbed is small due to the low feed pressure, resulting in the outlet CO₂ partial pressure reaching the threshold early and ending the adsorption process. The other effect that influences BSF is the recovery rate; a higher recovery rate increases the amount of CO₂ processed per unit weight of adsorbent.

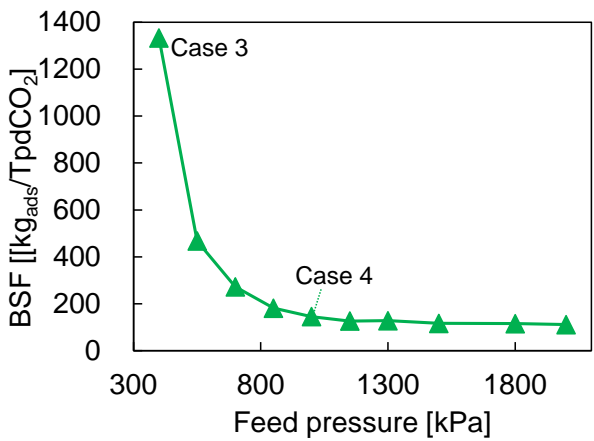
These cases include extrapolation of the isotherm model, which is based on data up to 298 K, towards the higher temperature region because the adsorbent may be heated due to the heat of adsorption. However, the effect of this extrapolation towards higher temperature on our simulation is probably insignificant; in the next section, the optimal operations are shown to be in a lower-temperature range, and thus the extrapolation is unnecessary under those optimal conditions.



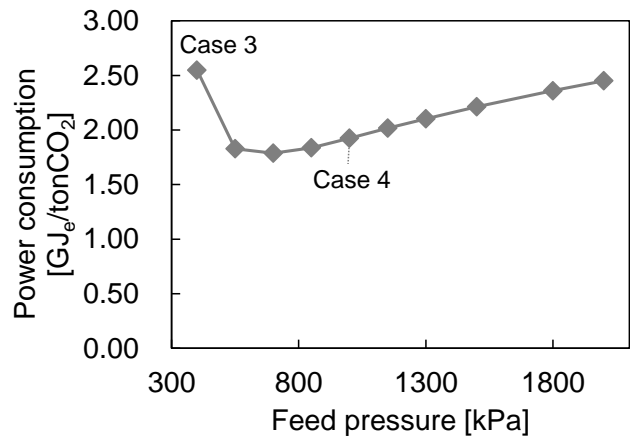
(a)



(b)



(c)



(d)

Figure 3-6. Performance indicators change with feed pressure at ambient temperature: (a) recovery rate and purity; (b) recovery rate vs. recovery estimation given by Eq. (3-18); (c) power consumption; (d) BSF.

3.6.2 Influence of temperature

Relationship between power consumption against operating temperature is shown in Figure 3-7. In this analysis, the feed pressure, $p_{\text{feed,CO}_2}$, was determined by Eq. (3-18) so that the estimated recovery is 80.0%. Figure 3-7 shows that the lower the temperature, the greater the recovery. At a temperature of 263 K, a recovery rate of 84.5% is achieved.

In Figure 3-7, the lower the temperature, the lower the power consumption for the compressor becomes. This is because lowering the temperature reduces the foot CO₂ pressure, $p_{\text{foot,ads}}$, and thus the feed pressure $p_{\text{feed,CO}_2}$ can be reduced without sacrificing the recovery, as seen in Eq. (3-18). Reduction in $p_{\text{feed,CO}_2}$ has a substantial effect on the power consumption of the compressor. For example, by decreasing the temperature from 298 K to 263 K, the power consumption can be lowered by 44% (from 2.36 GJ_e/tonCO₂ to 1.33 GJ_e/tonCO₂) because the feed pressure can be reduced from 1800 kPa to 516 kPa.

On the other hand, lowering the temperature increases the power consumption for the vacuum pump, as can also be seen in Figure 3-7. This is because an even lower pressure (deep vacuum) is needed to carry out desorption at lower temperatures. A deep vacuum operation sacrifices the efficiency of the vacuum pump, and increases its power consumption. For example, by decreasing the temperature from 298 K to 263 K, the desorption pressure must be reduced from 26.4 kPa to 8.14 kPa, where the efficiency of the vacuum pump reduces from 0.520 to 0.298. This substantial

decrease in the pump efficiency leads to an increase in the power consumption from 0.16 GJ_e/tonCO₂ to 0.52 GJ_e/tonCO₂.

The sum of power consumption of the compressor and the vacuum pump is the lowest when the temperature is at 263 K (1.33 GJ_e/tonCO₂). It should be noted that the optimal temperature found above is based on the assumptions for the efficiency of the compressor and vacuum pump. Furthermore, the additional energy needed to cool the adsorption column and supplied gas is not taken into account. The operating temperature should be decided carefully considering these uncertainties. Finally, lowering the operating temperature further to below 263 K may give an even lower power consumption, which I do not pursue in this study due to the lack of isotherm data.

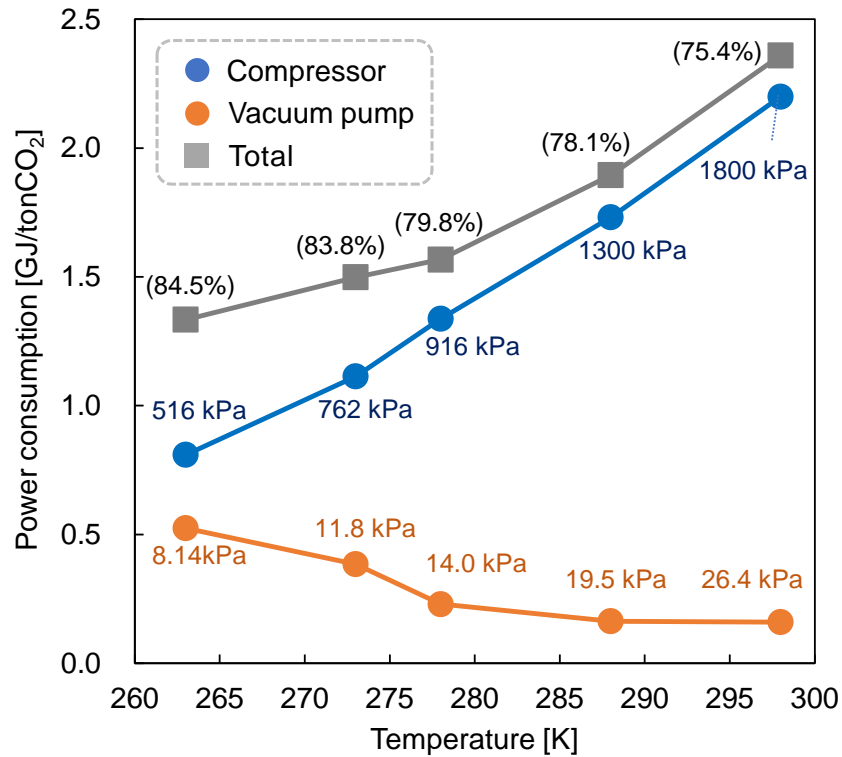


Figure 3-7. Power consumption as a function of feed and column wall temperature. Blue, orange, and black scripts in brackets are feed pressure, desorption pressure, and recovery rate, respectively.

3.6.3 Comparison with zeolite 13X

This section discusses a comparison between ELM-11 and zeolite 13X. The adsorption isotherm for zeolite 13X is shown in Figure 3-8. The isotherm model and its parameters were taken from the temperature-dependent Sips model shown by Park *et al.*¹³³ The detailed operating conditions and results are shown in Table 3-8 in Section 3.6.7 (Case 4 is for ELM-11 and Case 5 is for zeolite 13X).

Figure 3-9 (a) shows that the desorption step is shorter for ELM-11 than for zeolite 13X (350 s for ELM-11 vs. 1450 s for zeolite 13X) because ELM-11 has a higher mass transfer rate between the gas and adsorbent phases. The faster mass transfer in ELM-11 is caused by the greater driving force $q_{\text{CO}_2}^* - q_{\text{CO}_2}$ of the LDF model because for ELM-11, $q_{\text{CO}_2}^*$ is always nearly zero during the desorption step, owing to the sigmoidal isotherm shape. Note that in another case study in Section 3.2, the mass transfer coefficient of ELM-11 was set to the same value as zeolite 13X. It was found that the faster mass transfer of ELM-11 is *not* due to the difference in the mass transfer coefficient, but due to the difference in the *driving force*.

Additionally, the influence of the temperature drop during the desorption step, which lowers the driving force for zeolite 13X, is less significant for ELM-11. Figure 3-10 illustrates the desorption isotherms of zeolite 13X and ELM-11 during the desorption step: the light-blue lines are the isotherms at the temperature T_{low} that was lowered by the desorption heat, and the purple lines are the isotherms at the ambient temperature T_{amb} ($T_{\text{low}} < T_{\text{amb}}$). As shown in Figure 3-10 (a), the driving force, $q_{\text{CO}_2} - q_{\text{CO}_2,\text{tar}}$ of the zeolite 13X decreases as the temperature decreases to T_{low} , and thus the desorption rate becomes slower. On the other hand, as shown in Figure 3-10 (b), the driving force of ELM-11 remains nearly constant because of the sigmoidal shape of the isotherm; the equilibrium adsorption amount at P_{des} remains nearly zero even at the lower temperature T_{low} .

The temperature dependence of the driving force causes the significant difference in the desorption time between zeolite 13X and ELM-11.

Figure 3-9 (a) also shows the BSF for ELM-11, $145 \text{ kg}_{\text{ads}}/\text{TPDCO}_2$, is much smaller than that for zeolite 13X, $677 \text{ kg}_{\text{ads}}/\text{TPDCO}_2$. The difference is caused by four factors in Eq. (3-9): 1. the shorter desorption time (300 s for ELM-11 vs. 1450 s for zeolite 13X), 2. a larger amount of CO_2 product in one cycle (5.20 molCO_2 for ELM-11 vs. 4.21 molCO_2 for zeolite 13X), 3. higher recovery rate (67.8% for ELM-11 vs. 55.9% for zeolite 13X, as shown in Figure 3-9 (b)), and 4. a smaller amount of adsorbent in the column ($771 \text{ kg}_{\text{ads}}/\text{m}^3$ for ELM-11 vs. $1060 \text{ kg}_{\text{ads}}/\text{m}^3$ for zeolite 13X).

Figure 3-9 (c) shows that the sum of power consumption of ELM-11, $1.92 \text{ GJ}_e/\text{tonCO}_2$, is lower than that of zeolite 13X, $3.17 \text{ GJ}_e/\text{tonCO}_2$. The lower power consumption of ELM-11 for the vacuum pump, $0.150 \text{ GJ}_e/\text{tonCO}_2$, is because of the relatively high desorption pressure, 26.4 kPa, which allows the vacuum pump to be operated at high efficiency, $\eta_{\text{vacuum}} = 0.52$. This efficient vacuum operation compensates the greater power consumption for the compressor to deliver the higher feed pressure of 1000 kPa. On the other hand, the larger power consumption of zeolite 13X for the vacuum pump, $2.51 \text{ GJ}_e/\text{tonCO}_2$, can be explained by the low desorption pressure, 3.30 kPa, which is needed to achieve the sufficient working capacity. At this low pressure, the efficiency of

the vacuum pump η_{vacuum} is as low as 0.16. Such an inefficient operation cannot be compensated by the relatively low power consumption by the compressor at the feed pressure of 250 kPa.

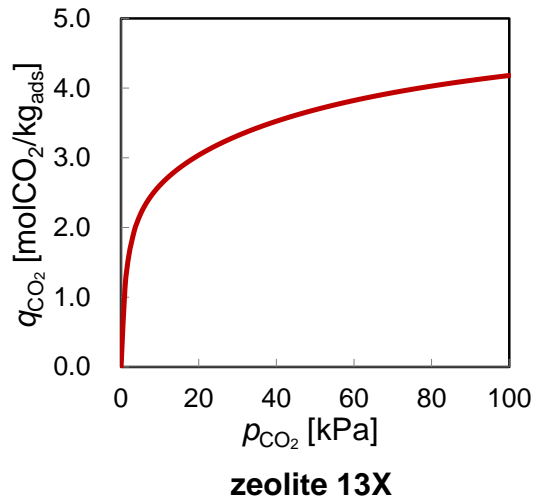


Figure 3-8. Isotherms of zeolite 13X at 298 K.

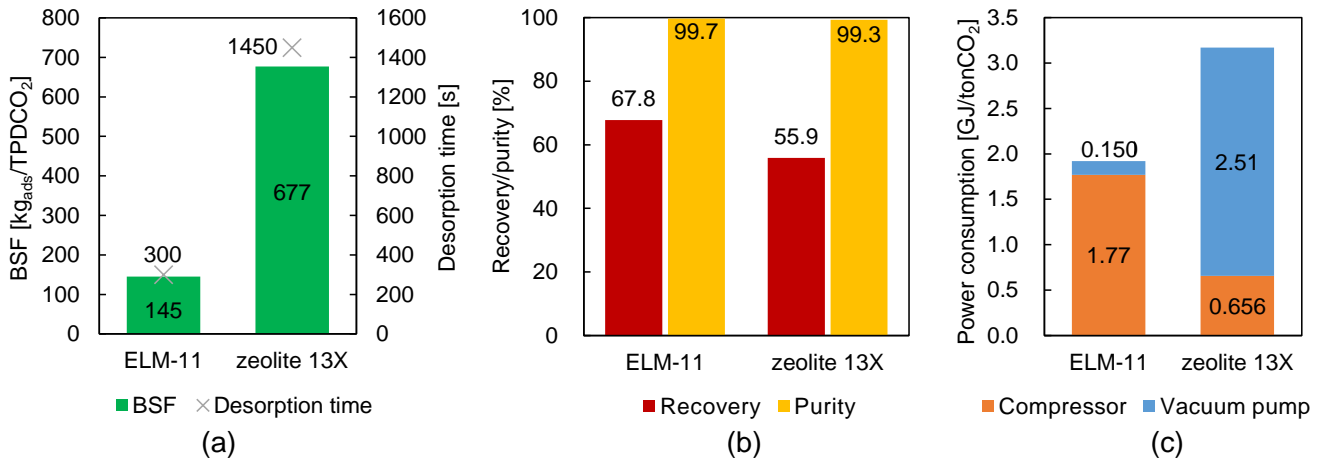


Figure 3-9. Comparison between ELM-11 and zeolite 13X at 298 K: (a) BSF and desorption time; (b) recovery and purity; (c) power consumption for compressor and vacuum pump.

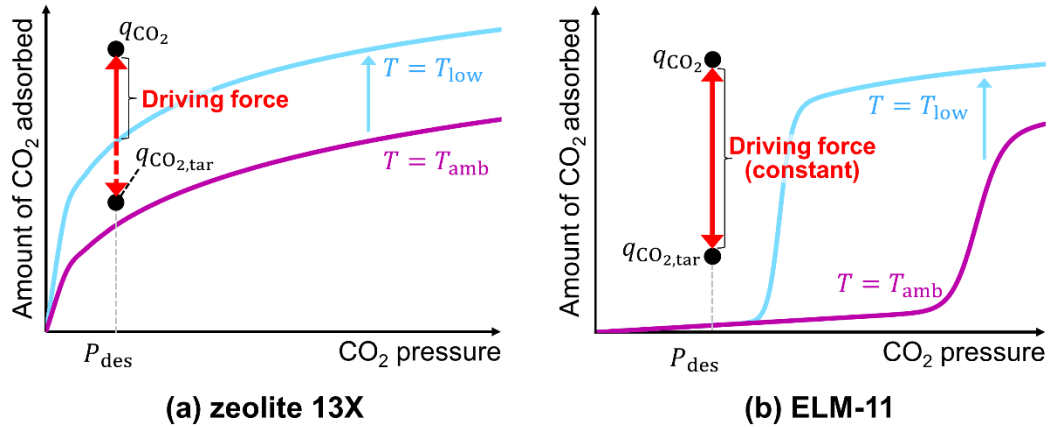


Figure 3-10. Temperature change effects on desorption time: (a) zeolite 13X with reduction in driving force; (b) ELM-11 without reduction in driving force.

Figure 3-11 shows CO₂ partial pressure and temperature profiles inside the column during the pressurization and adsorption steps, comparing ELM-11 and zeolite 13X. Due to the following properties of the sigmoidal adsorption isotherm, ELM-11 has sharp distributions: when CO₂ is fed to the column, only the part of CO₂ whose partial pressure exceeds the foot CO₂ pressure $p_{\text{foot,ads}}$ is adsorbed near the inlet, and the rest slips off. This property of slipping-off causes the saturated adsorption zone to gradually expand from the inlet while keeping the adsorption amount behind the zone low. On the other hand, zeolite 13X has a flat distribution as shown in the figure. This is because the adsorption occurs even at a relatively low partial pressure due to its Type-I isotherm, and thus adsorption occurs simultaneously throughout the column from the inlet to the outlet. Another reason is that the adsorption rate is lower than ELM-11 due to the smaller driving force $q^*_{\text{CO}_2} - q_{\text{CO}_2}$ caused by the large amount of CO₂ adsorbed in the column at the starting time of

cycles. Note that the profiles at $t = 0$ s are different between those for zeolite 13X and ELM-11 because of the cyclic steady states; the profiles at $t = 0$ are determined by $t = t_{\text{cycle}}$, in the previous cycle, where the two adsorbents show substantially different temperatures.

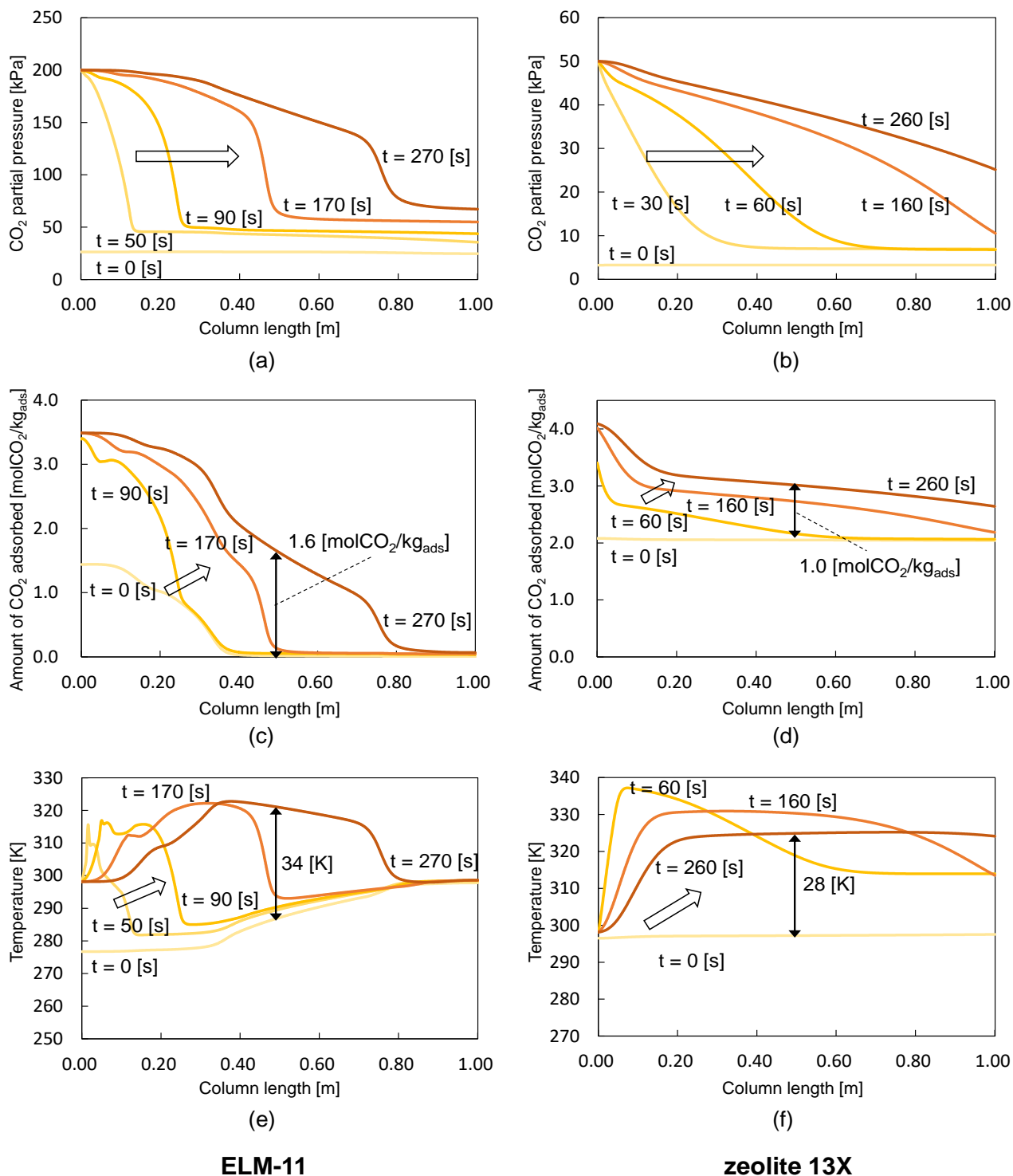
Figure 3-11 (a) and (b) show the internal CO₂ partial pressure profiles, where the influence of the isotherm shapes appears distinctively. Figure 3-11 (a) shows that because of the slipping-off, the CO₂ partial pressure for ELM-11 is always nearly flat near the column outlet, which elevates due to temperature increase as the adsorption operation continues. Figure 3-11 (b) shows that the partial pressure profile of CO₂ for zeolite 13X is flatter than that of ELM-11.

Figure 3-11 (c)–(f) show that the temperature change of ELM-11 is relatively small despite its large dynamic working capacity of CO₂: for example, the dynamic working capacities of ELM-11 and zeolite 13X at $z = 0.50$ m are 1.6 molCO₂/kg_{ads} and 1.0 molCO₂/kg_{ads}, respectively, while the temperature changes at the beginning of pressurization step and the end of adsorption step are 34 K and 28 K, respectively. This indicates that ELM-11 has a smaller ratio of temperature change to the dynamic working capacity of CO₂. This is because the CO₂ adsorption heat of ELM-11 is small due to the “intrinsic thermal management capabilities”,⁶⁷ and the N₂ adsorption heat of ELM-11 is almost negligible due to the small amount of N₂ adsorbed.

Note that the performance of the process may be highly dependent on the design and operation. Lu et al. experimentally investigated the CO₂ capture from gas with 15% CO₂ concentration using

zeolite 13X in a three-bed, eight-step VPSA process which involved purge, rinse, and pressure equalization steps. The results showed 73–82% purity and 85–95% recovery with a power consumption of 1.8–2.1 GJ_e/tonCO₂.¹⁴⁰ Krishnamurthy studied the basic four-step VSA process from gas with 15% CO₂ concentration using zeolite 13X and showed that 95.9 ± 1% purity, 86.4 ± 5.6% recovery with a productivity of 1.17 ± 0.07 TPDCO₂/m³_{ads} and power consumption of 1.70 ± 0.13 GJ_e/tonCO₂, which are measured in pilot plant experiments.⁵⁰ It should be noted that the comparison of ELM-11 and zeolite 13X in this study used a single-bed process to highlight the differences in the fundamental properties of the adsorbents.

I also note that the comparison above is based on some assumptions, which must be verified in future studies. In particular, the mass and heat transfer properties of ELM-11 are still being investigated. The value of the mass transfer coefficient k_{CO_2} was taken from Kondo *et al.*,¹²⁴ which was relatively insensitive to the simulation result, as shown in 3.2. The value used in this study was a conservative estimate, where the true value may be several times larger at low temperatures. Besides, the internal temperature profiles shown in Figure 3-11 (c) and (d) may be influenced by the axial thermal conductivity K_L , which was assumed to be dominated by the heat transfer in the gas phase. Further experimental investigations into heat and mass transfer are expected to confirm the potential advantages of ELM-11.



ELM-11

zeolite 13X

Figure 3-11. Profiles inside the column during pressurization and adsorption steps *in cycle steady states*: (a) CO₂ partial pressure for ELM-11; (b) CO₂ partial pressure for zeolite 13X; (c) amount of CO₂ adsorbed for ELM-11; (d) amount of CO₂ adsorbed for zeolite 13X; (e) temperature for ELM-11; (f) temperature for zeolite 13X. Vertical double-headed arrows at 0.5 m show changes from the beginning until the end of the steps.

3.6.4 Lower temperature, 273 K

The results in Section 3.6.2 indicate that ELM-11 performs better at lower temperatures, hence the cases at 273 K are shown in this section. The performance indicators are shown in Figure 3-12 and Table 3-6 below, while the feed pressure is varied. Figure 3-12 shows similar trends to the results shown in Figure 3-6; while the recovery rate and BSF depend highly on the feed pressure, the product purity is always high in all cases. As for the power consumption, Case 6, with the feed pressure of 200 kPa, shows the optimum value, 1.00 GJ_e/tonCO₂. However, this case has a low recovery rate of 36.2%, suggesting that higher feed pressure may need to be employed. For example, in Case 7, with the feed pressure of 300 kPa, the power consumption remains low and is close to the optimum value, while the recovery ratio is substantially higher and BSF is significantly lower.

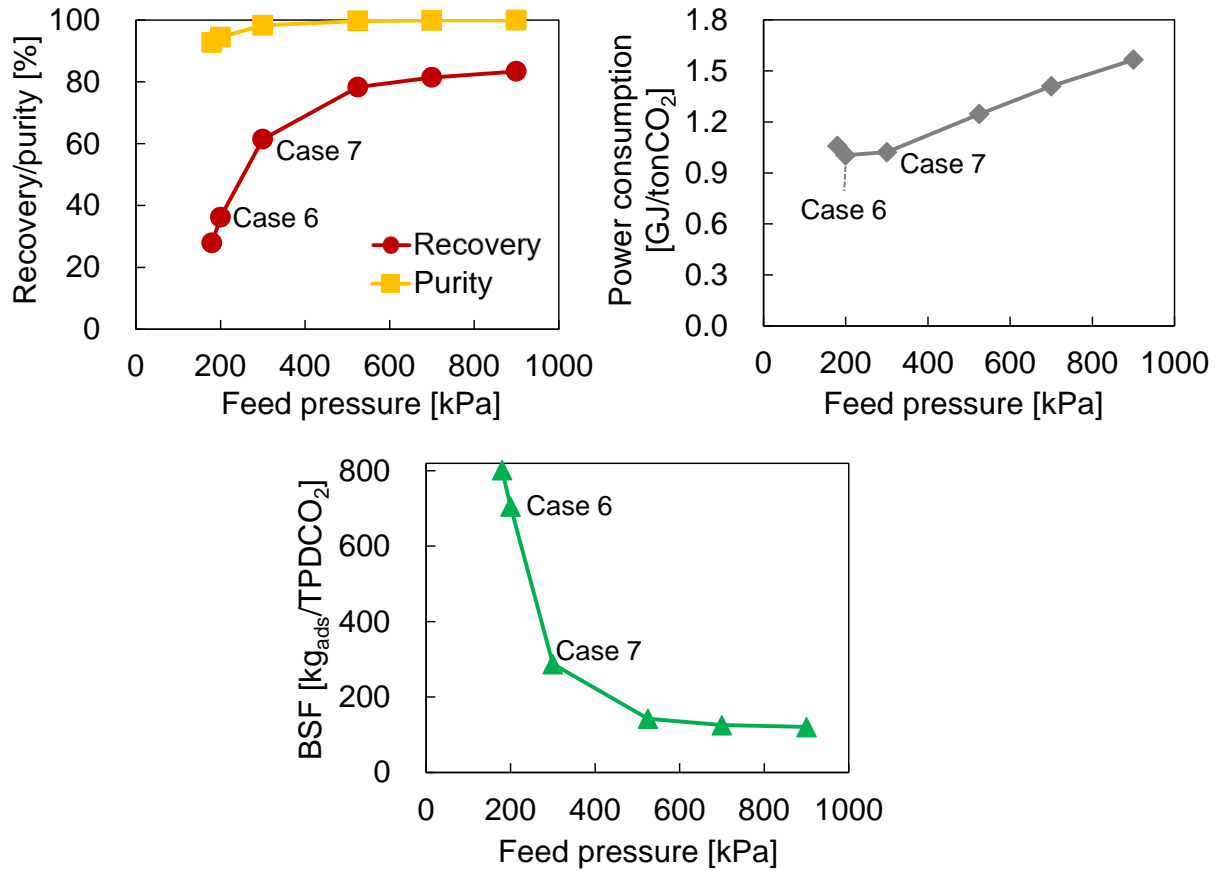


Figure 3-12. Performance indicators against feed pressure at temperature 273 K: (a) recovery rate and purity; (b) power consumption; (c) BSF.

Table 3-6 Results for different feed pressure at temperature 273 K

P_{feed} [kPa]	Recovery rate of CO ₂ [%]	Purity of product CO ₂ [%]	BSF [kg _{ads} /TPDCO ₂]	Power consumption [GJ _e /tonCO ₂]
180	27.9	92.6	802	1.06
200 (Case 6)	36.2	94.4	705	1.00
300 (Case 7)	61.4	98.3	287	1.02
525	78.3	99.6	142	1.25
700	81.4	99.9	125	1.41
900	83.4	99.9	121	1.57

3.6.5 Results for different desorption ratio r_d

The influence of desorption ratio r_d defined in Eq. (3-13) on the process performance indicators is shown in Figure 3-13 and Table 3-7. From Figure 3-13 (a) and (d), the optimal recovery rate is given at $r_d = 0.40$ for ELM-11 and at $r_d = 0.01$ for zeolite 13X. These optimal values of r_d also minimize the power consumption, as shown in Figure 3-13 (b) and (e). From Figure 3-13 (c) and (f), the BSFs are not the minimum at the optimal values of r_d , but remain nearly constant over the range I investigated: BSF varied from 118 to 128 $\text{kg}_{\text{ads}}/\text{TPDCO}_2$ (7.8% difference) for ELM-11, and from 541 to 677 $\text{kg}_{\text{ads}}/\text{TPDCO}_2$ (20% difference) for zeolite 13X. The convex trend of BSF against r_d can be explained by the influence of the desorption time and the recovery rate.

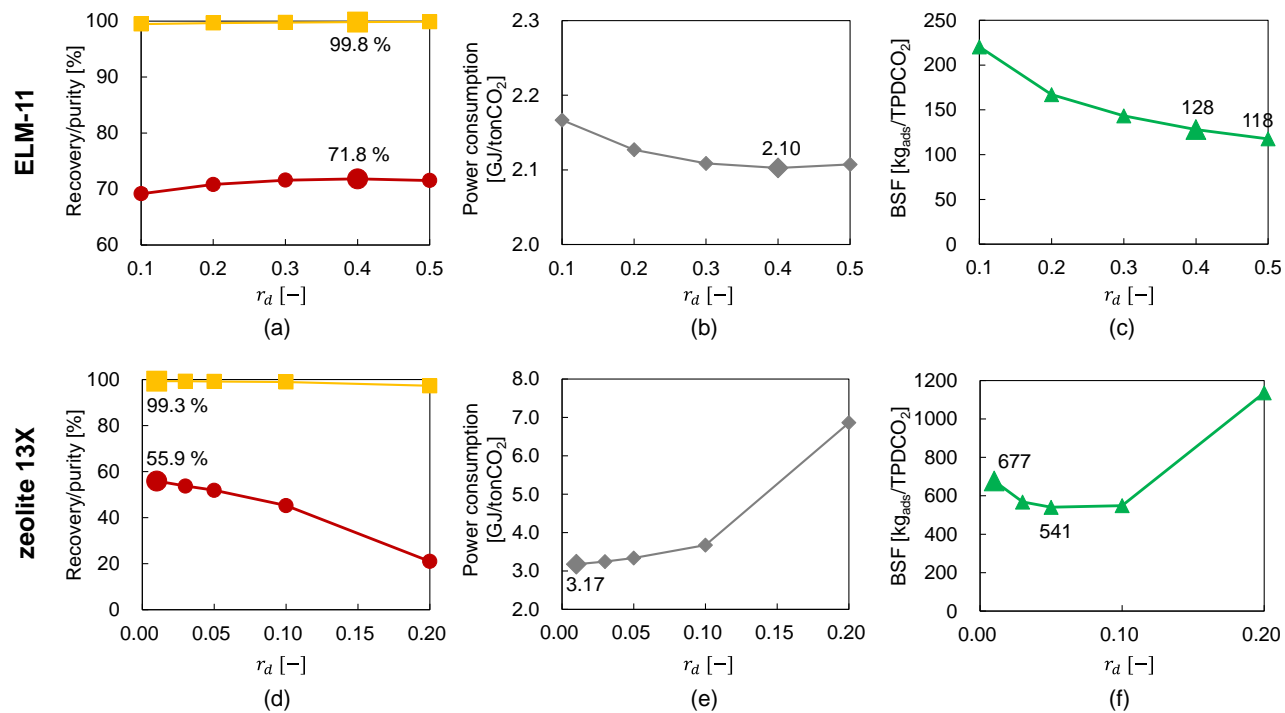


Figure 3-13. Results for different desorption ratio r_a : (a) recovery rate and purity for ELM-11; (b) power consumption for ELM-11; (c) BSF for ELM-11; (d) recovery rate and purity for zeolite 13X; (e) power consumption for zeolite 13X; (f) BSF for zeolite 13X.

Table 3-7 Results for different desorption ratios r_d . Optimal values of recovery rate of CO₂, BSF and power consumption are indicated by asterisks (*)

ELM-11					
Desorption ratio r_d [-]	Desorption time t_{des} [s]	Recovery rate of CO ₂ [%]	Purity of product CO ₂ [%]	BSF [kg _{ads} /TPDCO ₂]	Power consumption [GJ _e /tonCO ₂]
0.10	550	69.2	99.5	220	2.17
0.20	450	70.8	99.6	167	2.13
0.30	400	71.6	99.7	143	2.11
0.40	350	71.8*	99.8	128	2.10*
0.50	300	71.5	99.9	118*	2.11
zeolite 13X					
Desorption ratio r_d [-]	Desorption time t_{des} [s]	Recovery rate of CO ₂ [-]	Purity of product CO ₂ [-]	BSF [kg _{ads} /TPDCO ₂]	Power consumption [GJ _e /tonCO ₂]
0.01	1450	55.9*	99.3	677	3.17*
0.03	1050	53.8	99.3	568	3.24
0.05	850	51.9	99.2	541*	3.34
0.10	600	45.3	98.9	549	3.67
0.20	350	21.0	97.3	1136	6.86

3.6.6 Simulation results for 127 cases

Figure 3-14 shows all 127 simulation points conducted in this study and Table 3-8 shows the operating conditions and performance indicators for all cases with the optimal desorption ratios r_d maximizing the recovery rate. The United States Department of Energy (US-DOE) target recovery 90% can be achieved at low temperatures and high feed pressure. To achieve high recovery in an energy-efficient operation, a two-stage VPSA process, in which a column packed with a flexible MOF is connected to another column packed with a conventional MOF, has been proposed by Hiraide *et al.*⁷⁸

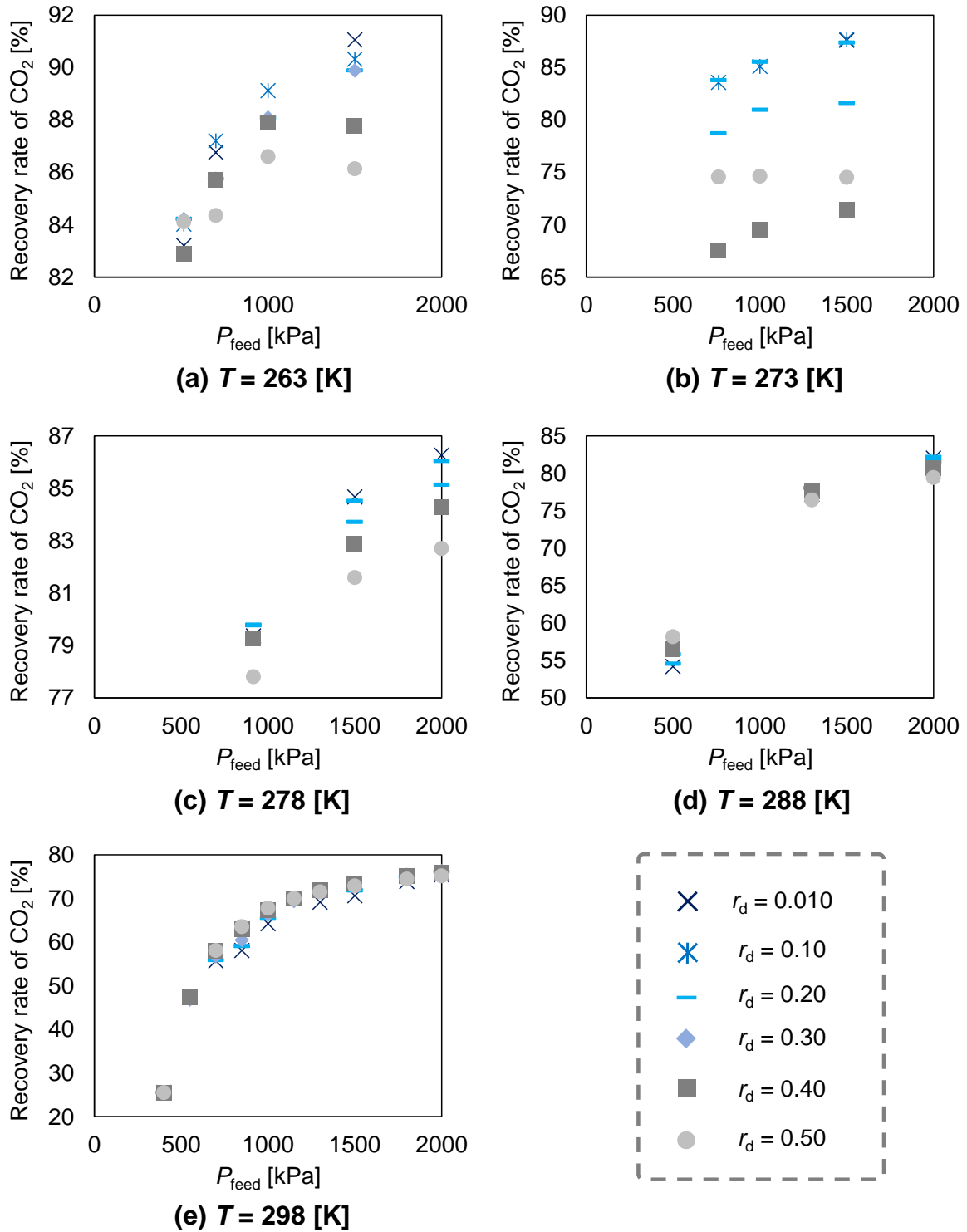


Figure 3-14. All 127 simulation points showing relationships among feed pressure, temperature, desorption ratio and recovery rate

Table 3-8 Operating conditions and performance indicators for all cases

Adsorbent	Operating conditions								Performance indicators			
	$T_{\text{feed}}, T_{\text{wall}}$ [K]	P_{feed} [kPa]	$p_{\text{foot,ads}}$ [kPa]	P_{des} [kPa]	η_{vacuum} [-]	t_{ads} [s]	t_{des} [s]	r_d [-]	Recovery rate of CO ₂ [%]	Purity of product CO ₂ [%]	BSF [kg _{ads} /TPDCO ₂]	Power consumption (compressor, vacuum pump) [GJ _e /tonCO ₂]
ELM-11	263	516	20.1	8.14	0.298	340	750	0.2	84.5	99.7	147	1.33 (0.809, 0.525)
ELM-11	263	700	20.1	8.14	0.298	390	850	0.1	87.2	99.8	138	1.50 (0.975, 0.527)
ELM-11	263	1000	20.1	8.14	0.298	370	750	0.2	88.8	99.9	128	1.72 (1.20, 0.518)
ELM-11	263	1500	20.1	8.14	0.298	450	1000	0.01	91.1	99.9	128	1.99 (1.47, 0.521)
ELM-11	273	762	29.6	11.8	0.371	370	500	0.2	83.8	99.9	110	1.50 (1.11, 0.385)
ELM-11	273	1000	29.6	11.8	0.371	380	500	0.2	85.6	99.9	105	1.67 (1.29, 0.383)
ELM-11	273	1500	29.6	11.8	0.371	430	800	0.1	87.7	99.9	121	1.92 (1.58, 0.337)
ELM-11	278	916	35.4	14	0.407	330	900	0.3	79.8	99.8	179	1.57 (1.34, 0.230)
ELM-11	278	1500	35.4	14	0.407	410	1250	0.1	84.7	99.9	174	1.90 (1.67, 0.232)
ELM-11	278	2000	35.4	14	0.407	420	1250	0.1	86.3	99.9	166	2.12 (1.89, 0.230)
ELM-11	288	500	49.6	19.5	0.472	160	400	0.5	58.2	98.7	272	1.39 (1.24, 0.152)
ELM-11	288	1300	49.6	19.5	0.472	340	600	0.3	78.1	99.8	138	1.89 (1.73, 0.164)
ELM-11	288	2000	49.6	19.5	0.472	400	700	0.2	82.2	99.9	126	2.22 (2.06, 0.165)
ELM-11 (Case 3)	298	400	67	26.4	0.52	60	300	0.5	25.5	92.0	1333	2.55 (2.44, 0.113)
ELM-11	298	550	67	26.4	0.52	130	300	0.4	47.4	97.4	467	1.83 (1.70, 0.129)
ELM-11	298	700	67	26.4	0.52	130	300	0.4	58.1	98.8	272	1.79 (1.65, 0.128)
ELM-11	298	850	67	26.4	0.52	190	300	0.4	64.4	94.4	181	1.84 (1.69, 0.146)

ELM-11 (Case 4)	298	1000	67	26.4	0.52	240	300	0.5	67.8	99.7	145	1.92 (1.77, 0.150)
ELM-11	298	1150	67	26.4	0.52	280	300	0.5	70.0	99.8	126	2.02 (1.87, 0.152)
ELM-11 (Case 1)	298	1300	67	26.4	0.52	290	350	0.4	71.8	99.8	128	2.10 (1.95, 0.144)
ELM-11	298	1500	67	26.4	0.52	320	350	0.4	73.5	1.0	117	2.21 (2.06, 0.157)
ELM-11	298	1800	67	26.4	0.52	340	400	0.3	75.4	99.9	115	2.36 (2.20, 0.160)
ELM-11	298	2000	67	26.4	0.52	350	400	0.3	76.3	99.9	111	2.45 (2.29, 0.160)
ELM-11 (Case 2)	298	1300	67	26.4	0.52	250	350	0.4	73.7	99.7	137	2.05 (1.90, 0.157)
zeolite 13X (Case 5)	298	250	-	3.3	0.16	230	1450	0.01	55.9	99.3	677	3.17 (0.656, 2.51)

3.7 Concluding remarks

In this chapter, a 4-step VPSA process using ELM-11 was evaluated by simulation with PDAEs. The process is simple without a rinse or purge steps since ELM-11 desorbs almost 100% of CO₂ in the desorption step. The process evaluation indicators considered in this chapter were CO₂ recovery, purity, BSF, and power consumption. Important operating conditions (adsorption time, desorption time, desorption pressure, and vacuum pump efficiency) were systematically determined to find appropriate values. Also, I solved the numerical issues in solving the PDAEs by using the artificial buffer step and the continuation. These methods can be applied to other numerically challenging process simulations in other studies.

From the results of the process simulation presented in Section 3.6, the following insights were obtained. Section 3.6.1 shows the results at the ambient temperature of 298 K. It is mentioned that the CO₂ recovery rate highly depends on feed pressure. Also, the recovery estimation equation (Eq.(3-18)) is proposed based on the slipping-off mechanism. Section 3.6.2 presents the results at various temperatures ranging from 263 K to 298 K. It is shown that the lower the temperature, the lower the feed CO₂ pressure and the higher the CO₂ recovery. It was also found that at lower temperatures, the compressor power can be saved because of the easier adsorption at lower feed pressure, but the vacuum pump power is higher because of the lower pressure required for desorption. Section 3.6.3 compares ELM-11 with zeolite 13X, a conventional adsorbent. Due to the shape of isotherms, desorption rate of ELM-11 was much higher than that of zeolite 13X. Also, the power consumption and CO₂ recovery

rate were found to be more efficient for ELM-11. Section 3.6.4 provides a detailed analysis at the low temperature of 273 K. Section 3.6.5 examines the effect of the parameter r_d on the process performance. Section 3.6.6 analyzes the process performance in 127 cases. Among the cases, the maximum CO₂ recovery was 91.1%, meeting the criteria set by the US-DOE. The above multi-angle analysis clarified the advantages of ELM-11 and the operating conditions to improve the process performance.

Chapter 4 Advanced critical path method with stochastic durations

4.1 Preparation

4.1.1 Project management and critical path

Network-based methods have been applied to many project management problems. A project is a set of activities with objectives and completion deadlines. Various projects such as production,¹⁴¹ construction,^{142,143} system development¹⁴⁴ can be modeled as networks, which can be handled by advanced management techniques. In many cases, completing projects in deadlines is the most critical requirement. For example, meeting the delivery date of a product, which is set as a deadline, is a critical constraint for many manufacturing systems. To satisfy such an important constraint, effective management of the systems is crucial.

The *Critical path method* (CPM) and the *Project evaluation and review technique* (PERT) are widely used as network-based methods for project management, which were proposed for the first time in 1950s.^{111,145} The project network is expressed with an *arrow diagram* as shown in Figure 4-1, where i is a task. In this figure, an activity is expressed as a node and a sequence of activities is expressed as an arc. Note that there are two equivalent expressions of the arrow diagram. In the activity on node type, activities with given durations are expressed as nodes. On the other hand, in the activity on arc type, they are expressed as arcs.¹⁴⁶ These two types of expressions are equivalent, and I employ the former type consistently in this thesis.

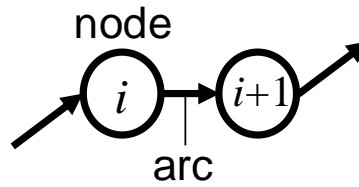


Figure 4-1. Arrow diagram

Here I show an example of a CCUS system in Figure 4-2. The CCUS system has six tasks; Task 1 is renewable energy generation from photovoltaic or wind power generation; Task 2 is water electrolysis using the energy generated by Task 1; Task 3 is power generation by a power plant; Task 4 is a CO₂ capture process from the flue gas of the power plant; Task 5 is a process to synthesize methane from H₂ produced in Task 2 and CO₂ recovered in Task 4; Task 6 is transportation of methane synthesized in Task 5 using pipelines or tank trucks; and finally, Task *s* is a source node which is the starting stage of the process, and Task *e* is a sink node which is the completion of the process. In this study, any system has a single source *s* and a single sink *e*. These source and sink are treated as dummy tasks that have no duration. It should be noted that many different expressions can be made by adding dummy nodes that are all equivalent. Note that the network diagram in Figure 4-2 is not handled as a case study in this thesis.

In a project network, the tasks must be completed sequentially. Firstly, in sequential tasks $i \rightarrow (i + 1)$, the task $(i + 1)$ cannot begin before the other task i finishes. In the example in Figure 4-3, Task 2, Task 4, and Task 6 cannot begin before Task 1, Task 3, and Task 5 finish, respectively. Secondly, if a task has a junction where several tasks are connected, the task cannot begin before all jointed tasks finish; an example is Task 5 in Figure 4-3.

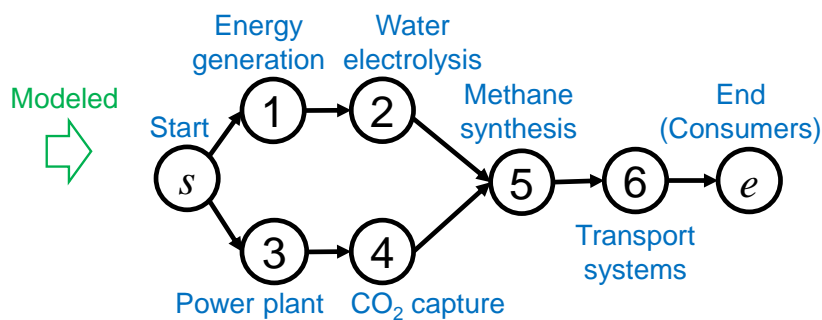
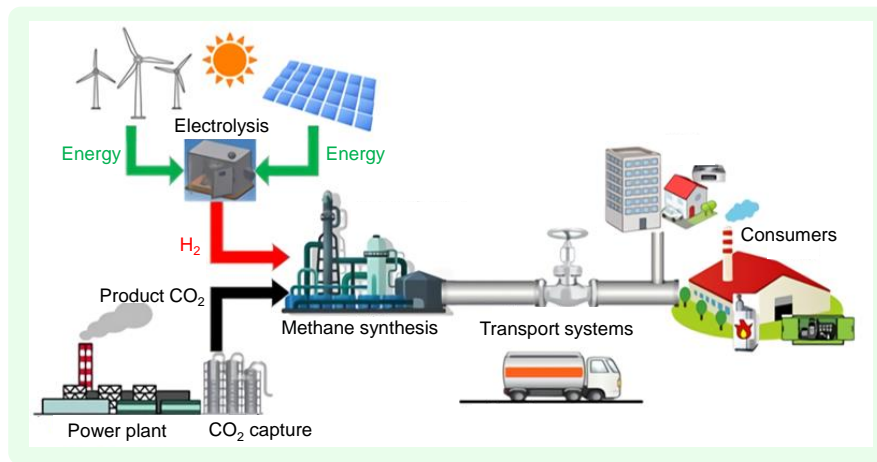


Figure 4-2. Example of a simple CCUS system

The completion time of the process, *process completion time*, is determined by the *critical path*. Here, a *path* is a sequence of tasks from the source to sink. Figure 4-3 shows the durations for each task, and paths for the system shown in Figure 4-2. The system has two paths; one is $s \rightarrow \text{Task 1} \rightarrow \text{Task 2} \rightarrow \text{Task 5} \rightarrow \text{Task 6} \rightarrow e$ (Path 1); the other is $s \rightarrow \text{Task 3} \rightarrow \text{Task 4} \rightarrow \text{Task 5} \rightarrow \text{Task 6} \rightarrow e$ (Path 2). The path that has the longest duration is called the *critical path*. Here I assume that each task duration is given as $t_1 = 60; t_2 = 40; t_3 = 40; t_4 = 40, t_5 = 50; t_6 = 60$, where t_i is given duration of task i . In this case, the critical path is Path 1 since the sum of task durations on Path 1, $t_1 + t_2 + t_5 + t_6 = 210$, is larger than that of Path 2, $t_2 + t_3 + t_5 + t_6 = 190$. Therefore, the process completion time is also 210, which is the duration of the critical path, and the duration of Task 3 and Task 4 do not influence the process completion time. Thus, the process completion time can be shortened by reducing the task durations on the critical path (Path 1).

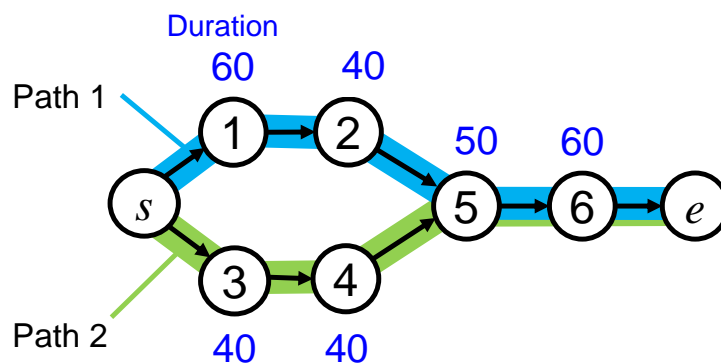


Figure 4-3. Task durations and paths

The PERT/CPM methods have been powerful techniques also for many chemical engineering problems.^{147,148} For example, in batch chemical processes where multiple tasks can be expressed as a project network, finding the capital investment strategy to optimize the scheduling can be formulated as a CPM problem. Furthermore, the PERT method can be applied to scheduling problems such as estimating uncertain completion times in chemical processes. These problems that can be handled by the PERT and CPM methods exist in many process industries such as steel, pharmaceuticals, semiconductor, and food. In addition, the PERT and CPM methods have been applied to construction of chemical plants as previously reported.¹⁴⁹

4.1.2 Handling uncertainty in critical path method

In the classical PERT/CPM methods, task durations are handled as fixed values. However, actual task durations in many real applications have uncertainty influenced by unpredictable reasons such as weather, human resources, equipment failure, traffic conditions, etc. To represent realistic project

management scenarios, handling uncertainty is often crucial, and various modifications have been proposed for the classical PERT/CPM methods. Here I classify approaches for modeling uncertainty in task or path durations into the following four classes: fixed time (Figure 4-4 (a)), fuzzy numbers (Figure 4-4 (b)), probability distribution (Figure 4-4 (c)), and histogram (Figure 4-4 (d)).

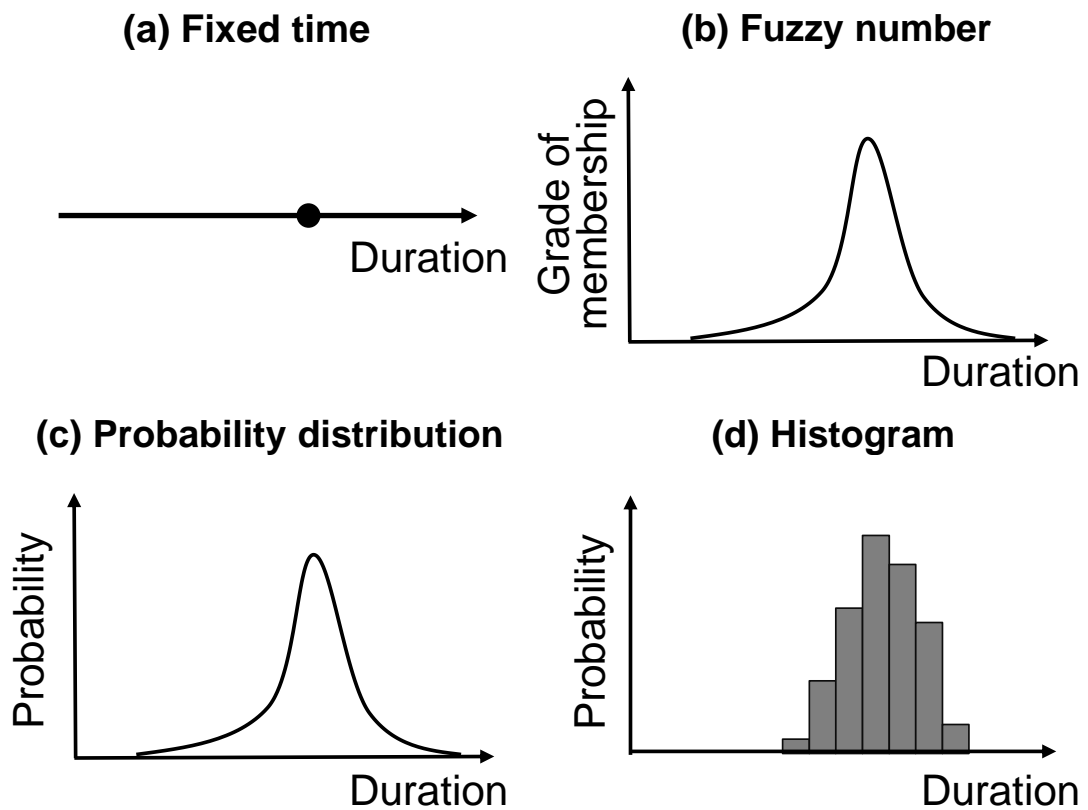


Figure 4-4. Four classes of modeling uncertainty in duration

The first approach is to regard task durations using a few representative values (point estimate) shown in Figure 4-4 (a). A common approach in this class is the *three-point estimation method*, where the distributions of the task durations are approximated by the following three values—the most likely

value, most optimistic value, and most pessimistic value. The classical PERT method employs this method.¹⁴⁵ However, it has been reported that approximations based on this approach may deviate from the true distributions.¹⁵⁰

The second approach is to regard task durations as fuzzy numbers (Figure 4-4 (b)), which is proposed by Zadeh for the first time.¹⁵¹ Fuzzy number expresses uncertainty by using the *membership function* which shows degree of confidence that the duration is. The scheduling methods that use fuzzy numbers have been proposed by Sadjadi et al.,¹⁵² Kaur and Kumar,¹⁵³ Xu et al.,¹⁵⁴ Chen and Hsueh.¹⁵⁵

The third approach is to assume the task durations follow some known continuous distribution functions (Figure 4-4 (c)). In the method that Golenko-Ginzburg and Gonik proposed, task durations are assumed to follow normal or beta distributions.¹⁵⁶ Dodin proposed a way to determine the probability distribution functions of the longest path in stochastic networks.¹⁵⁷ Hajdu and Bokor analyzed how types of probability distribution, like beta distribution or triangle distribution etc., of tasks affect the probability distribution of the entire project network.¹⁵⁰

The fourth approach is to handle task or path durations as histograms (Figure 4-4 (d)). The methods that handle task or path durations as discrete values have been proposed by Herroelen and Leus,¹⁵⁸ and Bruni et al.¹⁵⁹ Since the actual data of task or path durations is given as discrete values, handling the data histograms without approximation can be an advantage. My model employs this approach for the CCUS systems, where histograms of task durations can be obtained from historical operation data.

4.1.3 Considering time-cost trade off

An important difference between the CPM and the PERT is to consider time-cost trade off or not. In the CPM, task or path durations can be improved (shortened) by allocating *cost* to the tasks or paths, where the costs are limited resources such as human resources or utilities. Figure 4-5 shows an example of improvement of probability distribution of duration. By allocating cost, the expected value and dispersion of the distribution in Figure 4-5 become smaller. The CPM methods find the most effective way to allocate limited costs to the process. On the other hand, the PERT does not consider the time-cost trade-off and analyzes the whole duration or total cost of the process. In the following discussion, various methods that consider time-cost trade off or not are discussed in further detail.

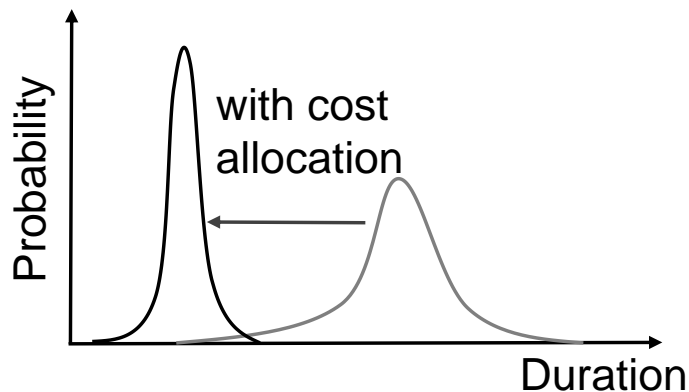


Figure 4-5. Improvement of duration

Various formulations considering time-cost trade-off have been proposed for the objective function. Kelley and Walker set the objective function as minimizing the project completion time or total allocation cost.¹¹¹ Xu et al. proposed four optimization problems with different objective functions such as minimizing total allocating cost.¹⁵⁴ On the other hand, Hasuike aimed to maximize an

approximation for the project completion probability within a target completion time.¹⁶⁰ In my model, a similar objective function is employed as Hasuike's method, where the probability is maximized, while I evaluate the objective function without approximation.

In time-cost trade off problem, there are two approaches to model improvement of task or path durations by allocating costs to tasks or paths. The first approach is continuous improvement per allocating costs, which assumes task or path durations decrease continuously in proportion to allocated costs. In this approach, the relationship between the allocated cost and reduction of task (or path) durations must be modeled as a continuous function to formulate an optimization problem.^{111,154,160} The other approach employs discrete improvement per allocating costs, which assumes task or path durations have discrete candidates by allocating some cost. In this approach, the relationship between the allocated cost and reduction of task (or path) durations must be modeled as a discrete function to formulate an optimization problem.¹⁶¹

Various scheduling methods that do not consider time-cost trade-off have been proposed. These methods generally have a single objective to estimate some indicators of the target project. The classical PERT method aims to estimate the project completion time.¹⁴⁵ Bruni et al. proposed a way to estimate minimum makespan that probability or "reliability level" of project completion is larger than a constant.¹⁵⁹ Ke and Liu proposed three ways to estimate, such as minimum cost expectation value or probability that the cost exceeds the budget.¹⁶² In addition, Hajdu and Bokor proposed a way to

estimate how the shape of the distribution function of each task duration affects the project completion time.¹⁵⁰

4.1.4 Solution approaches

I also classify the project scheduling methods with uncertainty based on the solution approaches. These problems can be solved either by a heuristic or deterministic algorithm. Due to the difficulty of the CPM problems with uncertainty, many heuristic approaches have been proposed. Heuristic algorithms are often used for finding approximate solutions when a short computational time is desired, or the problems is difficult to be formulated as a deterministic problem. Such approaches include the Monte Carlo simulation,¹⁶³ genetic algorithm,¹⁶⁴ and combining these two numerical techniques.^{162,165} On the other hand, in deterministic approaches, the exact solution can be found without an approximation. Examples include Linear Programming (LP) by Kelley and Walker,¹¹¹ LP using fuzzy parameters by Kaur and Kumar,¹⁵³ and Mixed-Integer Linear Programming (MILP) by Bruni et al.¹⁵⁹

4.1.5 Advantages of proposed method

In this thesis, I propose a method based on deterministic optimization in which the task durations are handled as histograms considering the time-cost trade off. The proposed approach has the following three advantages. Firstly, the operation data can be handled without approximation and losing information by handling task durations as histograms. Secondly, I consider time-cost trade off and find

the optimal cost allocation that maximizes the project completion probability within a given completion time. Note that I consider two kinds of improvement of task durations to enable more flexible modeling, while past studies consider only a single way to improve task durations.^{111,154,160} Thirdly, by formulating the problem as a MILP problem that a deterministic algorithm can solve, the exact solution can be found without an approximation in contrast to the heuristic approaches where only an approximate solution can be found.

The following discussions in Section 4 are organized as follows. In Section 4.2, I discuss the classical CPM problem and how to handle uncertainty as a background. In Section 4.3, I describe our assumptions in our problem formulation. In Section 4.4, I propose a new approach called Task-Oriented Formulation. In Section 4.5, I reformulate the same problem to decrease the computational time. In Section 4.6, I propose an iterative local search method to shorten the computational time. In Section 4.7, I show examples.

4.2 Problem descriptions

4.2.1 CPM without uncertainty

The CPM is a method to find the critical path in a process. This approach can also identify the most efficient improvement to reduce the process completion time. In this thesis, task durations are assumed to be shortened by allocating *cost* to the tasks, where the costs are limited resources such as human resources or utilities. The duration t_i of task i is assumed to be shortened (improved) linearly, where proportionality constant λ_i of a duration of task i , per additional cost c_i for all tasks $i \in W$. Note that $W = \{1, 2, \dots, n\}$ is the set of tasks except for source and sink, and n is the number of tasks except for source and sink. The duration of task i after cost allocation is $t_i - \lambda_i c_i$, $i \in W$. Since the process completion time is equal to the longest path duration,

$$\text{(Process completion time)} = \max_{j \in V} \left\{ \sum_{i \in p_j} t_i - \sum_{i \in p_j} \lambda_i c_i \right\}. \quad (4-1)$$

where j is a path from source to sink; r is the number of paths from source to sink; $V = \{1, 2, \dots, r\}$ is the set of all paths from source to sink. The CPM problems without uncertainty, which aim to minimize the process completion time, are generally formulated as min-max problem which assumes that task durations are reduced linearly with additional cost.

$$\begin{aligned} & \text{Minimize : } \max_{j \in V} \left\{ \sum_{i \in p_j} t_i - \sum_{i \in p_j} \lambda_i c_i \right\} \\ & \text{s.t. } \sum_{i \in W} c_i \leq C \\ & \quad 0 \leq c_i \leq c_i^U, \quad i \in W \end{aligned} \quad (4-2)$$

where p_j is the set of tasks except for dummy tasks on path $j \in V$; c_i^U is the crash cost (maximum cost) of task i ; C is the maximum total cost. These sets W , V , p_j and parameters t_i , λ_i , c_i^U , $i \in W$ above are assumed to be known. On the other hand, c_i , which is allocated cost of task $i \in W$, is a decision variable.

Generally, this problem can be formulated as Linear Programming (LP).¹¹¹

The classical CPM problem without uncertainty assumes that the task durations are known and constant. However, many task durations in the CCUS systems are subject to uncertainty. For example, power generation using renewable energy is affected by weather conditions; transportation by tanker truck is affected by traffic conditions; and steel and chemical processes, which are sources of CO₂ emissions, have different task durations depending on the product species. To consider the uncertainties in task durations, the classical CPM typically uses the average or mean of task duration or three-point estimation values to represent the distribution of the task duration based on best-case, most likely, and worst-case estimates. However, these approaches cannot fully utilize the information of the task duration distributions.

4.2.2 CPM with uncertainty

In this study, I expand the concept of the CPM without uncertainty, and define “*CPM with uncertainty*” as follows: I formulate a problem to maximize the probability of finishing all tasks by a given target completion time Γ . Here, I define a vector of allocating some cost to task i as \mathbf{c}_i , assuming the maximum total cost is given as C . Additionally, the duration of task i has a probability distribution illustrated in Figure 4-6, which can be improved by allocating some cost.

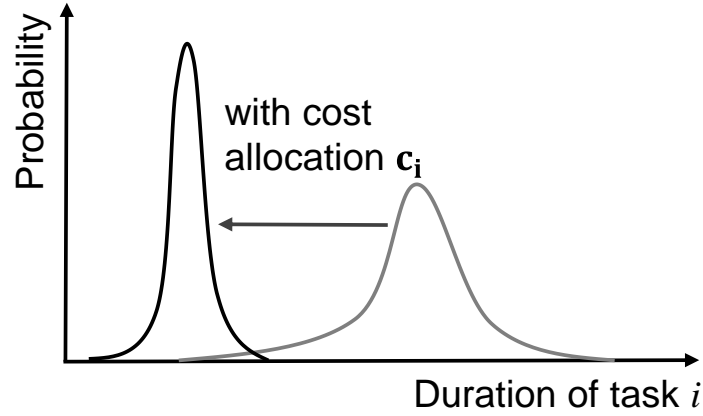


Figure 4-6. Probability distribution of duration of task i

Under these assumptions, the problem is generally formulated as

$$\text{Maximize : Pr}[\text{Process completion time} \leq \Gamma] \quad (4-3)$$

$$\text{s.t. } \sum_{i \in W} \|\mathbf{c}_i\| \leq C, \quad (4-4)$$

$$\mathbf{0} \leq \mathbf{c}_i \leq \mathbf{c}_i^U, \quad i \in W \quad (4-5)$$

where $\|\mathbf{c}_i\|$ is L1 norm of the vector of allocating cost \mathbf{c}_i , \mathbf{c}_i^U is a vector of the crash cost (maximum cost) of task i . In this formulation, the objective function (4-3) is the probability of finishing all tasks by a target completion time Γ ; generally, calculating the objective function (4-3) requires multi-dimensional integrations and convolutions, which are complicated operations that require the information of all paths.¹⁶⁶ Furthermore, to handle the task durations in the continuous time domain, it is necessary to model the probability distributions as some functional forms, which may require approximation. In this study, I avoid these two problems by discretizing the time domain, and

converting this problem into a Mixed-Integer Linear Programming (MILP) problem, as described in the next section.

4.3 Assumption for proposed methods

4.3.1 Obtaining discrete probability from operation data

In this thesis, the operation data is handled as discrete probability distributions, which avoids approximating the probability distribution to functional forms. Bruni used discrete data for the same motivation.¹⁵⁹ In our work, historical operation data is assumed to be available. Such data is an accumulated record of task durations, which can be shown graphically as histograms. This assumption does not require any approximation to probability distribution functions; thus, the solution is expected to be more accurate. I also assume that the duration of each task is independent (i.e. the duration of task i does not influence that of another task i' , $i \neq i'$).

To generate discretized distribution from the operation data, I discretize the duration of task i using an index k_i . Using this index, histograms of task distributions are discretized as illustrated in Figure 4-7. Here, k_i is an integer which takes a value between 0 and m , and I define a set of all realizations of k_i as A .

$$A = \{0, 1, 2, \dots, m-1, m\}. \quad (4-6)$$

The duration of task i without cost allocation, which is given as $t_i^{(k_i)}$, is uncertain and treated as a random variable and the scenario (realization) is specified by the integer k_i . As a result of the discretization, $t_i^{(k_i)}$ has multiple scenarios; $t_i^{(0)}, t_i^{(1)}, \dots, t_i^{(m-1)}, t_i^{(m)}$ (see Figure 4-7). Note that one realization of the discrete random variables from Task 1 to n as $\left(t_1^{(k_1)}, t_2^{(k_2)}, \dots, t_n^{(k_n)}\right)$ corresponds to

a scenario that duration of task i is within $t_i^{(k_i-1)} < t_i \leq t_i^{(k_i)}$ for all tasks $i \in W$, where t_i is duration of task i (expression as a continuous variable), $t_i^{(k_i')}$ is a certain realization of the $t_i^{(k_i)}$. Note that the number of all scenarios is m^n , which is a large number.

It should also be noted that the normalized distribution obtained from such data approaches the probability distribution as the historical record becomes larger with repeated operations. Figure 4-7 is an illustration of the normalized distributions. I divide duration of task i into m bins, which gives parameters of the probability $\alpha_i^{(k_i')}$ that satisfies $t_i^{(k_i)} = t_i^{(k_i')}$:

$$\begin{aligned} \alpha_i^{(k_i')} &= \Pr[t_i^{(k_i)} = t_i^{(k_i')}] \\ &= \frac{N_i[t_i^{(k_i')}]}{\sum_{k_i \in A} N_i[t_i^{(k_i)}]}, \end{aligned} \quad (4-7)$$

where $N_i[t_i^{(k_i)}]$ is defined as the number of samples within $t_i^{(k_i-1)} < t_i \leq t_i^{(k_i)}$, which is obtained from the historical operation data.

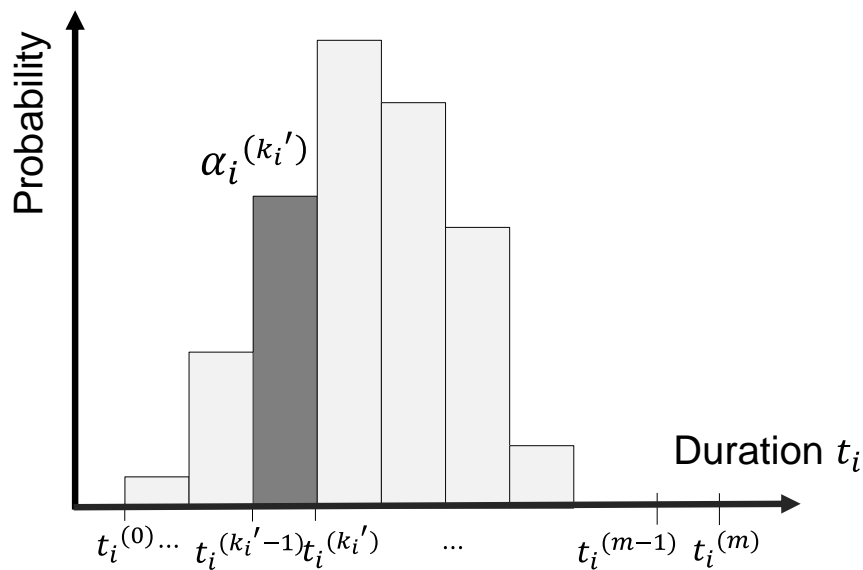


Figure 4-7. Normalized histogram of duration of task i

4.3.2 Approaches to improve task durations

Improvement (or shortening) task durations can be performed in a number of different ways, and outcomes can be difficult to predict. Some examples of such improvement are increasing the number of operators; preparing a training manual for operators. In CO₂ adsorption processes, task durations can be reduced by using adsorbents with fast mass transfer, as shown in Section 3.6.3. Some examples in chemical industries include upgrading the catalyst in a reactor and increasing the pump capacity in a liquid transport unit. As a result of such improvement measures, the task durations can be shortened, and the profile of the probability distributions (or histograms of the task duration data) may change significantly. It would not be easy to model and predict the change in probability distributions.

In this study, I use simple approaches to model the improvement of task durations by using two parameters, the expected value (mean) and dispersion (variance) of the probability distributions. The first approach is to decrease the expected value of task durations linearly per additional cost while keeping the shape of the distribution, as shown in Figure 4-8 (a). This approach shifts the entire distribution horizontally:

$$\tilde{t}_i^{(k_i)} = t_i^{(k_i)} - \lambda_{M,i} c_{M,i} \quad (4-8)$$

where $\tilde{t}_i^{(k_i)}$ is improved duration of task i by cost allocation; $c_{M,i}$ is allocating cost to reduce expected value of task duration; $\lambda_{M,i}$ is the decrease rate of $\tilde{t}_i^{(k_i)}$ per additional cost, which is assumed to be constant. I call this approach as *improvement of expected value*.

The second approach to improve the task duration is to narrow the dispersion while keeping the expected value of the distribution constant (Figure 4-6 (b)). In this approach, the task duration $\tilde{t}_i^{(k_i)}$ of task i after improvement is written as

$$\tilde{t}_i^{(k_i)} = t_i^{(k_i)} - \left(t_i^{(k_i)} - t_i^{\text{ave}} \right) \lambda_{D,i} c_{D,i} \quad (4-9)$$

where $c_{D,i}$ is allocating cost to reduce dispersion of task duration; and $\lambda_{D,i}$ is the proportionality constant

of dispersion per additional cost; t_i^{ave} is average duration of task i without improvement, where I define as:

$$t_i^{ave} = \frac{\sum_{k_i \in A} t_i^{(k_i)} N_i^{(k_i)}}{\sum_{k_i \in A} N_i^{(k_i)}}, i \in W. \quad (4-10)$$

I call this approach as *improvement of dispersion*.

While the *improvement of expected value* is used commonly by Kelley and Walker,¹¹¹ and Xu et al,¹⁵⁴ the *improvement of dispersion* is unique and other papers have not considered this approach. My proposed framework can handle both approaches. I demonstrate the benefit of the dispersion improvement in a case study in Section 4.7.

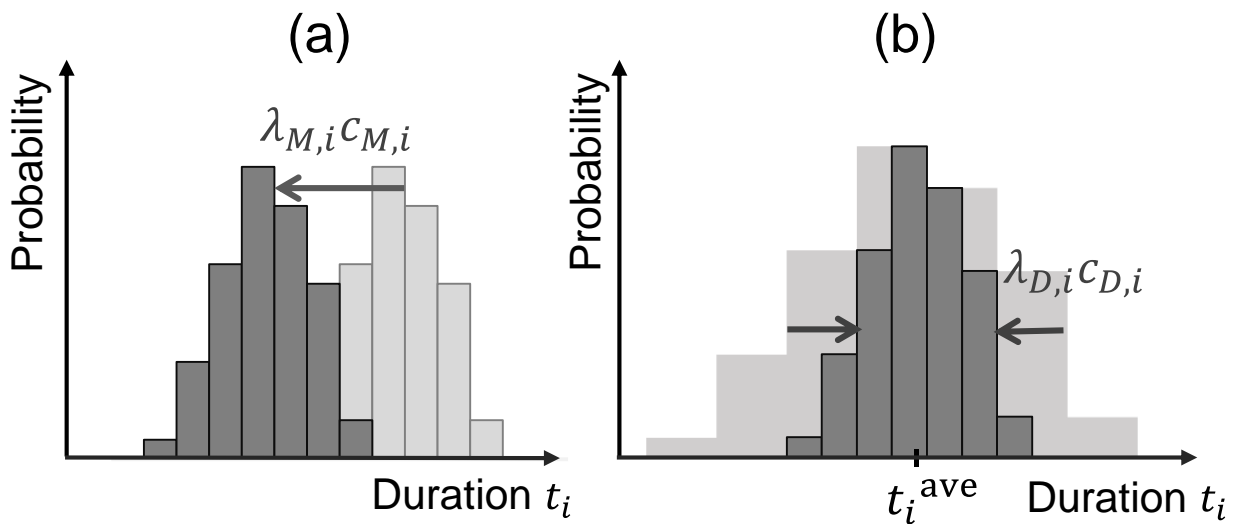


Figure 4-8. Improvement of duration of task i

4.4 Task-Oriented Formulation

In this section, I propose a reformulation strategy for the problem given by the *CPM without uncertainty* (4-3)-(4-5) into a MILP problem. This formulation is referred to as the Task-Oriented Formulation, while I discuss another reformulation called as Path-Oriented Formulation in Section 4.5.

4.4.1 Preparation for Task-Oriented Formulation

To avoid the complex operation in evaluating the objective function with convolution introduced by Kamburowski,¹⁶⁶ I convert the objective function (4-3) into a simple linear equation. From (4-7) I

express the joint probability that all tasks finish within the shaded bins in Figure 4-9 as the

multiplication of probabilities $\alpha_i^{(k_i')}$ for all tasks $i \in W$:

$$\Pr \left[t_i^{(k_i)} = t_i^{(k_i')}, i \in W \right] = \alpha_1^{(k_1')} \alpha_2^{(k_2')} \dots \alpha_n^{(k_n')} . \quad (4-11)$$

i.e. Eq.(4-11) is the probability that each task i finishes in $t_i^{(k_i)} = t_i^{(k_i')}$ for $i \in W$. Here, it should be noted that there are a large number of combinations for the realizations of indices k_i in the random variables $t_i^{(k_i)}$,

$$(k_1, k_2, \dots, k_n) \in A^n . \quad (4-12)$$

In this work, I assign binary variables $x^{(k_1, k_2, \dots, k_n)} \in \{0, 1\}$ that enumerate all possible realizations of the random variables. I consider a logic condition such that each of these random variables becomes positive only if the process completion time is equal to or shorter than T :

$$x^{(k_1, k_2, \dots, k_n)} = \begin{cases} 1 & \text{if Project completion time} \leq \Gamma \\ 0 & \text{otherwise} \end{cases} . \quad (4-13)$$

Using Eq. (4-11) and (4-13), I rewrite Eq. (4-3) in a discretized form as follows:

$$\begin{aligned}
& \Pr[\text{Project completion time} \leq \Gamma] \\
&= \sum_{(k_1', k_2', \dots, k_n') \in A^n} \Pr \left[t_i^{(k_i)} = t_i^{(k_i')}, i \in W \right] x^{(k_1', k_2', \dots, k_n')} \\
&= \sum_{(k_1', k_2', \dots, k_n') \in A^n} \alpha_1^{(k_1')} \alpha_2^{(k_2')} \dots \alpha_n^{(k_n')} x^{(k_1', k_2', \dots, k_n')}.
\end{aligned} \tag{4-14}$$

Here, instead of using the complex operations in calculating the Eq. (4-3) in the continuous time domain, I discretize the time domain and rely on the logic condition in Eq. (4-13). I implement this logic constraint within a framework of integer programming as shown below.

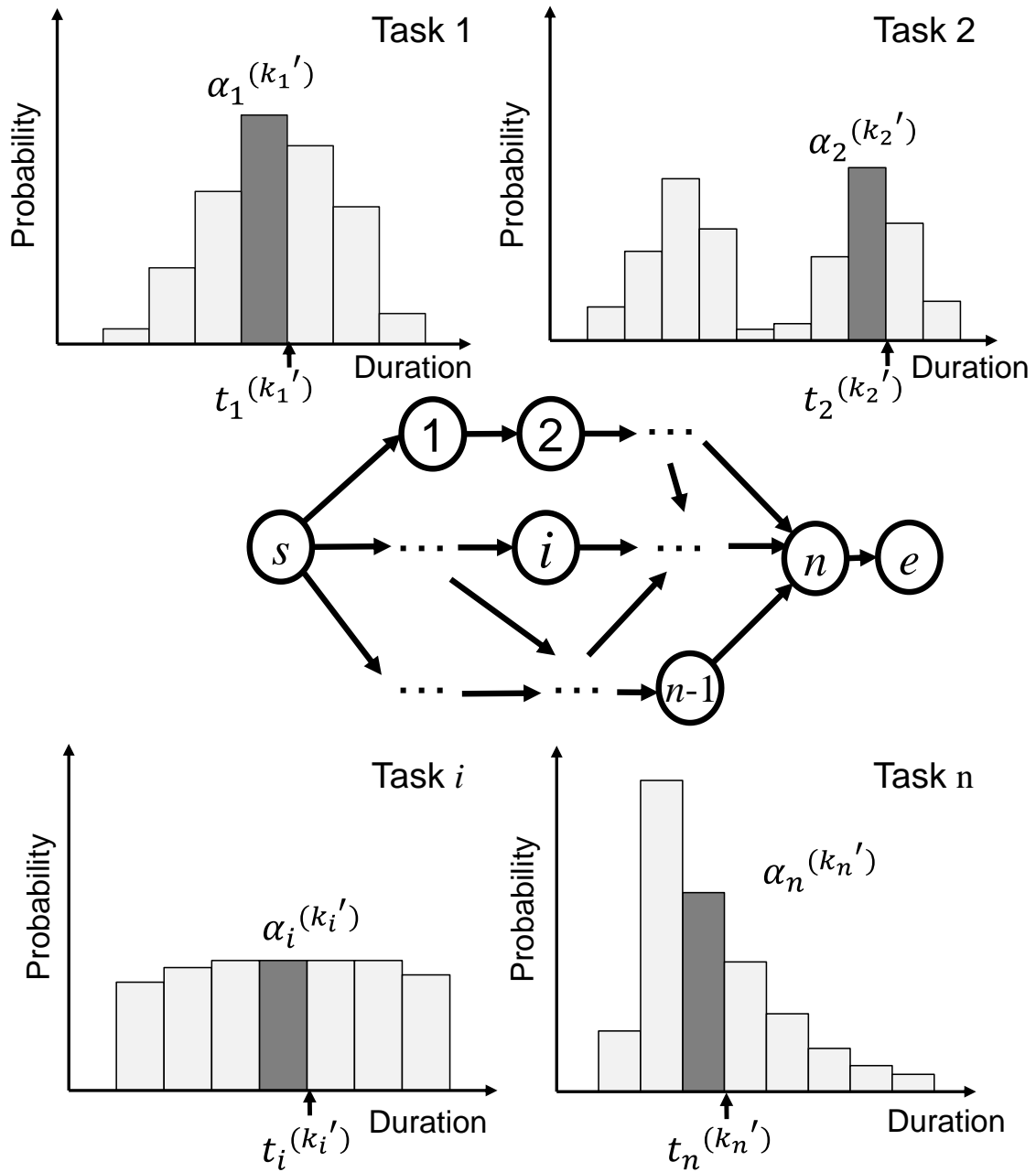


Figure 4-9. Concept of Eq. (4-11)

4.4.2 Task-Oriented Formulation

The optimization problem given in Eq. (4-3) - (4-5) can be reformulated into the following form using Eq. (4-13) and (4-14). Firstly, I show overall formulation and then discuss each constraint.

Task-Oriented Formulation (TOF)

$$\text{Maximize: } \sum_{(k_1, k_2, \dots, k_n) \in A^n} \alpha_1^{(k_1)} \alpha_2^{(k_2)} \dots \alpha_n^{(k_n)} x^{(k_1, k_2, \dots, k_n)} \quad (4-15)$$

$$\text{s.t. } x^{(k_1, k_2, \dots, k_n)} \in \{0, 1\}, (k_1, k_2, \dots, k_n) \in A^n \quad (4-16)$$

$$\left(\sum_{i \in p_j} t_i^{(k_i)} \right) x^{(k_1, k_2, \dots, k_n)} - \sum_{i \in p_j} \lambda_{M,i} c_{M,i} - \sum_{i \in p_j} (t_i^{(k_i)} - t_i^{\text{ave}}) \lambda_{D,i} c_{D,i} \leq \Gamma, j \in V, \quad (4-17)$$

$$(k_1, k_2, \dots, k_n) \in A^n$$

$$\sum_{i \in W} c_{M,i} + \sum_{i \in W} c_{D,i} \leq C \quad (4-18)$$

$$0 \leq c_{M,i} \leq c_{M,i}^U, \quad i \in W \quad (4-19)$$

$$0 \leq c_{D,i} \leq c_{D,i}^U, \quad i \in W,$$

In this problem, the decision variables are $x^{(k_1, k_2, \dots, k_n)}$ as well as the allocating costs

$$\mathbf{c}_i = \begin{bmatrix} c_{M,i} \\ c_{D,i} \end{bmatrix}, \quad (4-20)$$

where the costs $c_{M,i}$ and $c_{D,i}$, which are two improving approaches are introduced in Section 4.3.2, are vector elements of allocating cost \mathbf{c}_i defined in (4-4) in this formulation. It can be seen that Equations (17) can be given by substituting (18) into Equation (3).

It is critical to note that eq. (4-17) is a constraint for the duration of path j that realize the logic

condition (4-13). Here I recall $\tilde{t}_i^{(k_i)}$, which is the duration after improvement from $t_i^{(k_i)}$. Since $\tilde{t}_i^{(k_i)}$ is a result of two kinds of improvement; the *improvement of expected value* (4-8) and the *improvement of dispersion* (4-9), $\tilde{t}_i^{(k_i)}$ can be written as

$$\tilde{t}_i^{(k_i)} = t_i^{(k_i)} - \lambda_{M,i} c_{M,i} - (t_i^{(k_i)} - t_i^{\text{ave}}) \lambda_{D,i} c_{D,i}. \quad (4-21)$$

Here summing (4-21) over all tasks on path j gives

$$\sum_{i \in p_j} \tilde{t}_i^{(k_i)} = \sum_{i \in p_j} t_i^{(k_i)} - \sum_{i \in p_j} \lambda_{M,i} c_{M,i} - \sum_{i \in p_j} (t_i^{(k_i)} - t_i^{\text{ave}}) \lambda_{D,i} c_{D,i}. \quad (4-22)$$

Using (4-22), I express the process completion time as the maximum value of $\sum_{i \in p_j} \tilde{t}_i^{(k_i)}$: among all paths $j \in V$,

$$(\text{Project completion time}) = \max_{j \in V} \sum_{i \in p_j} \tilde{t}_i^{(k_i)} \quad (4-23)$$

From (4-23), when $\sum_{i \in p_j} \tilde{t}_i^{(k_i)}$ is below the target completion time Γ for all paths, $j \in V$, the process completion time must be below Γ because the $\sum_{i \in p_j} \tilde{t}_i^{(k_i)}$ that satisfy (4-23) is also below Γ :

$$\begin{aligned} & (\text{Project completion time} \leq \Gamma) \\ & \Leftrightarrow \sum_{i \in p_j} \tilde{t}_i^{(k_i)} \leq \Gamma, j \in V. \end{aligned} \quad (4-24)$$

Substituting (4-22) into the bottom inequality in (4-24) gives

$$\sum_{i \in p_j} t_i^{(k_i)} - \sum_{i \in p_j} \lambda_{M,i} c_{M,i} - \sum_{i \in p_j} (t_i^{(k_i)} - t_i^{\text{ave}}) \lambda_{D,i} c_{D,i} \leq \Gamma, j \in V. \quad (4-25)$$

Here I note (4-17) can be obtained by multiplying binary variables $\mathcal{X}^{(k_1, k_2, \dots, k_n)}$ to the first term of (4-25). If the left hand side of (4-25) is over Γ , the binary variables $\mathcal{X}^{(k_1, k_2, \dots, k_n)}$ become zero because the constraint (4-17) can be satisfied only when $\mathcal{X}^{(k_1, k_2, \dots, k_n)}$ are zero. On the other hand, if the left

hand side of (4-25) is below Γ , the binary variables $\mathcal{X}^{(k_1, k_2, \dots, k_n)}$ can take either value, but the number of positive binary variables $\mathcal{X}^{(k_1, k_2, \dots, k_n)}$ is maximized since the objective function (4-15) should be maximized. From the discussion above, the logic condition (4-13) is rewritten to the constraints (4-17).

Note that the problem size of the above formulation TOF is very large due to the large number of binary variables $\mathcal{X}^{(k_1, k_2, \dots, k_n)}$. The number of the binary variables $\mathcal{X}^{(k_1, k_2, \dots, k_n)}$ is m^n because they are defined as enumerations $(k_1, k_2, \dots, k_n) \in A^n$ of all possible random variables $t_i^{(k_i)}$, $i \in W$. In the next section, I show another formulation that reduces the problem size.

4.5 Path-Oriented Formulation

I show an alternative formulation to (4-3)–(4-5) that has a smaller number of decision variables than TOF . The large number of decision variables in TOF was due to the large number of discretized bins for task durations. In the reformulation given below, I reduce the decision variables by considering the duration of each path, instead of each task. This reduction in the problem size is possible because the number of all paths in a process is significantly smaller than the total number of tasks. Note that in this reformulation, I only consider the *improvement of the expected value* (4-8) ignoring the *improvement of dispersion* (4-9) (i.e. $c_{D,i} = 0$, $i \in W$).

4.5.1 Preparation for Path-Oriented Formulation

Firstly I rewrite Eq. (4-3) in case ignoring the *improvement of dispersion*. Since ignoring the *improvement of dispersion*, the improved duration $\tilde{t}_i^{(k_i)}$ is expressed as (4-8). By substituting (4-8) into (4-24), I obtain

$$\begin{aligned} & \Pr[\text{Project completion time} \leq \Gamma] \\ &= \Pr\left[\sum_{i \in p_j} \tilde{t}_i^{(k_i)} - \sum_{i \in p_j} \lambda_{M,i} c_{M,i} \leq \Gamma, j \in V\right]. \end{aligned} \quad (4-26)$$

While (4-26) is important since it is another expression of the objective function (4-3), here I introduce some definitions that help rewriting (4-3) using (4-26) in a useful form. At first, I define discrete time to describe path durations as $T^{(v_j)}, j \in V$ in which the index v_j for the random variable is within a set M :

$$v_j \in M, M = \{0, 1, 2, \dots, l-1, l\} \quad (4-27)$$

where l is the longest bin number of $v_j, j \in V$. Here I define *critical duration of path j* that is equivalent with the target completion time Γ after allocating costs $c_{M,i}, i \in W$ as

$$T^{(v_{j,\text{crit}})} - \sum_{i \in p_j} \lambda_{M,i} c_{M,i} = \Gamma. \quad (4-28)$$

Here I define a parameter $h^{(v'_1, v'_2, \dots, v'_r)}$ which is the probability that sum of task durations $\sum_{i \in p_j} \tilde{t}_i^{(k_i)}$

is smaller than $T^{(v'_j)}$ for all paths $j \in V$:

$$h^{(v'_1, v'_2, \dots, v'_r)} = \Pr\left[\sum_{i \in p_j} \tilde{t}_i^{(k_i)} \leq T^{(v'_j)}, j \in V\right], \quad (4-29)$$

$$(v'_1, v'_2, \dots, v'_r) \in M^r, \quad (4-30)$$

where v_j' is the index for a given realization of the random variable $T^{(v_j')}$. By substituting (4-28) into (4-29),

$$\begin{aligned} h^{(v_{1\text{crit}}, v_{2\text{crit}}, \dots, v_{r\text{crit}})} &= \Pr \left[\sum_{i \in p_j} t_i^{(k_i)} \leq T^{(v_{j\text{crit}})}, j \in V \right] \\ &= \Pr \left[\sum_{i \in p_j} t_i^{(k_i)} - \sum_{i \in p_j} \lambda_{M,i} c_{M,i} \leq \Gamma, j \in V \right]. \end{aligned} \quad (4-31)$$

By substituting (4-26) into (4-31), I can rewrite (4-3) by using $h^{(v_1, v_2, \dots, v_r)}$ as

$$\begin{aligned} &\Pr[\text{Project completion time} \leq \Gamma] \\ &= h^{(v_{1\text{crit}}, v_{2\text{crit}}, \dots, v_{r\text{crit}})}. \end{aligned} \quad (4-32)$$

Note that the parameters $h^{(v_1, v_2, \dots, v_r)}$ is calculated by summing the probability (4-11). It is defined in (4-29) that $h^{(v_1', v_2', \dots, v_r')}$ is the probability that the following condition is satisfied:

$$\sum_{i \in p_j} t_i^{(k_i)} \leq T^{(v_j')}, j \in V. \quad (4-33)$$

Here I define a set $H^{(v_1', v_2', \dots, v_r')}$, which includes all (k_1, k_2, \dots, k_n) that satisfies the condition (4-33) as follows:

$$\begin{aligned} H^{(v_1', v_2', \dots, v_r')} &= \left\{ (k_1, k_2, \dots, k_n) \in A^n \mid \sum_{i \in p_j} t_i^{(k_i)} \leq T^{(v_j')}, j \in V \right\}, \\ &\quad (v_1', v_2', \dots, v_r') \in M^r. \end{aligned} \quad (4-34)$$

Using the set defined in (4-34), $h^{(v_1', v_2', \dots, v_r')}$ can be rewritten as

$$h^{(v_1', v_2', \dots, v_r')} = \sum_{(k_1, k_2, \dots, k_n) \in H^{(v_1', v_2', \dots, v_r')}} \Pr \left[t_i^{(k_i)} = t_i^{(k_i')}, i \in W \right]. \quad (4-35)$$

Finally, by substituting (4-11) into (4-35), I obtain

$$h^{(v_1', v_2', \dots, v_r')} = \sum_{(k_1, k_2, \dots, k_n) \in H^{(v_1', v_2', \dots, v_r')}} \alpha_1^{(k_1)} \alpha_2^{(k_2)} \dots \alpha_n^{(k_n)}. \quad (4-36)$$

This calculation to prepare the parameters $h^{(v_1, v_2, \dots, v_r)}$ should be executed before solving optimization problems shown in *POF*.

4.5.2 Path-Oriented Formulation

From the discussion above, (4-3)–(4-5) can be reformulated into an even simpler form. Firstly I show the overall reformulation and discuss the objective function and constraints later. The correspondence between two formulations, the *CPM without uncertainty* and the *Path-Oriented Formulation* is as follows: (4-3)→{(4-37), (4-38), (4-39), (4-42)}, (4-4)→(4-40), (4-5)→(4-41).

Path-Oriented Formulation (POF)

$$\text{Maximize: } \sum_{(v_1, v_2, \dots, v_r) \in M^r} h^{(v_1, v_2, \dots, v_r)} z^{(v_1, v_2, \dots, v_r)} \quad (4-37)$$

$$\text{s.t. } \sum_{(v_1, v_2, \dots, v_r) \in M^r} z^{(v_1, v_2, \dots, v_r)} = 1, \quad (4-38)$$

$$T^{(v_j)} \cdot z^{(v_1, v_2, \dots, v_r)} - \sum_{i \in p_j} \lambda_{M,i} c_{M,i} \leq \Gamma, \quad j \in V, \quad (4-39)$$

$$\sum_{i \in W} c_{M,i} \leq C, \quad (4-40)$$

$$0 \leq c_{M,i} \leq c_{M,i}^U, \quad i \in W. \quad (4-41)$$

$$z^{(v_1, v_2, \dots, v_r)} \in \{0, 1\}, \quad (v_1, v_2, \dots, v_r) \in M^r. \quad (4-42)$$

where $z^{(v_1, v_2, \dots, v_r)} \in \{0, 1\}$ are binary variables that enumerate all possible realizations of the random variables. Decision variables are the binary variables $z^{(v_1, v_2, \dots, v_r)}$ and allocating costs of task i as $c_{M,i}$.

I consider a logic condition such that only one of the binary variables $z^{(v_1, v_2, \dots, v_r)} \in \{0, 1\}$ becomes positive when the condition (4-28) is satisfied, and other binary variables become zero:

$$z^{(v'_1, v'_2, \dots, v'_r)} = \begin{cases} 1 & \text{if } T^{(v'_j)} = T^{(v_{j\text{crit}})}, j \in V \\ 0 & \text{otherwise} \end{cases} \quad (4-43)$$

By multiplying $h^{(v_1, v_2, \dots, v_r)}$ to $z^{(v_1, v_2, \dots, v_r)}$ and summing them for all combinations of realization of indices (v_1, v_2, \dots, v_r) , $h^{(v_{1\text{crit}}, v_{2\text{crit}}, \dots, v_{r\text{crit}})}$ can be expressed as

$$\sum_{(v_1, v_2, \dots, v_r) \in M^r} h^{(v_1, v_2, \dots, v_r)} z^{(v_1, v_2, \dots, v_r)} = h^{(v_{1\text{crit}}, v_{2\text{crit}}, \dots, v_{r\text{crit}})}, \quad (4-44)$$

which is obtained from the logic condition (4-43). By substituting (4-44) into (4-32), it can be shown that Eq.(4-3) is equivalent with (4-37):

$$\begin{aligned} & \Pr[\text{Project completion time} \leq \Gamma] \\ &= h^{(v_{1\text{crit}}, v_{2\text{crit}}, \dots, v_{r\text{crit}})} \\ &= \sum_{(v_1, v_2, \dots, v_r) \in M^r} h^{(v_1, v_2, \dots, v_r)} z^{(v_1, v_2, \dots, v_r)}, \end{aligned} \quad (4-45)$$

while satisfying the logic condition (4-43).

The logic condition (4-43) is satisfied in the optimal solution of the *POF*. The mathematical proof is given in the following. Firstly, I show a condition that the binary variables $z^{(v_1, v_2, \dots, v_r)}$ satisfies. Here note that from the (4-29), which is the definition of $h^{(v_1, v_2, \dots, v_r)}$, it is obvious that the $h^{(v_1, v_2, \dots, v_r)}$ increases monotonically as the index j of random variables $v_j, j \in V$ increases:

$$h^{(v_1, v_2, \dots, v_j, \dots, v_r)} \leq h^{(v_1, v_2, \dots, v_{j+1}, \dots, v_r)}, j \in V. \quad (4-46)$$

Therefore, to maximize the objective function (4-37) under the constraint (4-38), the following condition must be satisfied:

$$z^{(v_1, v_2, \dots, v_j, \dots, v_r)} \leq z^{(v_1, v_2, \dots, v_{j+1}, \dots, v_r)}, j \in V. \quad (4-47)$$

Secondly, from Eq. (4-28), I have:

$$T^{(v_{j\text{eff}})} - \sum_{i \in p_j} \lambda_{M,i} c_{M,i} \begin{cases} > \Gamma \text{ if } v_j > v_{j\text{crit}} \\ = \Gamma \text{ if } v_j = v_{j\text{crit}} \\ < \Gamma \text{ if } v_j < v_{j\text{crit}} \end{cases}, j \in V. \quad (4-48)$$

Finally, from Eq. (4-47), Eq. (4-48) and the constraint (4-38), the following condition is satisfied under the constraints (4-39):

$$z^{(v'_1, v'_2, \dots, v'_r)} = \begin{cases} 0 \text{ if } v_j > v_{j\text{crit}} \\ 1 \text{ if } v_j = v_{j\text{crit}} \\ 0 \text{ if } v_j < v_{j\text{crit}} \end{cases}, j \in V. \quad (4-49)$$

It can be seen that Eq.(4-49) is equivalent with (4-43). From the discussions above, it is proved that Eq.(4-43) is satisfied at the optimal solution of *POF*.

4.6 Path-Oriented Formulation with Local Search Algorithm

In this section, a local search method for *POF* is proposed in order to further reduce decision variables and constraints of *POF*. I denote the *Path-Oriented Formulation with Local Search Algorithm* proposed in this section as *(POF, Local Search)*. In contrast, I call the original *POF* as *(POF, Strict)*.

4.6.1 Concept of *(POF, Local Search)*

A comparison between *(POF, Strict)* and *(POF, Local Search)* is illustrated in Figure 4-10. Note that the formulation *(POF, Strict)* finds certain indices of discrete random variables $(v_1^*, v_2^*, \dots, v_r^*)$ that corresponds to the optimal solution of *(POF, Strict)* that satisfies $z^{(v_1^*, v_2^*, \dots, v_r^*)} = 1$. This method uses the full search from all candidates of $(v_1^*, v_2^*, \dots, v_r^*)$. On the other hand, in *(POF, Local Search)*, I limit the search within a local region and consider a limited number of candidates for $(v_1^*, v_2^*, \dots, v_r^*)$. After this local search, I search the neighboring regions until the algorithm terminates.

Note that as shown in Figure 4-10, the search range of *(POF, Strict)* for all paths is expressed as (4-30). On the other hand, in *(POF, Local Search)*, the limited search range on path j is around $(v_1^{\text{ref}}, v_2^{\text{ref}}, \dots, v_r^{\text{ref}})$ that is a realization of some combination of the indices:

$$\bar{M}_j = \{v_j^{\text{ref}} - \beta, \dots, v_j^{\text{ref}} - 1, v_j^{\text{ref}}, v_j^{\text{ref}} + 1, \dots, v_j^{\text{ref}} + \beta\}, \quad (4-50)$$

where β is a parameter. Using (4-50), the narrowed candidates of index for discrete random variables discrete random variables is given by:

$$(v_1, v_2, \dots, v_r) \in \bar{M}_1 \times \bar{M}_2 \times \dots \times \bar{M}_r. \quad (4-51)$$

If the set given by (4-51) contains $(v_1^*, v_2^*, \dots, v_r^*)$, $(POF, Local Search)$ can find the optimal solution.

Note that the local search method does not guarantee global optimality. Since the candidates of the binary variable $z^{(v_1^*, v_2^*, \dots, v_r^*)}$ is limited, the global optimal solution may not be found if it lies outside the search region. This disadvantage must be weighed carefully against the advantage of the significantly shorter computational time as demonstrated in our case study.

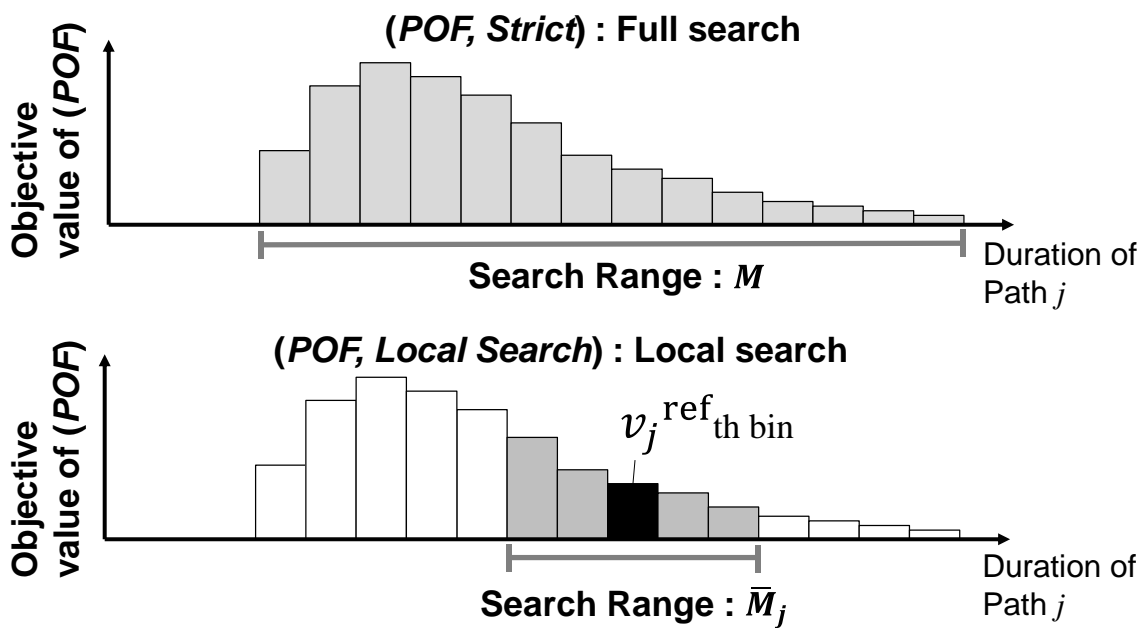


Figure 4-10. Comparison between the $(POF, Strict)$ and $(POF, Local Search)$

4.6.2 Detailed algorithm of (POF, Local Search)

The flow chart of this algorithm is shown in Figure 4-11. In Steps 1 and 2, an initial guess to set the search range (4-51) is obtained. Step 3 is to prepare parameters to be used in Step 4, which is the step to solve *POF* where the search range is narrowed down. In Step 5, the optimality is checked by comparing the value of the objective function.

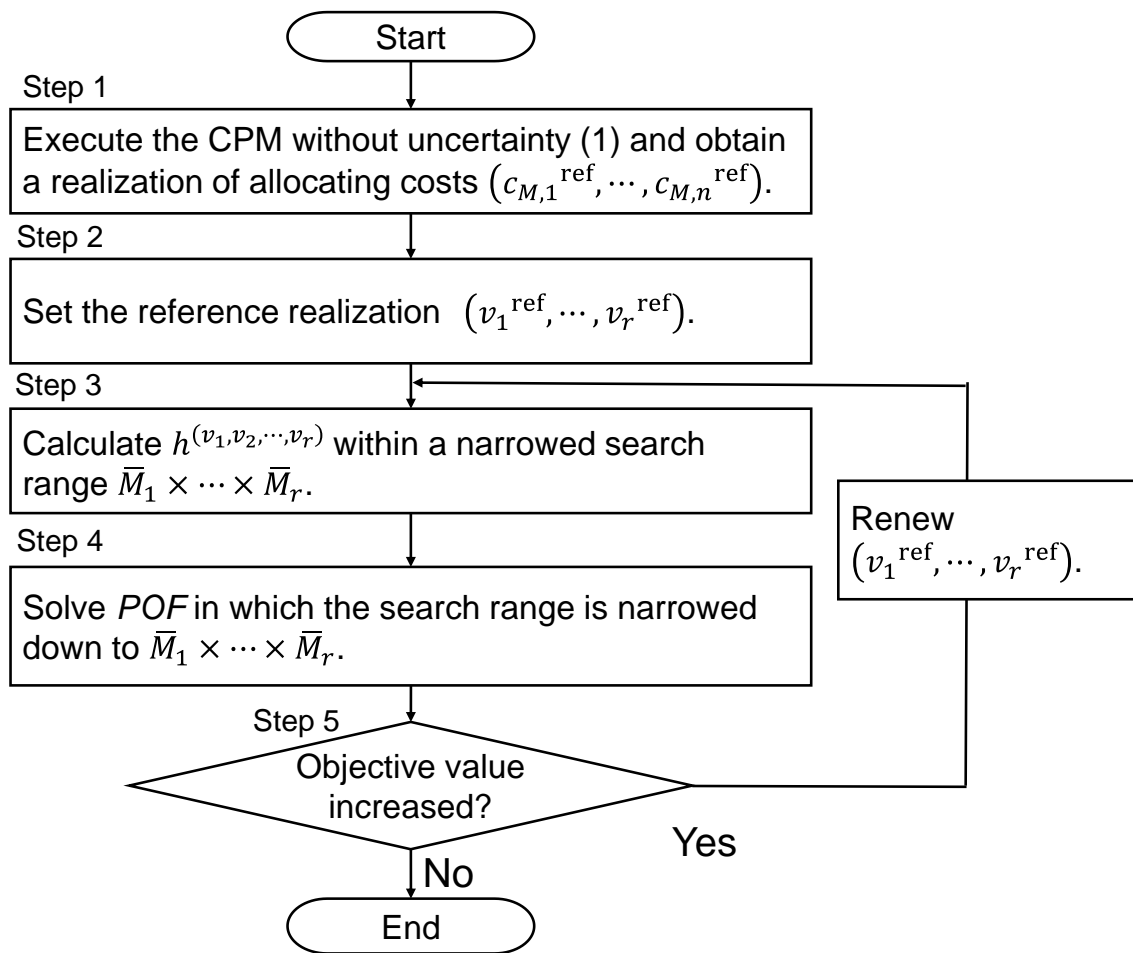


Figure 4-11. Flow chart of the algorithm of (POF, Local Search)

Step 1

In this step, I find one realization of allocating costs $(c_{M,1}^{\text{ref}}, c_{M,2}^{\text{ref}}, \dots, c_{M,n}^{\text{ref}})$ as a reference solution to find an initial guess to set the search range. Here I attempt to use the solution of the *CPM without uncertainty* shown in (4-2) as the realization of allocating costs $(c_{M,1}^{\text{ref}}, c_{M,2}^{\text{ref}}, \dots, c_{M,n}^{\text{ref}})$. In this study, I assume that the fixed task duration t_i in (4-2) is calculated by $t_i = t_i^{\text{ave}}$.

Step 2

In this step, I decide the reference realization of the indices as $(v_1^{\text{ref}}, v_2^{\text{ref}}, \dots, v_r^{\text{ref}})$ for $\left(T_1^{(v_1^{\text{ref}})}, T_2^{(v_2^{\text{ref}})}, \dots, T_r^{(v_r^{\text{ref}})}\right)$. Using this reference realization, the search range can be determined as shown in (4-50). To find the optimal solution, the candidates for search (4-51) must contain $(v_1^*, v_2^*, \dots, v_r^*)$. Therefore, the realization $(v_1^{\text{ref}}, v_2^{\text{ref}}, \dots, v_r^{\text{ref}})$, which is at the center of the search range, needs to be sufficiently close to $(v_1^*, v_2^*, \dots, v_r^*)$. However, $(v_1^*, v_2^*, \dots, v_r^*)$ cannot be found without executing *POF* and find optimal cost allocation $(c_{M,1}^*, c_{M,2}^*, \dots, c_{M,n}^*)$. Here, I attempt to use $(c_{M,1}^{\text{ref}}, c_{M,2}^{\text{ref}}, \dots, c_{M,n}^{\text{ref}})$ and set $(v_1^{\text{ref}}, v_2^{\text{ref}}, \dots, v_r^{\text{ref}})$ to satisfy a similar condition to (4-28) as

$$v_j^{\text{ref}} = \arg_{v_j} \left(T^{(v_j)} - \sum_{i \in p_j} \lambda_{M,i} c_{M,j}^{\text{ref}} = \Gamma \right). \quad (4-52)$$

Step 3

In this step, the problem *POF* is prepared where the search range is narrowed down. Firstly I construct the local search range around the reference indices $(v_1^{\text{ref}}, v_2^{\text{ref}}, \dots, v_r^{\text{ref}})$ as given in (4-50), where the candidates of discrete random variables is given by (4-51). Similarly with (4-34), here I

define a set of (k_1, k_2, \dots, k_n) that satisfies the condition (4-33) for the indices (4-51) where the search range is narrowed down:

$$\bar{H}^{(v'_1, v'_2, \dots, v'_r)} = \left\{ (k_1, \dots, k_n) \in A^n \mid \sum_{i \in p_1} t_i^{(k_i)} \leq T_1^{(v_1)}, \dots, \sum_{i \in p_r} t_i^{(k_i)} \leq T_r^{(v_r)} \right\}, \quad (4-53)$$

$$(v'_1, v'_2, \dots, v'_r) \in \bar{M}_1 \times \bar{M}_2 \times \dots \times \bar{M}_r.$$

Additionally, I calculate the probability (4-29) where the search range is narrowed down:

$$h^{(v'_1, v'_2, \dots, v'_r)} = \Pr \left[\sum_{i \in p_j} t_i^{(k_i)} \leq T_j^{(v'_j)}, j \in V \right], \quad (4-54)$$

$$\text{for } (k_1, k_2, \dots, k_n) \in \bar{H}^{(v'_1, v'_2, \dots, v'_r)}.$$

Step 4

I solve the following problem, which is a modification to *POF*:

$$\begin{aligned} & \text{Maximize:} && \sum_{(v_1, v_2, \dots, v_r) \in \bar{M}_1 \times \bar{M}_2 \times \dots \times \bar{M}_r} h^{(v_1, v_2, \dots, v_r)} \cdot z^{(v_1, v_2, \dots, v_r)} \\ & \text{s.t.} && z^{(v_1, v_2, \dots, v_r)} \in \{0, 1\}, (v_1, v_2, \dots, v_r) \in \bar{M}_1 \times \bar{M}_2 \times \dots \times \bar{M}_r \\ & && T_j^{(v_j)} \cdot z^{(v_1, v_2, \dots, v_r)} - \sum_{i \in p_j} \lambda_{M,i} c_{M,i} \leq \Gamma, j \in V, \\ & && \sum_{(v_1, v_2, \dots, v_r) \in \bar{M}_1 \times \bar{M}_2 \times \dots \times \bar{M}_r} z^{(v_1, v_2, \dots, v_r)} = 1, \\ & && \sum_{i \in W} c_{M,i} \leq C, \\ & && 0 \leq c_{M,i} \leq c_{M,i}^U, \quad i \in W. \end{aligned} \quad (4-55)$$

where in contrast to *POF*, the range of possible index of random variables (4-30) is replaced by the narrowed range (4-51). Note that the optimal solution of (4-55) may be different from the optimal

solution of *POF*; only if the search range (4-51) contains $(v_1^*, v_2^*, \dots, v_r^*)$ I obtain $h^{(v_{1\text{crit}}, v_{2\text{crit}}, \dots, v_{r\text{crit}})}$ as

the objective value. Even if (4-55) cannot find the optimal solution of *POF*, by executing (4-55) I can

find equivalent or better candidate where the objective value is higher compared to the reference value

$$h(v_1^{\text{ref}}, v_2^{\text{ref}}, \dots, v_r^{\text{ref}}).$$

Step 5

This step is to decide whether the search in Step 3 is sufficient by comparing the objective function.

If the binary variables $z^{(v_1, v_2, \dots, v_r)}$ is the same as those in the previous execution of Step 4, I terminate the algorithm. If the solution is changed, return to Step 3 with new reference indices $(v_1^{\text{ref}}, v_2^{\text{ref}}, \dots, v_r^{\text{ref}})$ which is the solution of Step 4.

4.7 Case studies

In this section, I present some examples to demonstrate the proposed methods. I compare the following three approaches: the *CPM without uncertainty*, the proposed formulation *TOF* and *POF*.

4.7.1 Example 1

In this example, I consider a simple CCUS system shown in Figure 4-12, which shows the structure as well as the normalized distribution of each task. Table 4-1 shows the historical data for task duration

$N_i[t_i^{(k_i)}]$, and the sum of samples $\sum_{k_i \in A} N_i[t_i^{(k_i)}]$ for all tasks. Note that $N_i[t_i^{(k_i)}]$ is introduced in

Section 3.1. For simplicity, I express $N_i[t_i^{(k_i)}]$ as $N_i[t_i^{(k_i)}] = N_i^{(k_i)}$.

In this example, I assume that the widths of all bins is constant. Thus, I have

$$t_i^{(k_i)} - t_i^{(k_i-1)} = a, (i = 1, 2, \dots, 4). \tag{4-56}$$

Additionally, I set $a = 5$, and the widths of all bins are equally spaced. Table 4-2 shows other parameters.

The maximum total cost and process completion time are given as follows: $C = 250$ and $\Gamma = 100$.

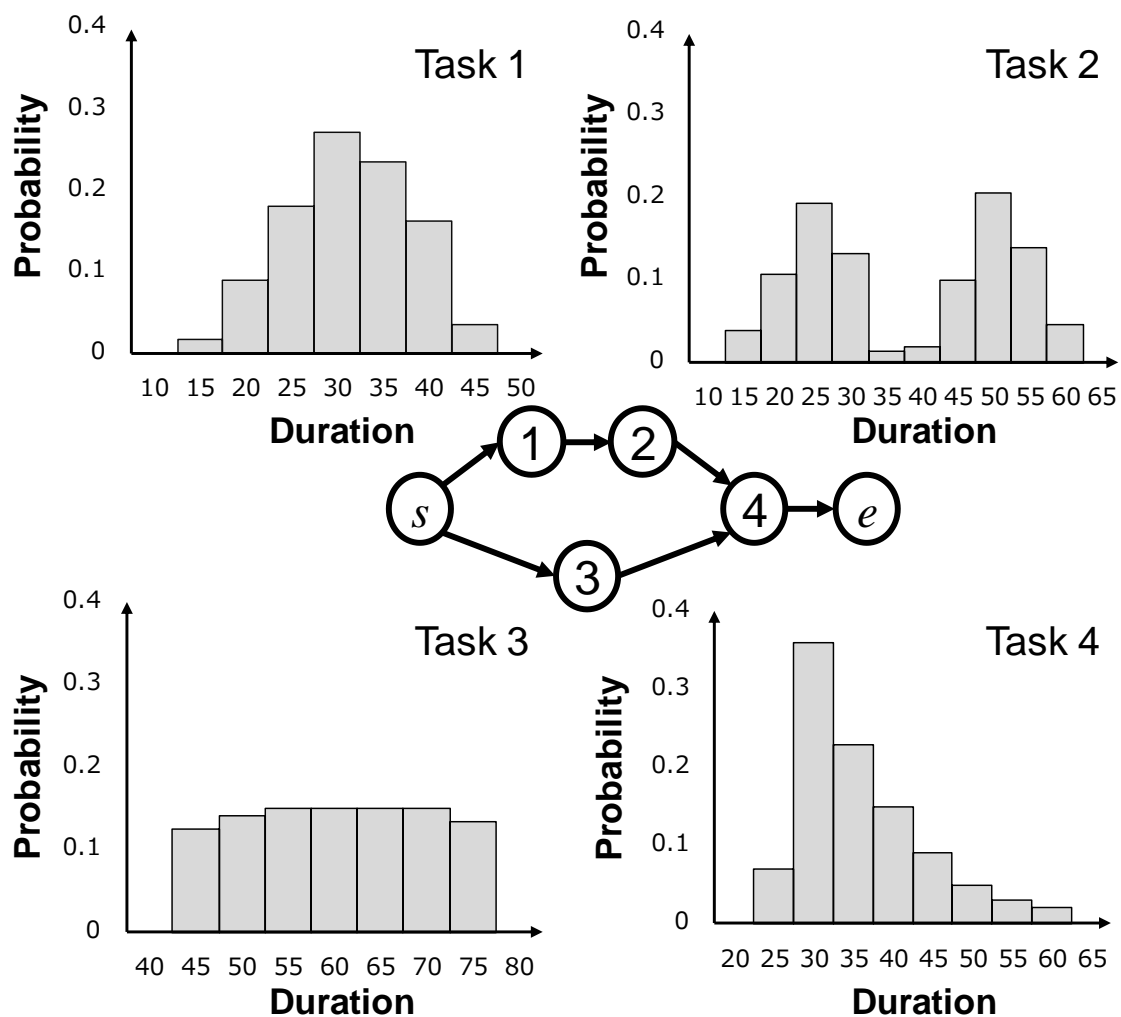


Figure 4-12. A CCUS system of Example 1

Table 4-1 Historical operation data for Example 1

Task i	$N_i^{(1)}$	$N_i^{(2)}$	$N_i^{(3)}$	$N_i^{(4)}$	$N_i^{(5)}$	$N_i^{(6)}$	$N_i^{(7)}$	$N_i^{(8)}$	$N_i^{(9)}$	$N_i^{(10)}$	$\sum_{k_i \in A} N_i^{(k_i)}$
1	2	10	20	30	26	18	4	-	-	-	110
2	6	16	29	20	2	3	15	31	21	7	150
3	15	17	18	18	18	18	16	-	-	-	120
4	7	36	23	15	9	5	3	2	-	-	100

Table 4-2 Parameters of the system in Example 1

Task i	$t_i^{(0)}$	$\lambda_{M,i}$	$c_{M,i}^U$	$\lambda_{D,i}$	$c_{D,i}^U$
1	15	0.24	40	0.020	30
2	15	0.15	125	0.015	40
3	45	0.20	125	0.010	40
4	25	0.090	100	0.020	30

Table 4-3 Results of example 1

	<i>CPM without uncertainty</i>	<i>TOF</i>	
		<i>w/o dispersion improvement</i>	<i>with dispersion improvement</i>
# of decision variables	9	3924	3928
# of constraints	20	7849	7857
Task i	$c_{M,i}$	$c_{M,i}$	$c_{M,i}$ $c_{D,i}$
1	40.00	40.00	40.00 10.00
2	61.80	80.00	1.040 40.00
3	48.20	30.00	25.27 3.685
4	100.0	100.0	100.0 30.00
Probability finished by Γ	N/A (0.8652)	0.9070	0.9444
Computational time	<1s	17s	1027s

Table 4-3 shows the results for Example 1 by the conventional approach, *CPM without uncertainty* and the proposed approach, *TOF*. In this example, I use the original formulation of the *CPM without uncertainty* shown in Eq. (4-2), where task duration $t_i, i \in W$ is fixed values while in this example task durations are given as the historical operation data in Table 4-1. In this study, I use the average duration t_i^{ave} defined in Eq.(4-10) in place of the duration t_i as $t_i = t_i^{\text{ave}}, i \in W$. On the other hand, for the *TOF*, the proposed formulation in Section 4.4.2, I implemented two approaches in this example: *without (w/o) dispersion improvement* and *with dispersion improvement*. In the former approach, I do not consider improvement of dispersions ($c_{M,i} = 0, i \in W$) to compare it against the conventional approach

based on the same degree of freedom. In the latter approach of *TOF*, I consider both improvements, expected values and dispersions.

I implemented these approaches on a desktop personal computer with a core i7, 3.4GHz processor. I used Numerical Optimizer from NTT DATA Mathematical Systems Inc. (Tokyo, Japan). The algorithm in this solver is based on the branch-and-bound method.

The *CPM without uncertainty* leads to a low value of the objective function, 0.8652, compared to the one calculated by the proposed methods. This value was calculated by simply applying to the optimal cost allocations obtained by the *CPM without uncertainty* to the original problem that includes the uncertainty of task durations. This result indicates ignoring the problem uncertainty leads to poor cost allocation when task durations are uncertain.

Here note that the objective value of *TOF with dispersion improvement*, 0.9444, is even higher than that of *(TOF) without dispersion improvement*, 0.9070; this difference is the result of the higher degrees of freedom by the improvement in the dispersion of task duration histograms.

The advantages in the objective values discussed above are obtained at a cost of significantly longer computational time. In this example, the *CPM without uncertainty* needed only a short computational time (< 1s) because the problem size is very small. In contrast, *TOF without dispersion improvement* needed a significantly longer computational time, 17 s, and that for *TOF with dispersion improvement* is even two orders of magnitudes larger, 1027 s, because of the complexity of algorithm. From this

result, I see that considering improvement of dispersion in addition to improvement of expected value of task duration histograms makes the problem much more difficult to solve.

I also analyze the optimal solution of *TOF without uncertainty*, and note that the allocation cost $c_{D,2}$, which is the improved dispersion of Task 2, is the highest among all allocation costs $c_{D,i}$, $i \in \mathcal{W}$. This is because the dispersion of the task duration histogram in Task 2 is significantly larger than that of other tasks (see Figure 4-12), and thus improving this wide profile of task duration is effective.

4.7.2 Example 2

To further observe the influence of the problem size of the proposed methods *TOF*, (*POF, Strict*) and (*POF, Local Search*), I apply these methods to another example that has a larger number of tasks and paths. Another CCUS system of Example 2 is shown in Figure 4-13, and historical operation data are given in Table 4-4 and Table 4-5. In this problem, I set the maximum total cost C and the process completion time Γ as follows: $C = 350$ and $\Gamma = 180$.

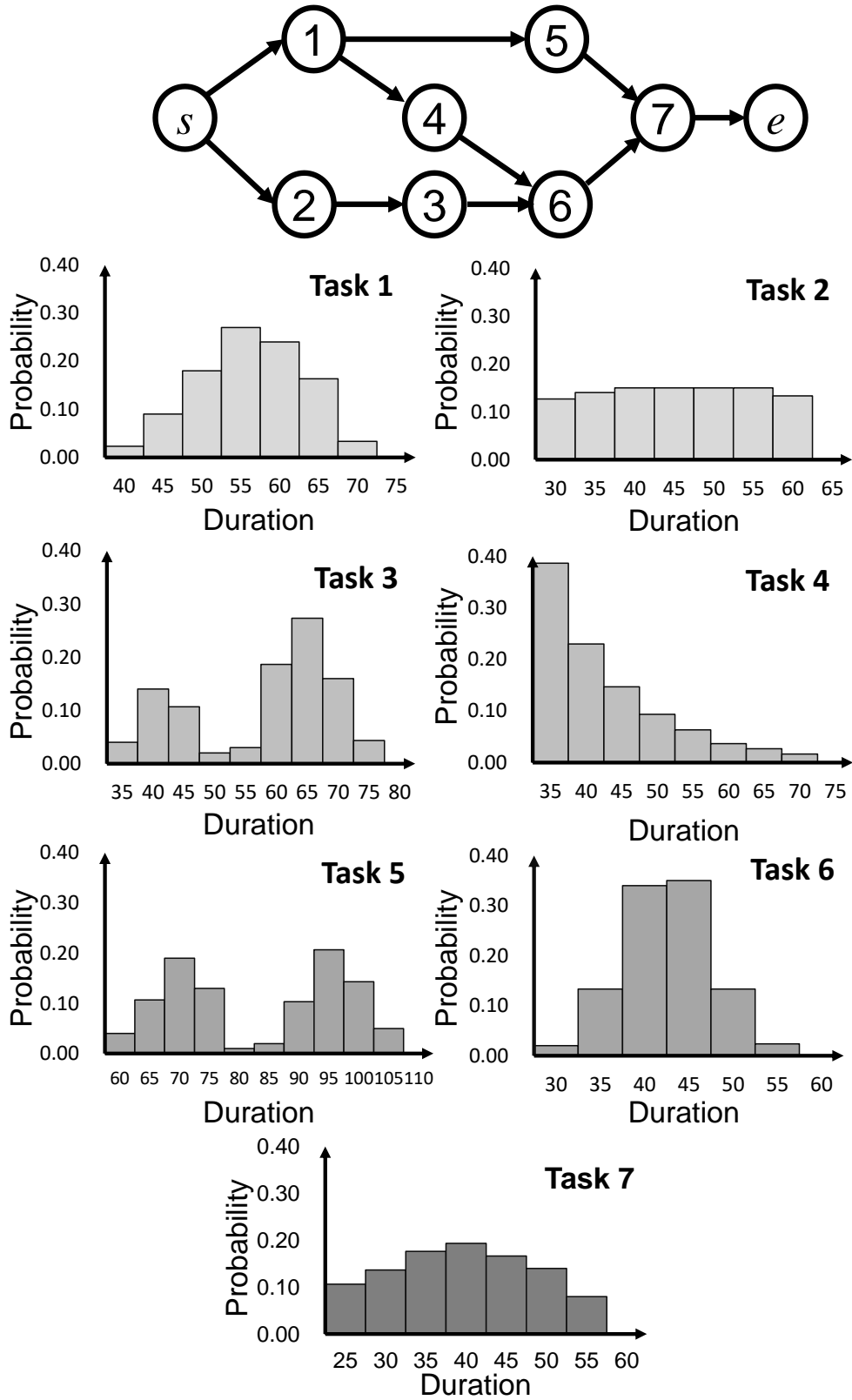


Figure 4-13. A CCUS system of Example 2

Table 4-4 Historical operation data for Example 2

Task i	$N_i^{(1)}$	$N_i^{(2)}$	$N_i^{(3)}$	$N_i^{(4)}$	$N_i^{(5)}$	$N_i^{(6)}$	$N_i^{(7)}$	$N_i^{(8)}$	$N_i^{(9)}$	$N_i^{(10)}$	$\sum_{k_i \in A} N_i^{(k_i)}$
1	7	27	54	81	72	49	10	-	-	-	300
2	38	42	45	45	45	45	40	-	-	-	300
3	12	42	32	6	9	56	82	48	13	-	300
4	116	69	44	28	19	11	8	5	-	-	300
5	12	32	57	39	3	6	31	62	43	15	300
6	6	40	102	105	40	7	-	-	-	-	300
7	32	41	53	58	50	42	24	-	-	-	300

Table 4-5 Parameters of the system in Example 2

Task i	$t_i^{(0)}$	$\lambda_{M,i}$	$c_{M,i}^U$
1	40	0.15	75
2	30	0.15	125
3	35	0.20	100
4	35	0.25	150
5	60	0.15	175
6	30	0.15	75
7	25	0.10	50

Table 4-6 Results of Example 2

	<i>TOF</i> <i>w/o dispersion</i> <i>improvement</i>	<i>(POF, Strict)</i>	<i>(POF, Local Search)</i> Search range $\beta = 2$
# of decision variables	2469614	14307	132
# of constraints	7408815	42914	410
Task i	$C_{M,i}$	$C_{M,i}$	$C_{M,i}$
1	-	75.00	75.00
2	-	0.000	0.000
3	-	75.74	100.0
4	-	20.59	15.00
5	-	67.65	76.67
6	-	75.00	33.33
7	-	36.03	50.00
Probability finished by Γ	N/A (0.8635)	0.8635	0.8635
Calculation time of $h^{(v_1, v_2, \dots, v_r)}$	< 24h	95s	5s (Sum for two iterations)
Calculation time to solve	< 24h	29s	1s < (Sum for two iterations)

Table 4-6 shows the solutions and computational statistics for Example 2. Note that *TOF without dispersion improvement* in this table is the same method introduced in Example 1; *(POF, Strict)* in this table is the *Path-Oriented Formulation* shown in Section 4.5; *(POF, Local Search)* is the *Path-Oriented Formulation with Local Search Algorithm* shown in Section 4.6. It should be noted that *(POF, Strict)* and *(POF, Local Search)* can only consider improvement of expected value, and thus I compare

TOF without dispersion improvement, not with dispersion improvement. In addition, note that the complex calculation of $h^{(v_1, v_2, \dots, v_r)}$ that appears in (4-29) and (4-54), which must be performed before solving the optimization problems for (*POF, Strict*) and (*POF, Local Search*), requires a significant amount of computational time; the computational time for this parameter is shown as “Calculation time of $h^{(v_1, v_2, \dots, v_r)}$,” in this table.

I compare the problem sizes and computational times in these three methods. It can be seen that *TOF* has the largest number of decision variables, 2469614, and constraints, 7408815. In contrast, (*POF, Strict*) has a significantly smaller number of decision variables, 14307, and constraints, 42914, than *TOF*. Furthermore, (*POF, Local Search*) has an even smaller number of decision variables and constraints than other two methods. The numbers of decision variables, 132, and constraints 410, are for the first iteration, out of the total of the two iterations. Due to the large number of variables and constraints, *TOF* cannot be solved in 24 hours. In contrast, (*POF, Strict*) and (*POF, Local Search*) can be solved much faster than *TOF*, in which calculation time of (*POF, Strict*) is 29 seconds and that of (*POF, Local Search*) is below 1 second. Note that the actual calculation time of (*POF, Strict*) and (*POF, Local Search*) is the sum of “Calculation time of h ” and “Calculation time to solve”, where (*POF, Strict*) needed $95 + 29 = 134$ seconds and (*POF, Local Search*) needed only about 5~6 seconds. These computational times are significantly smaller than that for *TOF*.

It can be seen in Table 4-6 that while the objective values in (*POF, Strict*) and (*POF, Local Search*) are the same, 0.8635, the optimal cost allocations found by these two methods are significantly

different. This non-uniqueness of the optimal solution is due to Eq. (4-28), where many different combinations of the allocating cost $c_i, i \in W$ exist that gives a single value of $T^{(v_{\text{crit}})}$.

I can also find a general rule for cost allocations about tasks that are in series without any branching or merging: in this example, Task 2 and 3. In the optimal solution, the allocating cost on Task 2 is zero ($c_{M,2} = 0$) in both *(POF, Strict)* and *(POF, Local Search)*, while for Task 3, which is the subsequent task to Task 2, a significant amount of cost is allocated. This is because the cost coefficient for Task 3, $\lambda_{M,3} = 0.20$, is higher than that for Task 2, $\lambda_{M,2} = 0.15$. Since the improvement of either task has the same influence on the process completion time, improving Task 3, which has the greater benefit for a given cost than Task 2, should be pursued.

4.8 Concluding remarks and future work

In this chapter, proposed an advanced CPM technique that maximizes the process completion probability within a target completion time, which can utilize historical data from systems to handle uncertain task durations. My method has three main advantages; handling the operation data without approximation; considering the time-cost trade off by two kinds of improvement of task duration; finding the optimal solution by formulating the problem as MILP. I proposed two formulations: *Task-Oriented Formulation (TOF)*, and *Path-Oriented Formulation (POF)*. Furthermore, I proposed the *Path-oriented Formulation with Local Search*, which applies the local search algorithm to *POF* and shortens the computational time. In addition, I applied these three formulations to two examples and demonstrated the effectiveness of our approach.

To address more practical issues, the following are potential room for improvements in the proposed approaches. Firstly, I will apply a real-time optimization method to my proposed formulations. There have been considerable advances in real-time data acquisition techniques in recent years, so historical operation data can be obtained in real-time easily. However, in implementing such real-time optimization approaches, the validity of the improvement model should be examined carefully; various formulations including our formulations have proportionality constants for improving duration of tasks per additional costs,^{111,154,160} which are approximations based on experience. The real-time operation data may be utilized to realize a successive optimization and modeling approach, where the optimal solution is implemented and then the proportionality constant is updated in an alternate and iterative manner in real time. In such an iterative optimization and modeling approach, the *Total cost C* can be divided and distributed to each time period.

Secondly, in *POF*, we needed to ignore the *improvement in dispersion*, which is considered only in *TOF*. Considering the *improvement of dispersion* allow to model variety of possible improvements. The concept of the *improvement of dispersion* to *POF* should also be extended to the local search method.

Thirdly, the problem I reformulated is a single-objective optimization problem; however, scheduling problems in actual CCUS systems have several objectives: minimizing total allocating cost; maximizing quality of products; maximizing probability of finishing the processes by deadline etc. Tavana et al. proposed a multi-objective optimization problem for project scheduling, where task

durations are fixed values.¹⁶⁷ To my knowledge, the multi-objective optimization problem with stochastic task durations expressed as discrete distributions has not been proposed.

Chapter 5 Conclusions

In this thesis, I have proposed and demonstrated the following two approaches to improve the design and operation methods for CCUS systems. In Chapters 2 and 3, many potential advantages are quantified for a flexible MOF in a CO₂ adsorption process using a rigorous process model. One of the most promising flexible MOFs, ELM-11, was considered in our case studies to evaluate the performance indicators, such as purity, recovery, BSF, and power consumption. An isothermal model of ELM-11 was proposed to develop a mathematical model based on the adsorption data, and the parameters are estimated by a least-squares method. The isotherm model was integrated within a dynamic VPSA process model employing a simple 4-step cycle without rinse and purge operations to estimate the performance indicators.

The results found that CO₂ purity is always high because of the high selectivity of ELM-11. To improve the recovery rate, increasing the feed pressure and lowering the operating temperature can overcome the slipping-off problem known in flexible MOFs. In addition, a formula to estimate recovery was proposed from the feed and foot CO₂ pressures without performing simulations, which will be useful also for other flexible MOFs that show sigmoidal adsorption isotherms. The relationship between power consumption and operating temperature was also investigated. For a given recovery rate, lowering the operating temperature lowers the power consumption by the compressor but increases the power consumption of the vacuum pump. Under this trade-off relationship, it was found that the low-temperature operation of 263 K to 273 K minimizes the sum of the two sources of power

consumption. However, careful consideration must also be given to cooling energy in the sub-ambient operations to find the optimal operation.

The advantages of ELM-11 were also confirmed through a comparison with zeolite 13X. The higher CO₂/N₂ selectivity of ELM-11 provides a significantly higher purity. Furthermore, the BSF of ELM-11 can be substantially smaller than that of zeolite 13X because of the larger working capacity and higher mass transfer rate based on the LDF model. The high product purity, throughput, and energy efficiency found in this study will pave the way for demonstration of large-scale CO₂ separation. The promising properties of flexible MOFs over zeolites revealed in this study also encourage future research on other practical applications of this material such as hydrocarbon separations.¹⁶⁸

In Chapter 4, I extended the conventional CPM to apply the RCPS method to schedule CCUS systems with uncertain task durations. The proposed method uses histograms obtained from historical operation data to represent the task durations. The formulation is MILP, which has the advantage of guaranteeing an optimal solution in the search range by using the branch-and-bound method. I proposed three formulations with trade-offs between computation time, cost allocation flexibility, and solution accuracy. *TOF* has more ways to improve the processing time with cost allocation than the conventional CPM and can propose flexible ways of cost allocation. However, this formulation requires a decision variable for every combination of the histograms of task durations, which makes the problem large; in Example 2, the system had 2,469,614 decision variables for 7 tasks. The formulation (*POF, Strict*) significantly reduces the number of decision variables compared to *TOF*,

instead of limiting the ways of cost allocation. In the example, the number of decision variables in *POF* is 14,307, which is 1/173 of that of *TOF*. The formulation (*POF, Local Search*) further reduces the number of decision variables by applying the local search method to (*POF, Strict*). In the example, the number of decision variables in (*POF, Local Search*) is 132, which is 1/18,700 of that of *TOF*. This method requires less computation time, but the optimal solution is not guaranteed depending on the range of the local search.

Nomenclature

Notations for Chapter 2 and 3

b_L	imaginary adsorption isotherm parameter for CO ₂ [molCO ₂ /(kg _{ads} ·kPa)]
b_U	temperature-dependent value for imaginary CO ₂ adsorption isotherm [kPa ⁻¹]
b_U^∞	imaginary adsorption isotherm parameter for CO ₂ [kPa ⁻¹]
b_H	imaginary adsorption isotherm parameter for CO ₂ [molCO ₂ /(kg _{ads} ·kPa)]
b_{N_2}	temperature-independent adsorption isotherm parameter for N ₂ [molN ₂ /(kg _{ads} ·kPa)]
C_{pg}	heat capacity of gas [J/(kg·K)]
C_{ps}	heat capacity of solid [J/(kg·K)]
D_L	axial dispersion coefficient [m ² /s]
E_U	imaginary adsorption isotherm parameter for CO ₂ [kJ/molCO ₂]
feed	amount of CO ₂ feed gas [molCO ₂]
h	heat transfer coefficient [J/(m ² ·s·K)]
$H_{\text{step},j}$	enthalpy of the phase transitions [kJ/molCO ₂]
i	component
impurity	amount of N ₂ gas in the product [molN ₂]
j	mode of hysteretic isotherms
k_i	overall mass transfer coefficient of component i [1/s]
K_L	axial thermal conductivity [J/(m·s·K)]

L	column length [m]
m_{ads}	weight of adsorbent packed in the column without binder [kg], ($m_{\text{ads}} = \rho_{\text{ads}} R_{\text{bed}}^2 \pi L$)
$M_{w_{\text{CO}_2}}$	molecular weight of CO ₂ [g/molCO ₂]
mode	binary variable for mode of hysteretic isotherms [-]
n_L	imaginary adsorption isotherm where the gate is always close [molCO ₂ /kg _{ads}]
n_U	imaginary adsorption isotherm where the gate is always open [molCO ₂ /kg _{ads}]
n_j	adsorption/desorption isotherms of CO ₂ [mol/kg _{ads}]
n_U^∞	saturated amount of CO ₂ adsorption [molCO ₂ /kg _{ads}]
$n_{\text{des} \rightarrow \text{ads}}$	secondary or higher-order adsorption isotherm [molCO ₂ /kg _{ads}]
$n_{\text{ads} \rightarrow \text{des}}$	secondary or higher-order desorption isotherm [molCO ₂ /kg _{ads}]
n_{sat}	saturated amount of CO ₂ adsorption [molCO ₂ /kg _{ads}]
n_{switch}	amount of CO ₂ adsorbed at switched point [molCO ₂ /kg _{ads}]
p_{CO_2}	partial pressure of CO ₂ [kPa]
p_{N_2}	partial pressure of N ₂ [kPa]
$p_{\text{feed},i}$	feed partial pressure of component i [kPa]
$p_{\text{CO}_2,\text{tar}}$	target partial pressure of CO ₂ during adsorption step [kPa]
$p_{\text{step},j}$	step pressure of isotherm j [kPa]
$p_{\text{step}0,j}$	step pressure of isotherm j at reference temperature [kPa]
$p_{\text{foot,ads}}$	foot CO ₂ pressure for adsorption isotherm at reference temperature [kPa]

$p_{\text{foot,des}}$	foot CO ₂ pressure for adsorption isotherm at reference temperature [kPa]
P_{atm}	atmospheric pressure [kPa]
P_{des}	desorption pressure [kPa]
P_{feed}	feed gas pressure [kPa]
$\text{Power}_{\text{compressor}}$	electrical power consumption for the compressor [kW]
$\text{Power}_{\text{vacuum}}$	electrical power consumption for the vacuum pump [kW]
product	amount of CO ₂ product in one cycle at a cyclic steady state [molCO ₂]
q_i	amount of component i adsorbed [mol/kg _{ads}]
q_i^*	equilibrium amount of component i adsorbed [mol/kg _{ads}]
$q_{\text{CO}_2,\text{tar}}$	target amount of CO ₂ adsorbed during desorption step [molCO ₂ /kg _{ads}]
$q_{\text{eq,ads}}$	equilibrium amount of CO ₂ adsorbed during adsorption step [molCO ₂ /kg _{ads}]
$q_{\text{eq,des}}$	equilibrium amount of CO ₂ adsorbed during desorption step [molCO ₂ /kg _{ads}]
Q_{outlet}	molar flow rate at the outlet [mol/s]
r_d	desorption ratio [-]
R	gas constant [J/(mol·K)]
R_p	particle radius [m]
R_{bed}	bed radius [m]
t	time since each cycle started [s]
t_{press}	pressurization time [s]

t_{ads}	adsorption time [s]
t_{depress}	depressurization time [s]
t_{des}	desorption time [s]
t_{trans}	transition time from atmospheric pressure to desorption pressure [s], which is used to design a pressure boundary condition in Step 4 (see Table 3-4).
t_{cycle}	cycle time [s]
T	temperature [K]
T_0	reference temperature [K]
T_{amb}	ambient temperature [K]
T_{feed}	feed temperature [K]
T_{wall}	column wall temperature [K]
u	gas velocity [m/s]
u_{outlet}	gas velocity at the outlet [m/s]
w_j	weighting function [-]
$y_{i,\text{feed}}$	feed mole fraction of component i [-]
z	axial position in column [m]
v_j	weighting function parameter [-]
χ_j	parameter for the weighting function w_j [-]
ε_{bed}	bed void [-]

ε_T	tolerance for temperature [K ²]
ε_y	tolerance for mole fraction [-]
ε_q	tolerance for adsorption amount [(mol/kg _{ads}) ²]
ρ_{ads}	adsorbent density without binder [kg _{ads} /m ³]
ρ_{pellet}	pellet density [kg/m ³]
ρ_{wall}	wall density [kg/m ³]
μ	gas viscosity [kg/(m·s)]
$\eta_{\text{compressor}}$	efficiency of compressor [-]
η_{vacuum}	efficiency of vacuum pump [-]
γ	heat capacity ratio [-]

Notations for Chapter 4

INDICES

s	Source task
e	Sink task
i	Task
j	Path from source to sink
k_i	Index of random variable $t_i^{(k_i)}$
v_j	Index of random variable $T^{(v_j)}$
k_i'	Realization of integer k_i
v_j'	Realization of integer v_j
$v_{j\text{crit}}$	Realization of integer v_j that satisfies Eq.(4-28)
v_j^*	Realization of integer v_j that corresponds to the optimal solution of <i>Path-Oriented Formulation</i> proposing in Section 4.5
v_j^{ref}	Realization of integer v_j for local search method in Section 4.6

SETS

W	Set of tasks except for source and sink
V	Set of paths
p_j	Set of tasks on path j except for dummy tasks
A	Set of realizations for $k_i, i \in W$

M Set of realizations for $v_j, j \in V$

\bar{M}_j Set of realizations for the local search method

E Set of arcs in process network

$H^{(v_1, v_2, \dots, v_r)}$ Set that includes all (k_1, k_2, \dots, k_n) satisfying condition $\sum_{i \in p_j} t_i^{(k_i)} \leq T_j^{(v_j)}, j \in V$

$\bar{H}^{(v_1, v_2, \dots, v_r)}$ Set that includes all (k_1, k_2, \dots, k_n) satisfying condition $\sum_{i \in p_j} t_i^{(k_i)} \leq T_j^{(v_j)}, j \in V$ for the local search method

PARAMETERS

n Number of tasks

r Number of paths

c_i^U Crash cost of task i

\mathbf{c}^U Vector of the crash cost of task i

C Maximum total cost

Γ Target process completion time

$\alpha_i^{(k_i)}$ Probability in bin k_i

$N_i[t_i^{(k_i)}]$ Number of samples within $t_i^{(k_{i-1})} < t_i \leq t_i^{(k_i)}$

Γ Target process completion time

λ_i Proportionality constant for reducing duration of task i per additional cost in classical CPM formulation

$\lambda_{M,i}$	Proportionality constant for reducing expected value of duration of task i per additional cost in proposing formulations
$\lambda_{D,i}$	Proportionality constant for dispersion of duration of task i per additional cost in proposing formulations
t_i^{ave}	Average duration of task i without improvement
$t_i^{(k_i)}$	Duration of task i without improvement in discretized form
$T^{(v_j)}$	Discretized time
$h^{(v_1, v_2, \dots, v_r)}$	Probability that sum of task durations $\sum_{i \in p_j} t_i^{(k_i)}$ is smaller than $T_j^{(v_j)}$ for all paths, $j \in V$
β	Search range in the local search method
$c_{M,i}^{\text{ref}}$	Realization of allocating cost on task i for the local search method as a reference value
$c_{M,i}^*$	Optimal value of $c_{M,i}$ of the <i>Path-Oriented Formulation</i> in Section 4.5
a	Bin width for histograms in case studies

References

- (1) Hoegh-Guldberg, O.; Jacob, D.; Taylor, M.; Guillén Bolaños, T.; Bindi, M.; Brown, S.; Camilloni, I. A.; Diedhiou, A.; Djalante, R.; Ebi, K. The Human Imperative of Stabilizing Global Climate Change at 1.5 °C. *Science* (80-.). **2019**, *365* (6459), eaaw6974.
- (2) Tollefson, J. IPCC Says Limiting Global Warming to 1.5 °C Will Require Drastic Action. *Nature* **2018**, *562* (7726), 172–174.
- (3) Masson-Delmotte, V.; Zhai, P.; Pörtner, H.-O.; Roberts, D.; Skea, J.; Shukla, P. R.; Pirani, A.; Moufouma-Okia, W.; Péan, C.; Pidcock, R. Global Warming of 1.5 °C. *An IPCC Spec. Rep. impacts Glob. Warm.* **2018**, *1* (5).
- (4) *Redrawing the Energy-Climate Map: World Energy Outlook Special Report*; OECD/IEA, 2013.
- (5) Beck, J. H. Efficient Targeted Optimisation for the Design of Pressure Swing Adsorption Systems for CO₂ Capture in Power Plants, UCL (University College London), 2014.
- (6) Metz, B.; Davidson, O.; De Coninck, H. C.; Loos, M.; Meyer, L. *IPCC Special Report on Carbon Dioxide Capture and Storage*; Cambridge: Cambridge University Press, 2005.
- (7) Aaron, D.; Tsouris, C. Separation of CO₂ from Flue Gas: A Review. *Sep. Sci. Technol.* **2005**, *40* (1–3), 321–348. <https://doi.org/10.1081/SS-200042244>.
- (8) Katzer, J.; Moniz, E. J.; Deutch, J.; Ansolabehere, S.; Beer, J. *The Future of Coal: An Interdisciplinary MIT Study*; Technical report, Massachusetts Institute of Technology,

Cambridge, MA, 2007.

- (9) Jansen, D.; Gazzani, M.; Manzolini, G.; van Dijk, E.; Carbo, M. Pre-Combustion CO₂ Capture. *Int. J. Greenh. Gas Control* **2015**, *40*, 167–187.
- (10) Stanger, R.; Wall, T.; Spörl, R.; Paneru, M.; Grathwohl, S.; Weidmann, M.; Scheffknecht, G.; McDonald, D.; Myöhänen, K.; Ritvanen, J. Oxyfuel Combustion for CO₂ Capture in Power Plants. *Int. J. Greenh. gas Control* **2015**, *40*, 55–125.
- (11) Choi, S.; Drese, J. H.; Jones, C. W. Adsorbent Materials for Carbon Dioxide Capture from Large Anthropogenic Point Sources. *ChemSusChem Chem. Sustain. Energy Mater.* **2009**, *2* (9), 796–854.
- (12) Hedin, N.; Andersson, L.; Bergström, L.; Yan, J. Adsorbents for the Post-Combustion Capture of CO₂ Using Rapid Temperature Swing or Vacuum Swing Adsorption. *Appl. Energy* **2013**, *104*, 418–433. <https://doi.org/10.1016/j.apenergy.2012.11.034>.
- (13) Liu, W.; King, D.; Liu, J.; Johnson, B.; Wang, Y.; Yang, Z. Critical Material and Process Issues for CO₂ Separation from Coal-Powered Plants. *Jom* **2009**, *61* (4), 36–44.
- (14) Ebner, A. D.; Ritter, J. A. State-of-the-Art Adsorption and Membrane Separation Processes for Carbon Dioxide Production from Carbon Dioxide Emitting Industries. *Sep. Sci. Technol.* **2009**, *44* (6), 1273–1421.
- (15) Machida, H.; Oba, K.; Tomikawa, T.; Esaki, T.; Yamaguchi, T.; Horizoe, H. Development of Phase Separation Solvent for CO₂ Capture by Aqueous (Amine+ether) Solution. *J. Chem.*

- Thermodyn.* **2017**, *113*, 64–70. <https://doi.org/https://doi.org/10.1016/j.jct.2017.05.043>.
- (16) Hung, Y.-C.; Hsieh, C.-M.; Machida, H.; Lin, S.-T.; Shimoyama, Y. Modeling of Phase Separation Solvent for CO₂ Capture Using COSMO-SAC Model. *J. Taiwan Inst. Chem. Eng.* **2022**, *135*, 104362. <https://doi.org/https://doi.org/10.1016/j.jtice.2022.104362>.
- (17) Inagaki, F.; Matsumoto, C.; Iwata, T.; Mukai, C. CO₂-Selective Absorbents in Air: Reverse Lipid Bilayer Structure Forming Neutral Carbamic Acid in Water without Hydration. *J. Am. Chem. Soc.* **2017**, *139* (13), 4639–4642. <https://doi.org/10.1021/jacs.7b01049>.
- (18) Riboldi, L. Assessment of Pressure Swing Adsorption as CO₂ Capture Technology in Coal-Fired Power Plants, NTNU, 2016.
- (19) Budd, P. M.; McKeown, N. B. Highly Permeable Polymers for Gas Separation Membranes. *Polym. Chem.* **2010**, *1* (1), 63–68.
- (20) Merkel, T. C.; Lin, H.; Wei, X.; Baker, R. Power Plant Post-Combustion Carbon Dioxide Capture: An Opportunity for Membranes. *J. Memb. Sci.* **2010**, *359* (1–2), 126–139.
- (21) Figueroa, J. D.; Fout, T.; Plasynski, S.; McIlvried, H.; Srivastava, R. D. Advances in CO₂ Capture Technology—the US Department of Energy’s Carbon Sequestration Program. *Int. J. Greenh. gas Control* **2008**, *2* (1), 9–20.
- (22) Al-Mamoori, A.; Krishnamurthy, A.; Rownaghi, A. A.; Rezaei, F. Carbon Capture and Utilization Update. *Energy Technol.* **2017**, *5* (6), 834–849.
- (23) Ruthven, D. M.; Pressure, F. Pressure Swing Adsorption. *New York VCH Publ.* **1994**, *1* (994),

235.

- (24) Ho, M. T.; Allinson, G. W.; Wiley, D. E. Reducing the Cost of CO₂ Capture from Flue Gases Using Pressure Swing Adsorption. *Ind. Eng. Chem. Res.* **2008**, *47* (14), 4883–4890.
- (25) Sircar, S. Basic Research Needs for Design of Adsorptive Gas Separation Processes. *Ind. Eng. Chem. Res.* **2006**, *45* (16), 5435–5448.
- (26) Agarwal, A.; Biegler, L. T.; Zitney, S. E. Superstructure-Based Optimal Synthesis of Pressure Swing Adsorption Cycles for Precombustion CO₂ Capture. *Ind. Eng. Chem. Res.* **2010**, *49* (11), 5066–5079.
- (27) Agarwal, A.; Biegler, L. T.; Zitney, S. E. A Superstructure-based Optimal Synthesis of PSA Cycles for Post-combustion CO₂ Capture. *AIChE J.* **2010**, *56* (7), 1813–1828.
- (28) Sinha, A.; Darunte, L. A.; Jones, C. W.; Realff, M. J.; Kawajiri, Y. Systems Design and Economic Analysis of Direct Air Capture of CO₂ through Temperature Vacuum Swing Adsorption Using MIL-101(Cr)-PEI-800 and Mmen-Mg₂(Dobpdc) MOF Adsorbents. *Ind. Eng. Chem. Res.* **2017**, *56* (3), 750–764. <https://doi.org/10.1021/acs.iecr.6b03887>.
- (29) Abanades, J. C.; Arias, B.; Lyngfelt, A.; Mattisson, T.; Wiley, D. E.; Li, H.; Ho, M. T.; Mangano, E.; Brandani, S. Emerging CO₂ Capture Systems. *Int. J. Greenh. Gas Control* **2015**, *40*, 126–166.
- (30) Shen, C.; Yu, J.; Li, P.; Grande, C. A.; Rodrigues, A. E. Capture of CO₂ from Flue Gas by Vacuum Pressure Swing Adsorption Using Activated Carbon Beads. *Adsorption* **2011**, *17* (1),

179–188. <https://doi.org/10.1007/s10450-010-9298-y>.

- (31) Zhao, R.; Zhao, L.; Deng, S.; Song, C.; He, J.; Shao, Y.; Li, S. A Comparative Study on CO₂ Capture Performance of Vacuum-Pressure Swing Adsorption and Pressure-Temperature Swing Adsorption Based on Carbon Pump Cycle. *Energy* **2017**, *137*, 495–509. <https://doi.org/10.1016/j.energy.2017.01.158>.
- (32) Tian, J.; Shen, Y.; Zhang, D.; Tang, Z. CO₂ Capture by Vacuum Pressure Swing Adsorption from Dry Flue Gas with a Structured Composite Adsorption Medium. *J. Environ. Chem. Eng.* **2021**, *9* (5), 106037. <https://doi.org/10.1016/j.jece.2021.106037>.
- (33) Qasem, N. A. A.; Ben-Mansour, R. Energy and Productivity Efficient Vacuum Pressure Swing Adsorption Process to Separate CO₂ from CO₂/N₂ Mixture Using Mg-MOF-74: A CFD Simulation. *Appl. Energy* **2018**, *209*, 190–202. <https://doi.org/10.1016/j.apenergy.2017.10.098>.
- (34) Xu, M.; Chen, S.; Seo, D.-K.; Deng, S. Evaluation and Optimization of VPSA Processes with Nanostructured Zeolite NaX for Post-Combustion CO₂ Capture. *Chem. Eng. J.* **2019**, *371*, 693–705. <https://doi.org/10.1016/j.cej.2019.03.275>.
- (35) Ko, D.; Siriwardane, R.; Biegler, L. T. Optimization of Pressure Swing Adsorption and Fractionated Vacuum Pressure Swing Adsorption Processes for CO₂ Capture. *Ind. Eng. Chem. Res.* **2005**, *44* (21), 8084–8094. <https://doi.org/10.1021/ie050012z>.
- (36) Shen, C.; Liu, Z.; Li, P.; Yu, J. Two-Stage VPSA Process for CO₂ Capture from Flue Gas

Using Activated Carbon Beads. *Ind. Eng. Chem. Res.* **2012**, *51* (13), 5011–5021.

<https://doi.org/10.1021/ie202097y>.

- (37) Luberti, M.; Friedrich, D.; Brandani, S.; Ahn, H. Design of a H₂ PSA for Cogeneration of Ultrapure Hydrogen and Power at an Advanced Integrated Gasification Combined Cycle with Pre-Combustion Capture. *Adsorption* **2014**, *20* (2), 511–524.
- (38) Ahn, S.; You, Y.-W.; Lee, D.-G.; Kim, K.-H.; Oh, M.; Lee, C.-H. Layered Two-and Four-Bed PSA Processes for H₂ Recovery from Coal Gas. *Chem. Eng. Sci.* **2012**, *68* (1), 413–423.
- (39) Wang, Q.; Luo, J.; Zhong, Z.; Borgna, A. CO₂ Capture by Solid Adsorbents and Their Applications: Current Status and New Trends. *Energy Environ. Sci.* **2011**, *4* (1), 42–55.
- (40) Cinke, M.; Li, J.; Bauschlicher, C. W.; Ricca, A.; Meyyappan, M. CO₂ Adsorption in Single-Walled Carbon Nanotubes. *Chem. Phys. Lett.* **2003**, *376* (5), 761–766.
- [https://doi.org/https://doi.org/10.1016/S0009-2614\(03\)01124-2](https://doi.org/https://doi.org/10.1016/S0009-2614(03)01124-2).
- (41) Hsu, S.-C.; Lu, C.; Su, F.; Zeng, W.; Chen, W. Thermodynamics and Regeneration Studies of CO₂ Adsorption on Multiwalled Carbon Nanotubes. *Chem. Eng. Sci.* **2010**, *65* (4), 1354–1361.
- <https://doi.org/https://doi.org/10.1016/j.ces.2009.10.005>.
- (42) Lu, C.; Bai, H.; Wu, B.; Su, F.; Hwang, J. F. Comparative Study of CO₂ Capture by Carbon Nanotubes, Activated Carbons, and Zeolites. *Energy & Fuels* **2008**, *22* (5), 3050–3056.
- <https://doi.org/10.1021/ef8000086>.
- (43) Saha, D.; Deng, S. Adsorption Equilibrium and Kinetics of CO₂, CH₄, N₂O, and NH₃ on

Ordered Mesoporous Carbon. *J. Colloid Interface Sci.* **2010**, *345* (2), 402–409.

<https://doi.org/https://doi.org/10.1016/j.jcis.2010.01.076>.

- (44) Yakovlev, V. Y.; Fomkin, A. A.; Tvardovski, A. V. Adsorption and Deformation Phenomena at the Interaction of CO₂ and a Microporous Carbon Adsorbent. *J. Colloid Interface Sci.* **2003**, *268* (1), 33–36. [https://doi.org/https://doi.org/10.1016/S0021-9797\(03\)00696-9](https://doi.org/https://doi.org/10.1016/S0021-9797(03)00696-9).
- (45) Zhao, D.; Cleare, K.; Oliver, C.; Ingram, C.; Cook, D.; Szostak, R.; Kevan, L. Characteristics of the Synthetic Heulandite-Clinoptilolite Family of Zeolites. *Microporous Mesoporous Mater.* **1998**, *21* (4), 371–379. [https://doi.org/https://doi.org/10.1016/S1387-1811\(98\)00131-0](https://doi.org/https://doi.org/10.1016/S1387-1811(98)00131-0).
- (46) Jacobs, P. A.; van Cauwelaert, F. H.; Vansant, E. F.; Uytterhoeven, J. B. Surface Probing of Synthetic Faujasites by Adsorption of Carbon Dioxide. Part 1.—Infra-Red Study of Carbon Dioxide Adsorbed on Na-Ca-Y and Na-Mg-Y Zeolites. *J. Chem. Soc. Faraday Trans. 1 Phys. Chem. Condens. Phases* **1973**, *69*, 1056–1068.
- (47) Montanari, T.; Busca, G. On the Mechanism of Adsorption and Separation of CO₂ on LTA Zeolites: An IR Investigation. *Vib. Spectrosc.* **2008**, *46* (1), 45–51.
<https://doi.org/https://doi.org/10.1016/j.vibspec.2007.09.001>.
- (48) Hernández-Huesca, R.; Díaz, L.; Aguilar-Armenta, G. Adsorption Equilibria and Kinetics of CO₂, CH₄ and N₂ in Natural Zeolites. *Sep. Purif. Technol.* **1999**, *15* (2), 163–173.
[https://doi.org/https://doi.org/10.1016/S1383-5866\(98\)00094-X](https://doi.org/https://doi.org/10.1016/S1383-5866(98)00094-X).
- (49) Inui, T.; Okugawa, Y.; Yasuda, M. Relationship between Properties of Various Zeolites and

Their Carbon Dioxide Adsorption Behaviors in Pressure Swing Adsorption Operation. *Ind.*

Eng. Chem. Res. **1988**, 27 (7), 1103–1109.

- (50) Krishnamurthy, S.; Rao, V. R.; Guntuka, S.; Sharratt, P.; Haghpanah, R.; Rajendran, A.; Amanullah, M.; Karimi, I. A.; Farooq, S. CO₂ Capture from Dry Flue Gas by Vacuum Swing Adsorption: A Pilot Plant Study. *AIChE J.* **2014**, 60 (5), 1830–1842.
<https://doi.org/10.1002/aic.14435>.
- (51) Hack, J.; Maeda, N.; Meier, D. M. Review on CO₂ Capture Using Amine-Functionalized Materials. *ACS omega* **2022**, 7 (44), 39520–39530.
- (52) Cogswell, C. F.; Xie, Z.; Wolek, A.; Wang, Y.; Stavola, A.; Finkenaur, M.; Gilmore, E.; Lanzillotti, M.; Choi, S. Pore Structure–CO₂ Adsorption Property Relations of Supported Amine Materials with Multi-Pore Networks. *J. Mater. Chem. A* **2017**, 5 (18), 8526–8536.
- (53) Geng, J.; Xue, D.; Liu, X.; Shi, Y.; Sun, L. N-doped Porous Carbons for CO₂ Capture: Rational Choice of N-containing Polymer with High Phenyl Density as Precursor. *AIChE J.* **2017**, 63 (5), 1648–1658.
- (54) Qi, S.-C.; Wu, J.-K.; Lu, J.; Yu, G.-X.; Zhu, R.-R.; Liu, Y.; Liu, X.-Q.; Sun, L.-B. Underlying Mechanism of CO₂ Adsorption onto Conjugated Azacyclo-Copolymers: N-Doped Adsorbents Capture CO₂ Chiefly through Acid–Base Interaction? *J. Mater. Chem. A* **2019**, 7 (30), 17842–17853.
- (55) Flaig, R. W.; Osborn Popp, T. M.; Fracaroli, A. M.; Kapustin, E. A.; Kalmutzki, M. J.;

- Altamimi, R. M.; Fathieh, F.; Reimer, J. A.; Yaghi, O. M. The Chemistry of CO₂ Capture in an Amine-Functionalized Metal–Organic Framework under Dry and Humid Conditions. *J. Am. Chem. Soc.* **2017**, *139* (35), 12125–12128.
- (56) Fracaroli, A. M.; Furukawa, H.; Suzuki, M.; Dodd, M.; Okajima, S.; Gándara, F.; Reimer, J. A.; Yaghi, O. M. Metal–Organic Frameworks with Precisely Designed Interior for Carbon Dioxide Capture in the Presence of Water. *J. Am. Chem. Soc.* **2014**, *136* (25), 8863–8866.
- (57) Zhang, H.; Goeppert, A.; Olah, G. A.; Prakash, G. K. S. Remarkable Effect of Moisture on the CO₂ Adsorption of Nano-Silica Supported Linear and Branched Polyethylenimine. *J. CO₂ Util.* **2017**, *19*, 91–99.
- (58) Weissnar, F.; Gau, A.; Hack, J.; Maeda, N.; Meier, D. M. Toward Carbon Dioxide Capture from the Atmosphere: Lowering the Regeneration Temperature of Polyethylenimine-Based Adsorbents by Ionic Liquid. *Energy & Fuels* **2021**, *35* (10), 9059–9062.
- (59) Bae, Y.; Snurr, R. Q. Development and Evaluation of Porous Materials for Carbon Dioxide Separation and Capture. *Angew. Chemie Int. Ed.* **2011**, *50* (49), 11586–11596.
- (60) D’Alessandro, D. M.; Smit, B.; Long, J. R. Carbon Dioxide Capture: Prospects for New Materials. *Angew. Chemie Int. Ed.* **2010**, *49* (35), 6058–6082.
- (61) Kitagawa, S.; Kitaura, R.; Noro, S. Functional Porous Coordination Polymers. *Angew. Chemie Int. Ed.* **2004**, *43* (18), 2334–2375.
- (62) Ruben, M.; Rojo, J.; Romero-Salguero, F. J.; Uppadine, L. H.; Lehn, J. Grid-type Metal Ion

- Architectures: Functional Metallosupramolecular Arrays. *Angew. Chemie Int. Ed.* **2004**, *43* (28), 3644–3662.
- (63) Majchrzak-Kucęba, I.; Wawrzyńczak, D.; Ściubidło, A. Application of Metal–Organic Frameworks in VPSA Technology for CO₂ Capture. *Fuel* **2019**, *255*, 115773.
<https://doi.org/10.1016/j.fuel.2019.115773>.
- (64) Horike, S.; Shimomura, S.; Kitagawa, S. Soft Porous Crystals. *Nat. Chem.* **2009**, *1* (9), 695–704. <https://doi.org/10.1038/nchem.444>.
- (65) Schneemann, A.; Bon, V.; Schwedler, I.; Senkovska, I.; Kaskel, S.; Fischer, R. A. Flexible Metal–Organic Frameworks. *Chem. Soc. Rev.* **2014**, *43* (16), 6062–6096.
<https://doi.org/10.1039/C4CS00101J>.
- (66) Coudert, F.-X.; Boutin, A.; Fuchs, A. H.; Neimark, A. V. Adsorption Deformation and Structural Transitions in Metal–Organic Frameworks: From the Unit Cell to the Crystal. *J. Phys. Chem. Lett.* **2013**, *4* (19), 3198–3205. <https://doi.org/10.1021/jz4013849>.
- (67) Hiraide, S.; Tanaka, H.; Ishikawa, N.; Miyahara, M. T. Intrinsic Thermal Management Capabilities of Flexible Metal – Organic Frameworks for Carbon Dioxide Separation and Capture. *ACS Appl. Mater. Interfaces* **2017**, *9* (46), 41066–41077.
<https://doi.org/10.1021/acsami.7b13771>.
- (68) Mason, J. A.; Oktawiec, J.; Taylor, M. K.; Hudson, M. R.; Rodriguez, J.; Bachman, J. E.; Gonzalez, M. I.; Cervellino, A.; Guagliardi, A.; Brown, C. M.; Llewellyn, P. L.; Masciocchi,

N.; Long, J. R. Methane Storage in Flexible Metal–Organic Frameworks with Intrinsic Thermal Management. *Nature* **2015**, *527* (7578), 357–361.

<https://doi.org/10.1038/nature15732>.

(69) Li, D.; Kaneko, K. Hydrogen Bond-Regulated Microporous Nature of Copper Complex-Assembled Microcrystals. *Chem. Phys. Lett.* **2001**, *335* (1–2), 50–56.

[https://doi.org/10.1016/S0009-2614\(00\)01419-6](https://doi.org/10.1016/S0009-2614(00)01419-6).

(70) Yang, J.; Yu, Q.; Zhao, Q.; Liang, J.; Dong, J.; Li, J. Adsorption CO₂, CH₄ and N₂ on Two Different Spacing Flexible Layer MOFs. *Microporous Mesoporous Mater.* **2012**, *161*, 154–159. <https://doi.org/10.1016/j.micromeso.2012.01.008>.

(71) Tanaka, H.; Hiraide, S.; Kondo, A.; Miyahara, M. T. Modeling and Visualization of CO₂ Adsorption on Elastic Layer-Structured Metal–Organic Framework-11: Toward a Better Understanding of Gate Adsorption Behavior. *J. Phys. Chem. C* **2015**, *119* (21), 11533–11543.

<https://doi.org/10.1021/jp512870p>.

(72) Hiraide, S.; Tanaka, H.; Miyahara, M. T. Understanding Gate Adsorption Behaviour of CO₂ on Elastic Layer-Structured Metal–Organic Framework-11. *Dalt. Trans.* **2016**, *45* (10), 4193–4202. <https://doi.org/10.1039/C5DT03476K>.

(73) Bon, V.; Kavooosi, N.; Senkovska, I.; Kaskel, S. Tolerance of Flexible MOFs toward Repeated Adsorption Stress. *ACS Appl. Mater. Interfaces* **2015**, *7* (40), 22292–22300.

<https://doi.org/10.1021/acsami.5b05456>.

- (74) Kultaeva, A.; Bon, V.; Weiss, M. S.; Pöppl, A.; Kaskel, S. Elucidating the Formation and Transformation Mechanisms of the Switchable Metal–Organic Framework ELM-11 by Powder and Single-Crystal EPR Study. *Inorg. Chem.* **2018**, *57* (19), 11920–11929. <https://doi.org/10.1021/acs.inorgchem.8b01241>.
- (75) Kondo, A.; Noguchi, H.; Ohnishi, S.; Kajiro, H.; Tohdoh, A.; Hattori, Y.; Xu, W.-C.; Tanaka, H.; Kanoh, H.; Kaneko, K. Novel Expansion/Shrinkage Modulation of 2D Layered MOF Triggered by Clathrate Formation with CO₂ Molecules. *Nano Lett.* **2006**, *6* (11), 2581–2584. <https://doi.org/10.1021/nl062032b>.
- (76) Sotomayor, F. J.; Lastoskie, C. M. Predicting the Breakthrough Performance of “Gating” Adsorbents Using Osmotic Framework-Adsorbed Solution Theory. *Langmuir* **2017**, *33* (42), 11670–11678. <https://doi.org/10.1021/acs.langmuir.7b02036>.
- (77) Horike, S.; Inubushi, Y.; Hori, T.; Fukushima, T.; Kitagawa, S. A Solid Solution Approach to 2D Coordination Polymers for CH₄/CO₂ and CH₄/C₂H₆ Gas Separation: Equilibrium and Kinetic Studies. *Chem. Sci.* **2012**, *3* (1), 116–120. <https://doi.org/10.1039/C1SC00591J>.
- (78) Hiraide, S.; Sakanaka, Y.; Kajiro, H.; Kawaguchi, S.; Miyahara, M. T.; Tanaka, H. High-Throughput Gas Separation by Flexible Metal–Organic Frameworks with Fast Gating and Thermal Management Capabilities. *Nat. Commun.* **2020**, *11* (1), 3867. <https://doi.org/10.1038/s41467-020-17625-3>.
- (79) Bon, V.; Senkowska, I.; Wallacher, D.; Heerwig, A.; Klein, N.; Zizak, I.; Feyerherm, R.;

Dudzik, E.; Kaskel, S. In Situ Monitoring of Structural Changes during the Adsorption on Flexible Porous Coordination Polymers by X-Ray Powder Diffraction: Instrumentation and Experimental Results. *Microporous Mesoporous Mater.* **2014**, *188*, 190–195.

<https://doi.org/10.1016/j.micromeso.2013.12.024>.

- (80) Ichikawa, M.; Kondo, A.; Noguchi, H.; Kojima, N.; Ohba, T.; Kajiro, H.; Hattori, Y.; Kanoh, H. Double-Step Gate Phenomenon in CO₂ Sorption of an Elastic Layer-Structured MOF.

Langmuir **2016**, *32* (38), 9722–9726. <https://doi.org/10.1021/acs.langmuir.6b02551>.

- (81) Takakura, Y.; Sugimoto, S.; Fujiki, J.; Kajiro, H.; Yajima, T.; Kawajiri, Y. Model-Based Analysis of a Highly Efficient CO₂ Separation Process Using Flexible Metal–Organic Frameworks with Isotherm Hysteresis. *ACS Sustain. Chem. Eng.* **2022**, *10* (45), 14935–14947.

- (82) Remy, T.; Baron, G. V.; Denayer, J. F. M. Modeling the Effect of Structural Changes during Dynamic Separation Processes on MOFs. *Langmuir* **2011**, *27* (21), 13064–13071.

<https://doi.org/10.1021/la203374a>.

- (83) Hefti, M.; Joss, L.; Bjelobrk, Z.; Mazzotti, M. On the Potential of Phase-Change Adsorbents for CO₂ Capture by Temperature Swing Adsorption. *Faraday Discuss.* **2016**, *192*, 153–179.

<https://doi.org/10.1039/c6fd00040a>.

- (84) Štěpánek, F.; Kubíček, M.; Marek, M.; Šoóš, M.; Rajniak, P.; Yang, R. T. On the Modeling of PSA Cycles with Hysteresis-Dependent Isotherms. *Chem. Eng. Sci.* **2000**, *55* (2), 431–440.

[https://doi.org/10.1016/S0009-2509\(99\)00338-3](https://doi.org/10.1016/S0009-2509(99)00338-3).

- (85) Hefti, M.; Mazzotti, M. Modeling Water Vapor Adsorption/Desorption Cycles. *Adsorption* **2014**, *20* (2–3), 359–371. <https://doi.org/10.1007/s10450-013-9573-9>.
- (86) Wang, Y.; An, Y.; Ding, Z.; Shen, Y.; Tang, Z.; Zhang, D. Integrated VPSA Processes for Air Separation Based on Dual Reflux Configuration. *Ind. Eng. Chem. Res.* **2019**, *58* (16), 6562–6575.
- (87) Nilchan, S.; Pantelides, C. C. On the Optimisation of Periodic Adsorption Processes. *Adsorption* **1998**, *4* (2), 113–147.
- (88) Niu, Z.; Tang, Z.; Li, W.; Shen, Y.; Zhang, D. Simulation and Optimization of VPSA System Based on Pseudo Transient Continuation Method. *AIChE J.* **2022**, *68* (7). <https://doi.org/10.1002/aic.17729>.
- (89) Peszyńska, M.; Showalter, R. E. A Transport Model with Adsorption Hysteresis. *Differ. Integr. Equ.* **1998**, *11*, 327–340.
- (90) Barton, P. I.; Pantelides, C. C. Modeling of Combined Discrete/Continuous Processes. *AIChE J.* **1994**, *40* (6), 966–979. <https://doi.org/10.1002/aic.690400608>.
- (91) Coffey, T. S.; Kelley, C. T.; Keyes, D. E. Pseudotransient Continuation and Differential-Algebraic Equations. *SIAM J. Sci. Comput.* **2003**, *25* (2), 553–569. <https://doi.org/10.1137/S106482750241044X>.
- (92) Fowler, K. R.; Kelley, C. T. Pseudo-Transient Continuation for Nonsmooth Nonlinear Equations. *SIAM J. Numer. Anal.* **2005**, *43* (4), 1385–1406.

- (93) Kelley, C. T.; Keyes, D. E. Convergence Analysis of Pseudo-Transient Continuation. *SIAM J. Numer. Anal.* **1998**, *35* (2), 508–523.
- (94) Knoll, D. A.; McHugh, P. R. Enhanced Nonlinear Iterative Techniques Applied to a Nonequilibrium Plasma Flow. *SIAM J. Sci. Comput.* **1998**, *19* (1), 291–301.
- (95) Rodopoulos, D.; Weckx, P.; Noltsis, M.; Catthoor, F.; Soudris, D. Atomistic Pseudo-Transient BTI Simulation with Inherent Workload Memory. *IEEE Trans. Device Mater. Reliab.* **2014**, *14* (2), 704–714.
- (96) Tsay, C.; Pattison, R. C.; Baldea, M. Equation-oriented Simulation and Optimization of Process Flowsheets Incorporating Detailed Spiral-wound Multistream Heat Exchanger Models. *AIChE J.* **2017**, *63* (9), 3778–3789.
- (97) Ma, Y.; Luo, Y.; Zhang, S.; Yuan, X. Simultaneous Optimization of Complex Distillation Systems and Heat Integration Using Pseudo-Transient Continuation Models. *Comput. Chem. Eng.* **2018**, *108*, 337–348.
- (98) Grimaud, A.; Rouge, L. Carbon Sequestration, Economic Policies and Growth. *Resour. Energy Econ.* **2014**, *36* (2), 307–331.
- (99) Tapia, J. F. D.; Lee, J.-Y.; Ooi, R. E. H.; Foo, D. C. Y.; Tan, R. R. A Review of Optimization and Decision-Making Models for the Planning of CO₂ Capture, Utilization and Storage (CCUS) Systems. *Sustain. Prod. Consum.* **2018**, *13*, 1–15.
- (100) Huang, Y.; Rebennack, S.; Zheng, Q. P. Techno-Economic Analysis and Optimization Models

for Carbon Capture and Storage: A Survey. *Energy Syst.* **2013**, 4 (4), 315–353.

- (101) Aresta, M.; Dibenedetto, A. Industrial Utilization of Carbon Dioxide (CO₂). In *Developments and Innovation in Carbon Dioxide (CO₂) Capture and Storage Technology*; Maroto-Valer, M. M., Ed.; Woodhead Publishing Series in Energy; Woodhead Publishing, 2010; Vol. 2, pp 377–410. <https://doi.org/https://doi.org/10.1533/9781845699581.4.377>.
- (102) Bruhn, T.; Naims, H.; Olfe-Kräutlein, B. Separating the Debate on CO₂ Utilisation from Carbon Capture and Storage. *Environ. Sci. Policy* **2016**, 60, 38–43. <https://doi.org/https://doi.org/10.1016/j.envsci.2016.03.001>.
- (103) Stephanopoulos, G.; Reklaitis, G. V. Process Systems Engineering: From Solvay to Modern Bio- and Nanotechnology.: A History of Development, Successes and Prospects for the Future. *Chem. Eng. Sci.* **2011**, 66 (19), 4272–4306. <https://doi.org/https://doi.org/10.1016/j.ces.2011.05.049>.
- (104) Turk, G. A.; Cobb, T. B.; Jankowski, D. J.; Wolsky, A. M.; Sparrow, F. T. CO₂ Transport: A New Application of the Assignment Problem. *Energy* **1987**, 12 (2), 123–130. [https://doi.org/https://doi.org/10.1016/0360-5442\(87\)90116-2](https://doi.org/https://doi.org/10.1016/0360-5442(87)90116-2).
- (105) Bai, H.; Wei, J.-H. The CO₂ Mitigation Options for the Electric Sector. A Case Study of Taiwan. *Energy Policy* **1996**, 24 (3), 221–228. [https://doi.org/https://doi.org/10.1016/0301-4215\(95\)00133-6](https://doi.org/https://doi.org/10.1016/0301-4215(95)00133-6).
- (106) Mavrotas, G.; Diakoulaki, D.; Papayannakis, L. An Energy Planning Approach Based on

- Mixed 0–1 Multiple Objective Linear Programming. *Int. Trans. Oper. Res.* **1999**, 6 (2), 231–244. [https://doi.org/https://doi.org/10.1016/S0969-6016\(98\)00056-2](https://doi.org/https://doi.org/10.1016/S0969-6016(98)00056-2).
- (107) Tekiner, H.; Coit, D. W.; Felder, F. A. Multi-Period Multi-Objective Electricity Generation Expansion Planning Problem with Monte-Carlo Simulation. *Electr. Power Syst. Res.* **2010**, 80 (12), 1394–1405. <https://doi.org/https://doi.org/10.1016/j.epsr.2010.05.007>.
- (108) Tan, R. R.; Ng, D. K. S.; Foo, D. C. Y.; Aviso, K. B. Crisp and Fuzzy Integer Programming Models for Optimal Carbon Sequestration Retrofit in the Power Sector. *Chem. Eng. Res. Des.* **2010**, 88 (12), 1580–1588. <https://doi.org/https://doi.org/10.1016/j.cherd.2010.03.011>.
- (109) Pękala, Ł. M.; Tan, R. R.; Foo, D. C. Y.; Jeżowski, J. M. Optimal Energy Planning Models with Carbon Footprint Constraints. *Appl. Energy* **2010**, 87 (6), 1903–1910. <https://doi.org/https://doi.org/10.1016/j.apenergy.2009.12.012>.
- (110) Al-Mohannadi, D. M.; Linke, P. On the Systematic Carbon Integration of Industrial Parks for Climate Footprint Reduction. *J. Clean. Prod.* **2016**, 112, 4053–4064. <https://doi.org/https://doi.org/10.1016/j.jclepro.2015.05.094>.
- (111) Kelley, J. E.; Walker, M. R. Critical-Path Planning and Scheduling. *Pap. Present. December 1-3, 1959, East. Jt. IRE-AIEE-ACM Comput. Conf. - IRE-AIEE-ACM '59* **1959**, 160–173. <https://doi.org/10.1145/1460299.1460318>.
- (112) Takakura, Y.; Yajima, T.; Kawajiri, Y.; Hashizume, S. Application of Critical Path Method to Stochastic Processes with Historical Operation Data. *Chem. Eng. Res. Des.* **2019**, 149, 195–

208. <https://doi.org/https://doi.org/10.1016/j.cherd.2019.06.027>.

- (113) Blake, A.; Hill, S. Rectangular Grid Two-Dimensional Sheets of Copper (II) Bridged by Both Co-Ordinated and Hydrogen Bonded 4, 4'-Bipyridine (4, 4'-Bipy) in [Cu (Á-4, 4'-Bipy)(H₂O)₂(F₃B₃)₂] Ë4, 4'-Bipy. *J. Chem. Soc. Dalt. Trans.* **1997**, No. 6, 913–914.
- (114) Kanoh, H.; Kondo, A.; Noguchi, H.; Kajiro, H.; Tohdoh, A.; Hattori, Y.; Xu, W. C.; Inoue, M.; Sugiura, T.; Morita, K.; Tanaka, H.; Ohba, T.; Kaneko, K. Elastic Layer-Structured Metal Organic Frameworks (ELMs). *J. Colloid Interface Sci.* **2009**, *334* (1), 1–7.
<https://doi.org/10.1016/j.jcis.2009.03.020>.
- (115) Sing, K. S. W. Reporting Physisorption Data for Gas/Solid Systems with Special Reference to the Determination of Surface Area and Porosity (Recommendations 1984). *Pure Appl. Chem.* **1985**, *57* (4), 603–619.
- (116) Ghanbari, T.; Abnisa, F.; Wan Daud, W. M. A. A Review on Production of Metal Organic Frameworks (MOF) for CO₂ Adsorption. *Sci. Total Environ.* **2020**, *707*, 135090.
<https://doi.org/10.1016/j.scitotenv.2019.135090>.
- (117) Na, B.-K.; Lee, H.; Koo, K.-K.; Song, H. K. Effect of Rinse and Recycle Methods on the Pressure Swing Adsorption Process to Recover CO₂ from Power Plant Flue Gas Using Activated Carbon. *Ind. Eng. Chem. Res.* **2002**, *41* (22), 5498–5503.
<https://doi.org/10.1021/ie0109509>.
- (118) Riboldi, L.; Bolland, O. Evaluating Pressure Swing Adsorption as a CO₂ Separation

Technique in Coal-Fired Power Plants. *Int. J. Greenh. Gas Control.* **2015**, *39*, 1–16.

<https://doi.org/10.1016/j.ijggc.2015.02.001>.

(119) Kajiro, H.; Nagai, T.; Igarashi, R. Excipients of Porous Polymer Metal Complexes. JP 2018-153740, 2018. <https://astamuse.com/ja/published/JP/No/2018153740>.

(120) Watanabe, A.; Kishida, K. Adsorption Sheet. JP 2013-154302, 2013.

<https://astamuse.com/ja/published/JP/No/2013154302>.

(121) Kriesten, M.; Vargas Schmitz, J.; Siegel, J.; Smith, C. E.; Kaspereit, M.; Hartmann, M.

Shaping of Flexible Metal-Organic Frameworks: Combining Macroscopic Stability and Framework Flexibility. *Eur. J. Inorg. Chem.* **2019**, *2019* (43), 4700–4709.

<https://doi.org/10.1002/ejic.201901100>.

(122) Schell, J.; Casas, N.; Marx, D.; Mazzotti, M. Precombustion CO₂ Capture by Pressure Swing Adsorption (PSA): Comparison of Laboratory PSA Experiments and Simulations. *Ind. Eng. Chem. Res.* **2013**, *52* (24), 8311–8322. <https://doi.org/10.1021/ie3026532>.

(123) Fujiki, J.; Takakura, Y.; Sugimoto, S.; Kajiro, H.; Yajima, T.; Kawajiri, Y. Breakthrough Analysis for CO₂ Adsorption Kinetics on Flexible Metal-Organic Frameworks. *Available SSRN 4277079* **2022**.

(124) Kondo, A.; Kojima, N.; Kajiro, H.; Noguchi, H.; Hattori, Y.; Okino, F.; Maeda, K.; Ohba, T.; Kaneko, K.; Kanoh, H. Gas Adsorption Mechanism and Kinetics of an Elastic Layer-Structured Metal–Organic Framework. *J. Phys. Chem. C* **2012**, *116* (6), 4157–4162.

<https://doi.org/10.1021/jp210240x>.

- (125) Wakao, N.; Funazkri, T. Effect of Fluid Dispersion Coefficients on Particle-to-Fluid Mass Transfer Coefficients in Packed Beds. *Chem. Eng. Sci.* **1978**, *33* (10), 1375–1384.
[https://doi.org/10.1016/0009-2509\(78\)85120-3](https://doi.org/10.1016/0009-2509(78)85120-3).
- (126) Fuller, E. N.; Schettler, P. D.; Giddings, J. C. A New Method for Prediction Coefficients of Binary Gas-Phase Diffusion. *Ind. Eng. Chem. Res.* **1966**, *58* (5), 18–27.
- (127) NIST Chemistry WebBook. *Carbon Dioxide*. NIST Chemistry WebBook.
<https://webbook.nist.gov/cgi/cbook.cgi?ID=C124389&Units=SI&Mask=7&Type=JANAFG&Table=on#JANAFG> (accessed 2021-07-03).
- (128) NIST Chemistry WebBook. *Nitrogen*. NIST Chemistry WebBook.
<https://webbook.nist.gov/cgi/cbook.cgi?ID=C7727379&Type=JANAFG&Table=on#JANAFG> (accessed 2021-07-03).
- (129) Ruthven, D. M. *Principles of Adsorption and Adsorption Processes*; John Wiley & Sons: New York, 1984.
- (130) Westenberg, A. A.; De Haas, N. Gas Thermal-Conductivity Studies at High Temperature. Line-Source Technique and Results in N₂, CO₂, and N₂-CO₂ Mixtures. *Phys. Fluids* **1962**, *5* (3), 266–273. <https://doi.org/10.1063/1.1706610>.
- (131) Abe, Y.; Kestin, J.; Khalifa, H. E.; Wakeham, W. A. The Viscosity and Diffusion Coefficients of the Mixtures of Light Hydrocarbons with Other Polyatomic Gases. *Berichte der*

Bunsengesellschaft für Phys. Chemie **1979**, 83 (3), 271–276.

<https://doi.org/10.1002/bbpc.19790830315>.

- (132) Kestin, J.; Ro, S. T.; Wakeham, W. A. The Viscosity of Carbon-Monoxide and Its Mixtures with Other Gases in the Temperature Range 25 - 200°C. *Berichte der Bunsengesellschaft für Phys. Chemie* **1982**, 86 (8), 753–760. <https://doi.org/10.1002/bbpc.19820860816>.
- (133) Park, Y.; Ju, Y.; Park, D.; Lee, C.-H. Adsorption Equilibria and Kinetics of Six Pure Gases on Pelletized Zeolite 13X up to 1.0 MPa: CO₂, CO, N₂, CH₄, Ar and H₂. *Chem. Eng. J.* **2016**, 292, 348–365. <https://doi.org/10.1016/j.cej.2016.02.046>.
- (134) Ichiho, O.; Tsuguyuki, S.; Kayoko, K.; Syuji, H.; Akira, I. True Density of Nanocellulose: Contribution of Crystallinity and Surface Modification; The 69th Annual Conference of the Japan Wood Research Society: Hakodate, Japan, 2019.
- (135) Warmuzinski, K. Effect of Pressure Equalization on Power Requirements in PSA Systems. *Chem. Eng. Sci.* **2002**, 57 (8), 1475–1478. [https://doi.org/10.1016/S0009-2509\(02\)00060-X](https://doi.org/10.1016/S0009-2509(02)00060-X).
- (136) Yavary, M.; Ebrahim, H. A.; Falamaki, C. The Effect of Number of Pressure Equalization Steps on the Performance of Pressure Swing Adsorption Process. *Chem. Eng. Process. Process Intensif.* **2015**, 87, 35–44. <https://doi.org/10.1016/j.cep.2014.11.003>.
- (137) DeWitt, S. J. A.; Awati, R.; Octavio Rubiera Landa, H.; Park, J.; Kawajiri, Y.; Sholl, D. S.; Realff, M. J.; Lively, R. P. Analysis of Energetics and Economics of Sub-Ambient Hybrid Post-Combustion Carbon Dioxide Capture. *AIChE J.* **2021**, 67 (11), 1–14.

<https://doi.org/10.1002/aic.17403>.

- (138) Campbell, J. M. *Gas Conditioning and Processing. Vol. 2; Campbell Petroleum Series: Norman, Okla, 1979.*
- (139) Naumov, V. A.; Velikanov, N. L. Simulation of Operational Characteristics of the Water-Ring Vacuum Pumps. *IOP Conf. Ser. Mater. Sci. Eng.* **2019**, *537* (3), 032029.
<https://doi.org/10.1088/1757-899X/537/3/032029>.
- (140) Wang, L.; Yang, Y.; Shen, W.; Kong, X.; Li, P.; Yu, J.; Rodrigues, A. E. Experimental Evaluation of Adsorption Technology for CO₂ Capture from Flue Gas in an Existing Coal-Fired Power Plant. *Chem. Eng. Sci.* **2013**, *101*, 615–619.
<https://doi.org/10.1016/j.ces.2013.07.028>.
- (141) Nahmias, S.; Cheng, Y. *Production and Operations Analysis; McGraw-hill New York, 2009; Vol. 6.*
- (142) Yang, J. Bin; Kao, C. K. Critical Path Effect Based Delay Analysis Method for Construction Projects. *Int. J. Proj. Manag.* **2012**, *30* (3), 385–397.
<https://doi.org/10.1016/j.ijproman.2011.06.003>.
- (143) Lee, A. H. I.; Kang, H. Y.; Huang, T. T. Project Management Model for Constructing a Renewable Energy Plant. *Procedia Eng.* **2017**, *174*, 145–154.
<https://doi.org/10.1016/j.proeng.2017.01.186>.
- (144) Anthonisse, J. M.; van Hee, K. M.; Lenstra, J. K. Resource-Constrained Project Scheduling:

- An International Exercise in DSS Development. *Decis. Support Syst.* **1988**, 4 (2), 249–257.
- (145) Malcolm, D.; Roseboom, J.; Clark, C.; Fazar, W. Application of a Technique for Research and Development Program Evaluation. *Oper. Res.* **1959**, 7 (5), 1959.
<https://doi.org/https://doi.org/10.1287/opre.7.5.646>.
- (146) Murotu, Y.; Ooba, T.; Yonezawa, M.; Hujii, S.; Kogiso, N. *SYSTEMS ENGINEERING*; 2006.
- (147) Kyriakidis, T. S.; Kopanos, G. M.; Georgiadis, M. C. MILP Formulations for Single- and Multi-Mode Resource-Constrained Project Scheduling Problems. *Comput. Chem. Eng.* **2012**, 36 (1), 369–385. <https://doi.org/10.1016/j.compchemeng.2011.06.007>.
- (148) Kopanos, G. M.; Kyriakidis, T. S.; Georgiadis, M. C. New Continuous-Time and Discrete-Time Mathematical Formulation for Resource-Constrained Project Scheduling Problems. *Comput. Chem. Eng.* **2014**, 68, 96–106. <https://doi.org/10.1016/j.compchemeng.2014.05.009>.
- (149) H. Walton. Experience of the Application of the Critical Path Method to Plant Construction. *J. Oper. Res. Soc.* **2017**, 9–16. <https://doi.org/https://doi.org/10.1057/jors.1964.3>.
- (150) Hajdu, M.; Bokor, O. The Effects of Different Activity Distributions on Project Duration in PERT Networks. *Procedia - Soc. Behav. Sci.* **2014**, 119, 766–775.
<https://doi.org/10.1016/j.sbspro.2014.03.086>.
- (151) Zadeh, L. A. Semantic Inference from Fuzzy Premises. In *Proceedings of the Sixth International Symposium on Multiple-valued Logic; MVL '76*; IEEE Computer Society Press: Los Alamitos, CA, USA, 1976; pp 217–218.

- (152) Sadjadi, S. J.; Pourmoayed, R.; Aryanezhad, M. B. A Robust Critical Path in an Environment with Hybrid Uncertainty. *Appl. Soft Comput. J.* **2012**, *12* (3), 1087–1100.
<https://doi.org/10.1016/j.asoc.2011.11.015>.
- (153) Kaur, P.; Kumar, A. Linear Programming Approach for Solving Fuzzy Critical Path Problems with Fuzzy Parameters. *Appl. Soft Comput. J.* **2014**, *21*, 309–319.
<https://doi.org/10.1016/j.asoc.2014.03.017>.
- (154) Xu, J.; Zheng, H.; Zeng, Z.; Wu, S.; Shen, M. Discrete Time-Cost-Environment Trade-off Problem for Large-Scale Construction Systems with Multiple Modes under Fuzzy Uncertainty and Its Application to Jinping-II Hydroelectric Project. *Int. J. Proj. Manag.* **2012**, *30* (8), 950–966. <https://doi.org/10.1016/j.ijproman.2012.01.019>.
- (155) Chen, S.-P.; Hsueh, Y.-J. A Simple Approach to Fuzzy Critical Path Analysis in Project Networks. *Appl. Math. Model.* **2008**, *32* (7), 1289–1297.
<https://doi.org/10.1016/j.apm.2007.04.009>.
- (156) Golenko-Ginzburg, D.; Gonik, A. Stochastic Network Project Scheduling with Non-Consumable Limited Resources. *Int. J. Prod. Econ.* **1997**, *48* (1), 29–37.
[https://doi.org/10.1016/S0925-5273\(96\)00019-9](https://doi.org/10.1016/S0925-5273(96)00019-9).
- (157) Dodin, B. Approximating the Distribution Functions in Stochastic Networks. *Comput. Oper. Res.* **1985**, *12* (3), 251–264. [https://doi.org/10.1016/0305-0548\(85\)90024-3](https://doi.org/10.1016/0305-0548(85)90024-3).
- (158) Herroelen, W.; Leus, R. The Construction of Stable Project Baseline Schedules. *Eur. J. Oper.*

Res. **2004**, *156* (3), 550–565. [https://doi.org/10.1016/S0377-2217\(03\)00130-9](https://doi.org/10.1016/S0377-2217(03)00130-9).

- (159) Bruni, M. E.; Guerriero, F.; Pinto, E. Evaluating Project Completion Time in Project Networks with Discrete Random Activity Durations. *Comput. Oper. Res.* **2009**, *36* (10), 2716–2722. <https://doi.org/10.1016/j.cor.2008.11.021>.
- (160) Hasuike, T. CPMを用いた不確実・不確定状況下におけるクリティカルパスの求解. 京都大学数理解析研究所講究録 **2013**, *1829*, 72–79.
<https://doi.org/https://repository.kulib.kyoto-u.ac.jp/dspace/handle/2433/194808>.
- (161) Tao, S.; Wu, C.; Sheng, Z.; Wang, X. Stochastic Project Scheduling with Hierarchical Alternatives. *Appl. Math. Model.* **2017**, *0*, 1–22. <https://doi.org/10.1016/j.apm.2017.09.015>.
- (162) Ke, H.; Liu, B. Project Scheduling Problem with Stochastic Activity Duration Times. *Appl. Math. Comput.* **2005**, *168* (1), 342–353. <https://doi.org/10.1016/j.amc.2004.09.002>.
- (163) Li, H.; Womer, N. K. Solving Stochastic Resource-Constrained Project Scheduling Problems by Closed-Loop Approximate Dynamic Programming. *Eur. J. Oper. Res.* **2015**, *246* (1), 20–33. <https://doi.org/10.1016/j.ejor.2015.04.015>.
- (164) Azaron, A.; Perkgoz, C.; Sakawa, M. A Genetic Algorithm Approach for the Time-Cost Trade-off in PERT Networks. *Appl. Math. Comput.* **2005**, *168* (2), 1317–1339.
<https://doi.org/10.1016/j.amc.2004.10.021>.
- (165) Huang, W.; Ding, L. Project-Scheduling Problem with Random Time-Dependent Activity Duration Times. *IEEE Trans. Eng. Manag.* **2011**, *58* (2), 377–387.

<https://doi.org/10.1109/TEM.2010.2063707>.

- (166) Kamburowski, J. Bounding the Distribution of Project Duration in PERT Networks. *Oper. Res. Lett.* **1992**, *12* (1), 17–22. [https://doi.org/10.1016/0167-6377\(92\)90017-W](https://doi.org/10.1016/0167-6377(92)90017-W).
- (167) Tavana, M.; Abtahi, A.-R.; Khalili-Damghani, K. A New Multi-Objective Multi-Mode Model for Solving Preemptive Time–Cost–Quality Trade-off Project Scheduling Problems. *Expert Syst. Appl.* **2014**, *41* (4), 1830–1846.
- (168) Li, L.; Lin, R.-B.; Wang, X.; Zhou, W.; Jia, L.; Li, J.; Chen, B. Kinetic Separation of Propylene over Propane in a Microporous Metal-Organic Framework. *Chem. Eng. J.* **2018**, *354*, 977–982. <https://doi.org/10.1016/j.cej.2018.08.108>.

Part of this dissertation is reprinted with permission from ACS Sustainable Chem. Eng. 2022, 10, 45, 14935–14947. Copyright 2022 American Chemical Society.